5-2013

PREDICTION OF SUBSURFACE DAMAGE DURING MACHINING NICKEL-BASED SUPERALLOYS

Yujie Chen
Clemson University, yujiec@clemson.edu

PREDICTION OF SUBSURFACE DAMAGE DURING MACHINING NICKEL BASED SUPERALLOYS

A Dissertation
Presented to
the Graduate School of
Clemson University

In Partial Fulfillment
of the Requirements for the Degree
Doctor of Philosophy
Automotive Engineering

---

by
Yujie Chen
May 2013

Accepted by:
Dr. Thomas R. Kurfess
Dr. Laine Mears
Dr. Mohammed A. Omar
Dr. Huang Yong
Dr. Fadi Abu-Farha

ABSTRACT

Nickel-based superalloys are widely utilized in hostile environments such as jet engines and gas turbines due to their high resistance to oxidation, high corrosion resistance, good thermal fatigue-resistance and fracture toughness. Subsurface damage is typically generated during the machining of these materials, and in particular, γ'-strengthened nickel-based superalloys. The depth of the subsurface damage is a critical requirement specified by the customer. Therefore, it is critical to predict, measure and control subsurface damage.

This research specifically targets the development of a model to predict subsurface damage during the machining of γ'-strengthened nickel-based superalloys. To accomplish this, a modified Johnson-Cook model is developed to represent the plasticity behavior of the material using elevated temperature tests. The proposed model integrates a piece-wise method, strain hardening function, thermal sensitivity function, and flow softening function accurately model anomalous strength behavior. Material subroutines are developed for finite element analysis (FEA) simulation and applied with the ABAQUS/Explicit solver. Orthogonal cutting experiments are conducted to verify FEA results. Recrystallization techniques are utilized for estimation of the depth of subsurface damage. By comparing the subsurface damage between experimental and FEM simulation results, a threshold value is established for determining the depth of subsurface damage.

A high agreement between FEA simulation and experimental results is observed. From the cutting force aspect, the agreement is more than 90% for unaggressive cutting

inputs. On the other hand, the model agreement is slightly lower, 85%, for aggressive machining conditions. This is due to the fact that the severe rake face wear cannot be comprehensively represented in the FEA simulation. In addition, the depth of subsurface damage predicted from the FEA simulations reached an agreement of 95% when compared to experimental findings. Therefore, a subsurface damage model between cutting inputs and depth of subsurface damage has been established based on the results derived from FEA simulations.

ACKNOWLEDGEMENTS

I would like to thank to my advisor, Dr. Thomas Kurfess, for his guidance and help during the last three years. Also, I would like to acknowledge Dr. Cristina Bunget for her guidance, patients and encouragement during this research. I would like to thank my committee members: Dr. Laine Mears, Dr. Mohammed Omar, Dr. Yong Huang and Dr. Fadi Abu-Farha for all their advice on this work. Also, I would like to thank GE Power and Water for supporting this project.

I would like to thank to all the undergraduate student and graduate students, who have been working on GE Power and Water project. I could not accomplish my work without their help.

Finally, I want to acknowledge my wife Ke Xu. With her love and understanding, I could concentrate on my research work.

TABLE OF CONTENTS

Page

Table of Contents (Continued)

Page

Table of Contents (Continued)

Page

LIST OF TABLES

List of Tables (Continued)

Table Page

LIST OF FIGURES

Figure Page

List of Figures (Continued)

Figure Page

List of Figures (Continued)

Figure Page

List of Figures (Continued)

Figure Page

List of Figures (Continued)

Figure Page

List of Figures (Continued)

Figure Page

List of Figures (Continued)

Figure Page

LIST OF NOMENCLATURE

A: Yield strength

A_0 : Original cross-section area

a: Lattice parameter

$a_{\gamma'}$: Lattice parameter of γ'

a_{γ} : Lattice parameter of γ

B: Coefficient of train hardening

C: Coefficient of Strain rate function

C_{ε}: Equilibrium concentration of solute in the matrix

D: effective diffusion coefficient

D_c : Diameter of the specimen

E is young's modulus

n: Strain hardening exponent

P : External uniaxial load

$q_1 \sim q_7$: Coefficients for modified Johnson-Cook model determined by regression method

r: Interface energy

R: universal gas constant

R_g : Goodness of fit

T: Current workpiece temperature

T: Current temperature

$\overline{T}$: Average temperature

T_m: Material melting temperature

T_r: Room temperature

V_m: Volume of precipitate

Vb: Average tool wear

Vb_{max}: Maximum tool wear

v : Surface speed,

w : Revolution per minute and

β_0 : Constant

β_1 : First order coefficient

β_2 : Second order coefficient

γ: Alloy matrix

γ': Strengthening phase of the alloy

σ : Equivalent flow stress

σ_T : Thermal induced stress

σ_{11}, σ_{22}, σ_{33} : Deviatoric stress

σ_1, σ_2, σ_3 : Principal component stresses

σ_m : Hydrostatic stress

σ^{tr} : Trial stress

$\boldsymbol{\sigma}$: Stress tensor

$\boldsymbol{\sigma}'$: Deviatoric stress matrix

σ_e : von Mises stress

$\boldsymbol{\sigma}$: Stress tensor

σ_p^y : Updated yield surface value

σ_0^y : Original yield surface value

σ_{Exp} : Experimental data

σ_{Mod} : Stress from improved model

σ_{TRUE} : True stress

σ_E : Engineering stress

ε : the equivalent plastic strain

$\dot{\varepsilon}$: Equivalent plastic strain rate

$\dot{\varepsilon}_0$: Reference equivalent plastic strain

$\bar{\varepsilon}_0^{pl}$: Initial equivalent plastic strain

$\Delta\bar{\varepsilon}^{pl}$: Increment of the equivalent plastic strain

$\bar{\varepsilon}_f^{pl}$: Strain at fracture point

ε : Total strain

$\boldsymbol{\varepsilon}^p$: Plastic strain

ε_E : Engineering strain

d_{MAZ}: Depth of machined affected zone/Depth of subsurface damage

l_0 Original sample dimension

Δl : Increased dimension

ε_{TRUE} : True stress

$f_{A(\varepsilon,T)}$: Strain hardening function

$f_{S(T)}$: Temperature sensitivity function

$f_{T(\varepsilon,T)}$: Flow softening function

$\overline{\sigma}$: Average value of experimental data

$f_{(\dot{\varepsilon})}$: Strain rate sensitivity function

$r(p)$: Hardening function

v : Poisson ratio

λ : First Lame parameter

G: Second Lame factor (shear modulus)

I : Unit matrix and

$tr(\boldsymbol{\varepsilon})$: Trial strain

n : Tensor normal

f : Yield function

$\sum_{i=1}^{3} \varepsilon_{ii}$: Trace strain

D : Elastic stiffness matrix for isotropic material

$d\varepsilon$: Total strain increment

$d\varepsilon^p$: Plastic strain increment

λ^m : Plastic multiplier

q : Equivalent plastic strain

m^c : Correct factor

h : Hardening function

E^{Inelas} : Inelastic energy

C: specific heat

ΔT : Temperature increment

ρ : Density

α : Thermal expansion

ALLIE: Total internal energy,

ALLSE: Recoverable strain energy,

ALLPD: Plastic dissipation energy,

ALLCD: Energy dissipated by creep and viscoelasticity,

ALLAE: Artificial strain energy

ALE: Arbitrary Lagrangian Eulerian

APB: Anti-phase boundary

DoC: Depth of Cut

FEA(M): Finite element analysis (method)

IN: Inconel

MAZ: Machined affected zone

SEM: Scanning electron microscope

VUMAT: subroutine for Explicit solver

CHAPTER ONE

INTRODUCTION

New high performance systems such as jet engines, high efficiency internal combustion engines and gas turbines have requirements that exceed the mechanical or thermal capabilities of most conventional materials. Nickel-based superalloys are commonly used in these hostile environments, due to their high resistance to oxidation, corrosion, good thermal fatigue-resistance and excellent physical properties at high temperature [1]. However, their unique physical properties result in low machinability, as observed from the experiments [2, 3, 4]. Subsurface damage, which always detrimental to product performance, is becoming a more significant machining characteristic as higher performance is demanded from these high end materials and products. The deformed grains with tensile residual stress yield durability and reliability issues in hostile environments, such as thermo-mechanical fatigue failure under cyclic loads or crevice corrosion in high pressure environments. Furthermore, continuously improved efficiency and performance is driving towards higher temperature operations, requiring more advanced superalloys with specifically designed grain structures and orientations. While such new materials provide better performance, they also are increasingly more difficult to process. The quality required when manufacturing gas turbine and aircraft parts refers not only the characteristics of the surface (*i.e.*, surface roughness, micro-cracks), but also the characteristics below the surface. During the processing of these materials, the grain structures can become deformed (Figure 1). Machining affected zone or subsurface damage caused to the microstructure may only extend a few micrometers into the part;

however, if too much deformation is generated during manufacture, the resulting components (*i.e.*, gas turbine components, Figure 2) lose much of their mechanical integrity, reducing their effective in-service life and raising the potential of extremely costly catastrophic failures. Thus, identifying and minimizing this layer and its depth are of extreme importance [2, 6].

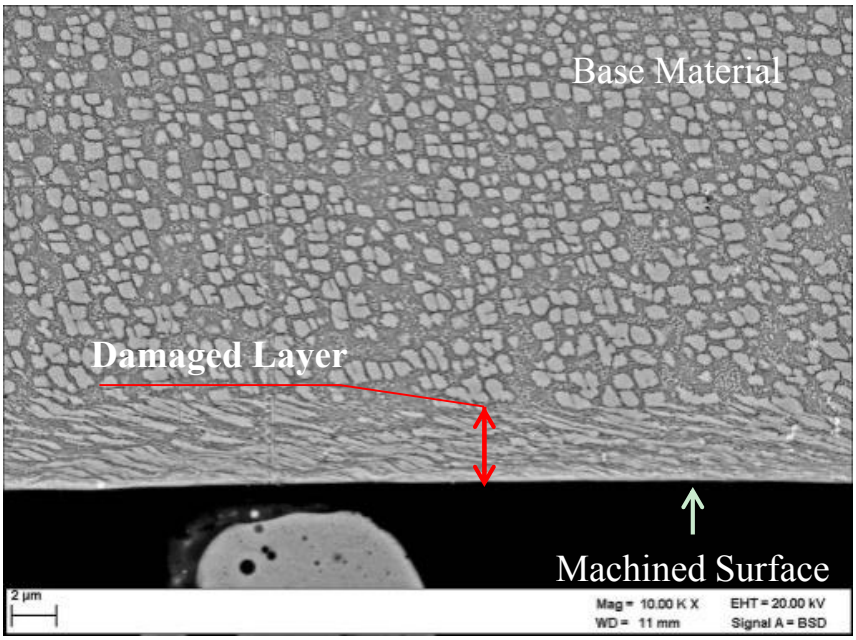

Figure 1: Typical subsurface damage [7].

Figure 2: Example of gas turbine [8].

Problem Statement

The understanding of the mechanisms employed in the machining process of superalloys is the key to higher productivity, better surface integrity, longer tool life, lower energy consumption and, subsequently, a more competitive, viable and sustainable enterprise. Moreover, machining models for nickel-based superalloys are not as well developed as those of other materials such as steel or aluminum. In this research, a methodology of investigating orthogonal cutting of nickel-based superalloys is developed. Also a specific model is established to make estimation of subsurface damage possible during the machining process on γ'-strengthened nickel-based superalloys. During this process, establishing an advanced material constitutive model is necessary.

The material behavior as expressed by the constitutive equations is the key factor for accurately modeling and simulating the cutting process. The Johnson-Cook (Johnson-

Cook) constitutive model is capable of predicting the mechanical properties of a wide variety of material. However, the Johnson-Cook model must to be modified when modeling advanced materials such as Ti-6Al-4V and Inconel 100, as their properties are well outside of typical materials for which this model are developed. Figure 3(a) shows a comparison between the experimental measurements on the flow stress of Inconel 100, and the predictions of the Johnson-Cook model [9, 10]. It can be seen that the properties of the material are much more stable at higher temperatures than expected. In another words, the basic Johnson-Cook model may not accurately predict material behaviors for the advanced materials, such as γ'-strengthened nickel-based superalloy. Moreover, during milling tests performed in the same conditions for three materials, the force recorded for γ'-strengthened nickel-based superalloy was extremely high as compared to steel or even Inconel 718 (Figure 3-b).

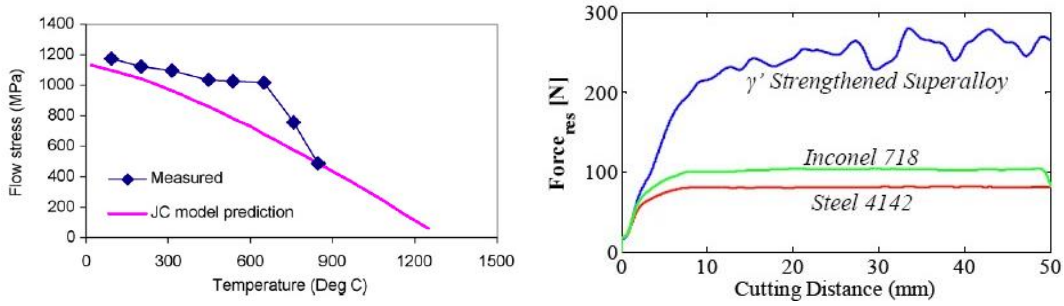

(a) Constitutive model of Inconel 100[6] (b) Cutting forces for three materials

Figure 3: Nickel-based material Performed Atypically.

Usually, for the conventional materials, the higher surface speed always leads to depth machined affected zone [11]. However, the observations from previous work

showed nickel-based superalloys are not consistent with respect to the machining speed, as shown in Figure 4. [12] This suggests the possibility of an atypical cutting mechanism during milling of γ'-strengthened nickel-based superalloy. Thus, a better understanding of the process and a modified material constitutive model are needed for enabling the prediction of the damaged layer in these superalloys.

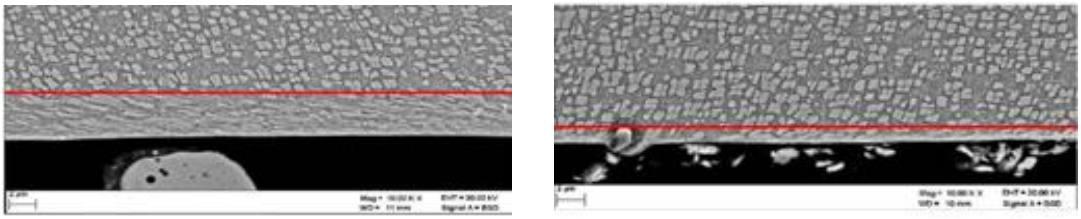

Lower speed and feed *Higher speed and feed*

Figure 4: Lower cutting speed induced higher subsurface damage.

Research Objectives

The purpose of this research lies in establishing a relatively simplified methodology to predict subsurface damage and during machining of nickel-based superalloys by relating it to cutting inputs such as: cutting speed, depth of cut and material properties. This methodology can be extended to other nickel-based superalloys and advanced materials. The objectives of this research are:

- *Formulate a novel material constitutive model for nickel based super alloys.* Elevated temperature tensile tests areperformed to determine the plastic hardening and elastic region.

- *Modify the constitutive machining model to incorporate a piece-wise material model to incorporate material property variations due to thermal considerations.* This enable accurate modeling of the anomalous plastic behavior of γ' strengthened nickel based superalloy at higher temperatures. The piece-wise model is implemented using ABAQUS/Explicit solver.

- *Validate the model.* Validation between the FEA results with the experiments results is conducted.

- *Formulate of a new statistical based machining model.* Based on the validated results from FEA, a statistical machining model for nickel-based superalloys between cutting inputs and depth of subsurface damage are formulated.

The general approach for this research is shown in the flow chart in Figure 5.

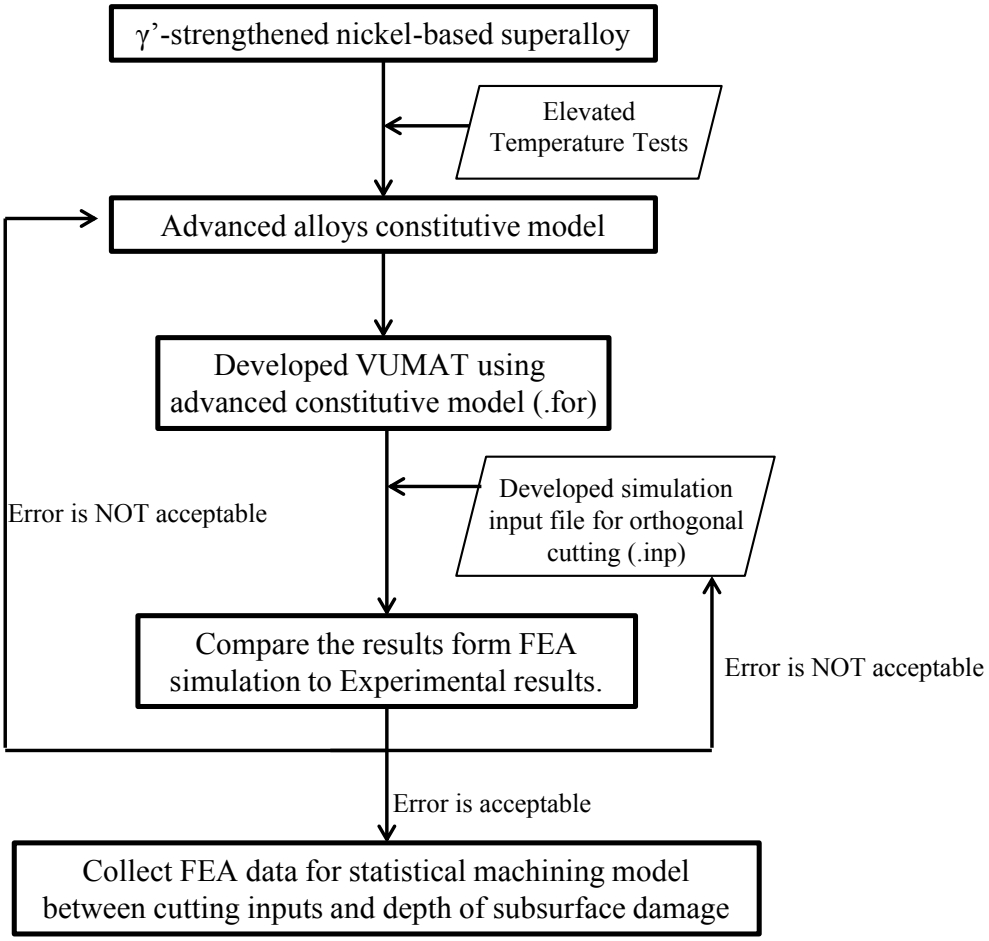

Figure 5: Methodology of the proposed research.

CHAPTER TWO

BACKGROUND

During the machining processing, the surface of the workpiece undergoes elastic deformation, plastic deformation, thermal cycles, dynamic recrystallization and chemical reactions. The mechanical and thermal effects are the main reasons for the subsurface damage in workpiece [13]. For most of the conventional materials, subsurface investigations are fully developed with both FEA and experimental methods. Less research has been accomplished on developing robust material constitutive models for advanced materials such as Ti-6Al-4V and Inconel alloy [10, 15]. Regarding γ'-strengthened nickel-based superalloy, there is no existing material constitutive model or any research done on subsurface damage estimation during machining process.

Experimental Investigations in Machined Subsurface Layer

The presence of a damaged layer was mainly investigated in the hard turning of conventional materials, such as hardened steels, aluminum and titanium alloys. For steel, the changes to the microstructure in the machined surface layer appear as white and dark layers [11, 15]. When machining on titanium alloys, the depth of subsurface damage has been observed to increase with increased cutting speed and feed rate, as shown in Figure 6 [16].

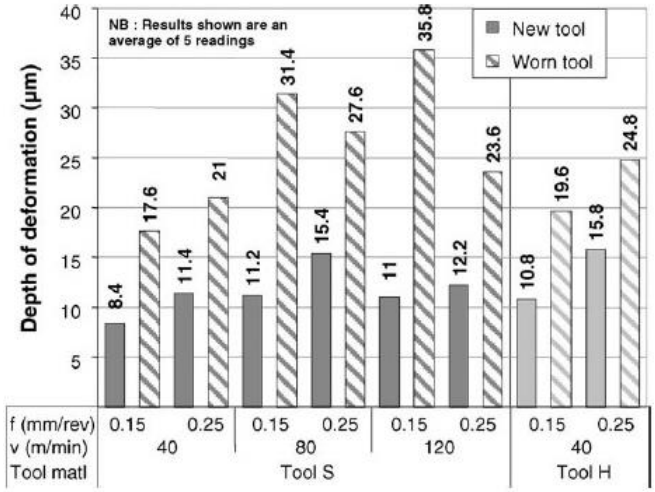

Figure 6: Depth of subsurface damage at different cutting conditions [16].

In 2006, Axinte *et al.* performed turning experiments on a nickel-based alloy under dry conditions, observing deformed layers ~2-3 times harder than the bulk material, which is significantly higher than for steel. [17] Ranganath *et al.* (2009) found larger strains with large edge radii (worn tools) and lower speeds during orthogonal cutting on Inconel 100, which is consistent with the white layer observations for other materials, such as steel [9]. Beside the deformed microstructure and presence of cracks, the subsurface damaged layer exhibits variations in hardness. Experimentally, Inconel 718 was investigated in drilling and turning processes [18, 19]. Pawade *et al.* (2008) conducted turning experiments on Inconel 718 in various cutting conditions, measured the microhardness and recorded the difference from the bulk material, as shown in Figure 7 [20]. The machined affected zone was defined by a threshold value of 200µm. The microhardness decreased rapidly near to the machined surface and was constant 250µm below machined surface.

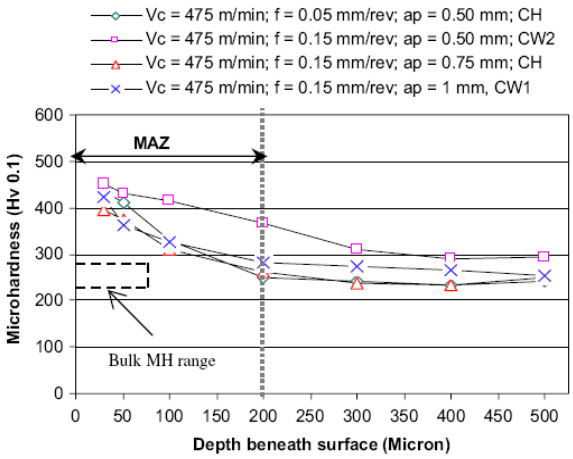

Figure 7: Microhardness profiles of the machined subsurface layer [16].

High tensile residual stress levels, large thickness of the residual stress layer, high work-hardening levels and increased thickness of the work-hardened layer were found after machining Inconel 690, as shown in Figure 8. From this figure, it was concluded that tensile stress always exists along the machined direction and the axial stress transformed from tension to compression after 200μm beneath the machined surface. Furthermore, all stresses decreased to 0 MPa at 150 μm [21].

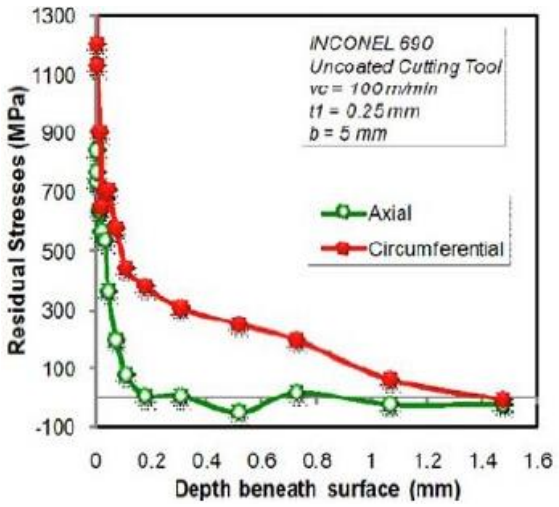

Figure 8: Residual stresses of the machined subsurface layer [21].

End milling on Inconel 718 at cutting speed of 90 m/min, feed rate of 0.2 mm/tooth and depth of cut (DoC) of 0.5 mm was performed and the subsurface damage investigated. The results are shown in Figure 9. A thin layer of plastic deformation was formed beneath the machined surface of the workpiece. In Figure 9-a, a wavy pattern with periodicity of 200 μm and height of 10 μm was observed. In Figure 9-b, the sections of the surface in the feed direction appeared to show no bending of the microstructure; however, in other regions apparent straining/working of the material was visible within the top 5–10 μm region [22].

In Figure 9, the subsurface damage resulting from the turning process on Inconel 718, consisted of deformed grain boundaries in the direction of cutting, and the microhardness increased as compared to the bulk material. In 2006, Sharman *et al.* investigated microhardness in machined affected zone on Inconel 718. It shows that with

a sharp tool (Figure 10-a and Figure 10-b), microhardness decreased to that of the parent material within ~100 μm, as shown in Figure 10 [23]. However, with worn tools, the microhardness reached that of the parent material beyond ~250 μm. This suggests a greater depth of subsurface damage when machining with worn tools as compared to that of new/sharp tools.

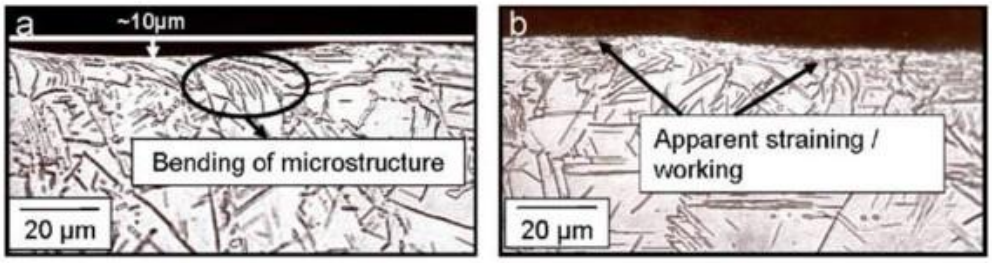

(a) (b)

Figure 9: Subsurface profile of end milling on Inconel 718 [22].

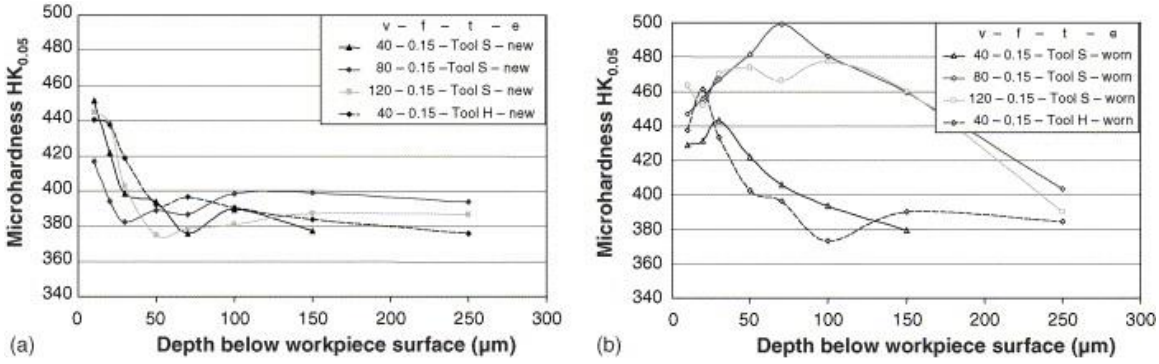

Figure 10: Microhardness profiles of the machined subsurface [23].

Strengthening Phenomenon in γ/ γ' Alloys at Elevated Temperature

Different from the conventional materials mentioned above, γ'-strengthened nickel-based superalloys have FCC lattice structure and ordered γ'-precipitates embedded in γ-matrix. Due to this structure, γ'-strengthened nickel-based superalloys exhibit anomalous material behavior at elevated temperature. The microstructure of these alloys is investigated in this research to explain the strengthened phenomenon under elevated temperature.

These anomalous characteristics are related to the specific crystal structure of the superalloys, which is a two-phase equilibrium microstructure consisting of γ-phase and γ'-precipitates. The γ-phase forms a matrix surrounding the γ'-phase precipitates. Among γ'-strengthened nickel-based superalloys, the strengthening phenomenon at elevated temperature has been observed in previous investigation. In 2009, based on nickel alloy 617, enhanced yield strength phenomenon has been observed by Roy *et al*. [24]. To a certain degree, larger fraction of γ' precipitates ensures a higher strength of the nickel-based superalloys, which are relatively stable even at a higher temperature range. In 2008, Shenoy *et al.* investigated the effects of machining on Inconel 100 microstructure, results are shown in Figure 11. In this research, γ exhibited strength decrease with increasing temperature. However, the performance of γ' phase showed strength increase at a relatively high temperature range, followed by decrease. Thus, the γ- γ' alloy exhibited higher yield strength within temperature range from 700°C to 800°C [25].

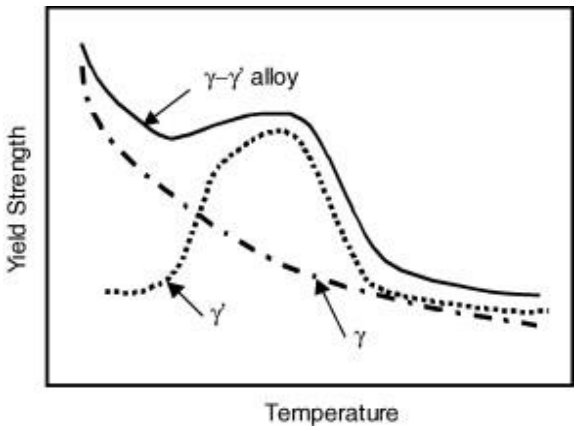

Figure 11: γ and γ' phase of Inconel 100 [25].

Similar observations were reached by Beadmore *et al.* (1969) when the performance of γ and γ' phases at elevated temperature was studies, as shown in Figure 12 [26]. Softening phenomenon and hardening phenomenon (strain hardening) dominate the material strength changes alternatively with rising temperature.

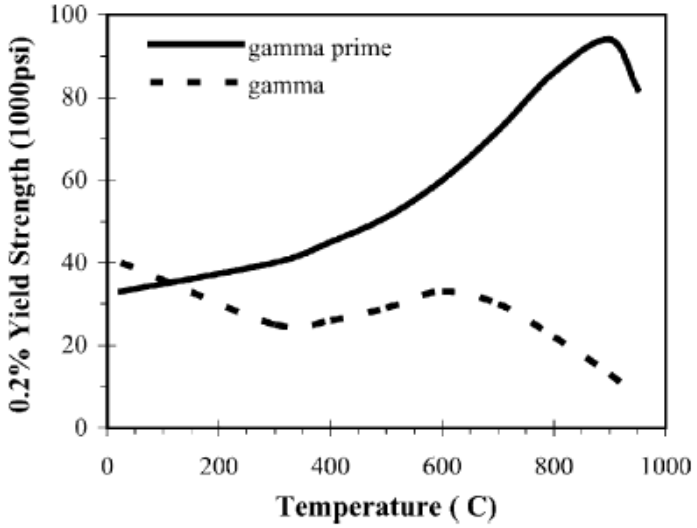

Figure 12: Strength of γ and γ' phase from P. Beadmore research [26].

Investigation of microstructure under elevated temperature on GTD111, which is a type of γ'-strengthened superalloys used in this dissertation, has been performed by S. A. Sajjadi in 2004. Tensile experiments were done under $10^{-4}s^{-1}$ with the temperature varying from 25 to 900 ºC. In this research, verification of the anomalous yield strength with elevated temperatures of superalloys (specifically GTD111) was performed, and some results are shown in Figure 13 [27]. The transformation between γ and γ' phases can cause the material to behave anomalously within a certain temperature range.

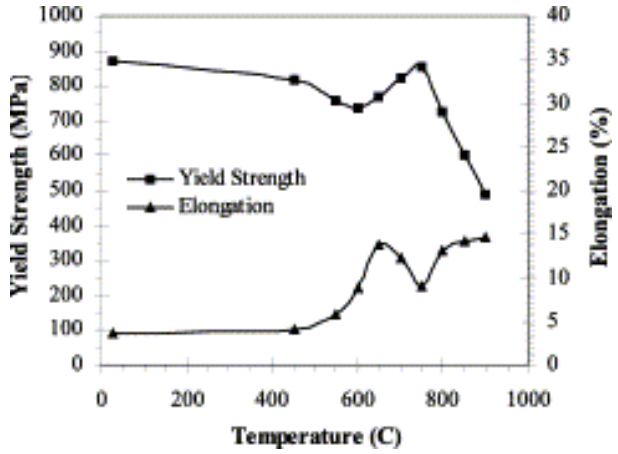

Figure 13: Anomalous yield strength at elevated temperature on GTD111 [27].

For γ'-strengthened superalloys, at temperatures below 600 °C, the deformation is homogeneous and dislocation is restricted to a few slip planes. With increasing temperature, the number of slip bands increases and a homogeneous distribution of dislocation structure formed. At 600 °C, stacking faults start to form, which is shown in Figure 14. When the temperature was in the range of 600 °C to 750 °C, inhomogeneity in localized strains increases while the number of slip plans decreases. A higher density of dislocations forms at the γ and γ' interface and only a few stacking faults are produced.

The dislocation tangles formed at γ and γ’ interface impede the movement of dislocation and further elongation. Between the temperatures of 750 °C and 900 °C, dislocations appear within matrix γ and through γ’. Thus, stacking faults are formed in γ’ at a higher temperature range. [27]

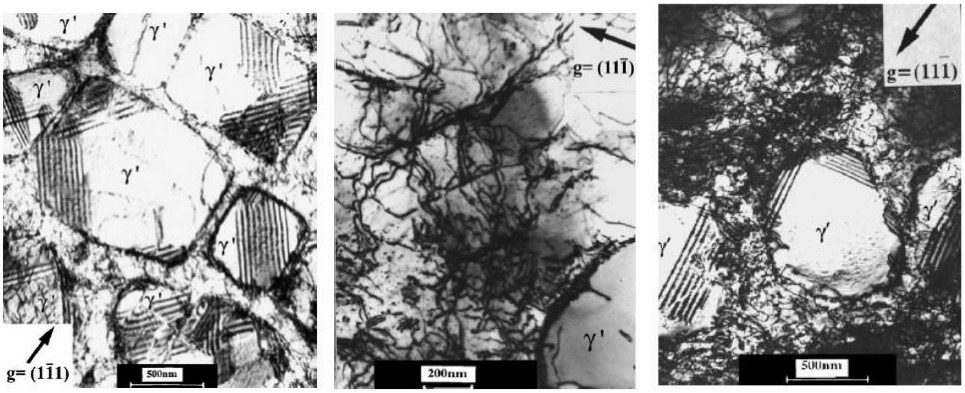

Figure 14: Microstructue with various temperatures [27].

From these results, it can be concluded that the nickel-based superalloys exhibit different plastic behavior for different temperature ranges. Several explanations were posited to explain how various critical machining factors relate to the anomalous behavior. For example, γ/ γ’ lattice parameter mismatch, coherency strain at γ/ γ’ interface, anti-phase boundary (APB), ordered precipitate, differences in elastic moduli between γ and γ’ matrix, particle size of γ’ , volume fraction of γ’ phase have all been considered as casus of this anomalous behavior. However, there are three key factors that are widely accepted as the most likely cause of the strengthening phenomenon in γ/ γ’ alloys at elevated temperatures. These three factors are discussed in the ensuing text, and are not independent.

γ/ γ' lattice parameter mismatch

A small mismatch value between γ and γ' lattice is important for two reasons:

(*i*) When γ and γ' lattices are combined with the cube-cube orientation relationship, there is lower γ/γ' interfacial energy. The ordinary mechanism of precipitate coarsening is driven entirely by the minimization of total interfacial energy.

(*ii*) A coherent or semi-coherent interface makes the microstructure stable, which is an excellent property for elevated temperature applications.

In 1985, M. V. Nathal has investigated the lattice parameter associated with temperature on three nickel-based alloys: nickel alloy 143, NASAIR 100 and Alloy E, which is shown in Figure 15 [28]. The thermal expansion of lattice parameters of γ/ γ' phase was described by second-order polynomial expression:

$$a = B_0 + B_1 \cdot \left(T_c - \overline{T}\right) + B_2 \cdot \left(T_c - \overline{T}\right), \tag{2.1}$$

where a is lattice parameter, T_c is the current temperature, and $\overline{T}$ is the average temperature in studied temperature range.

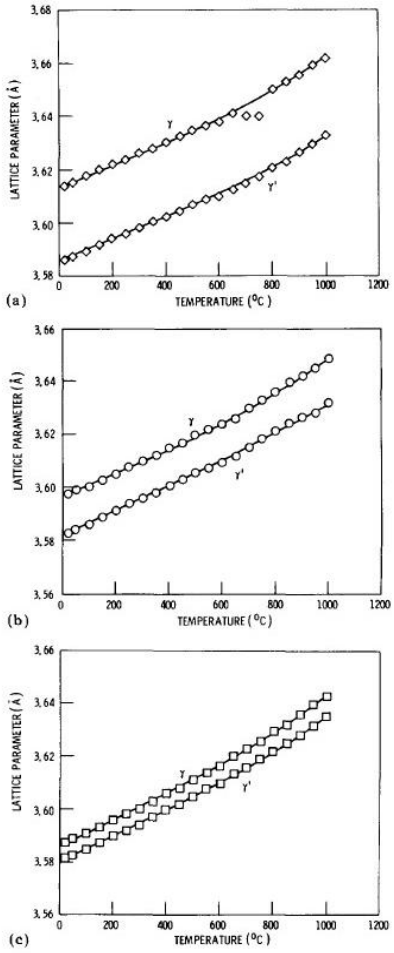

Figure 15: Lattice parameter vs. temperature [28].

As in Figure 15 shown, the expansion of γ'-phase is always smaller than that of the γ-phase for these three nickel based alloys. Also, γ' coarsening is directly influenced by the high value of lattice mismatch. Lattice mismatch is expressed in equation (2.2).

$$\delta = \frac{2\left(a_{\gamma'} - a_{\gamma}\right)}{a_{\gamma'} - a_{\gamma}}, \tag{2.2}$$

where $a_{\gamma'}$ and a_{γ} are the lattice parameters of the γ' and γ phase, respectively.

In Figure 16, the anomalous lattice mismatch in Alloy 143 was explained as: within 600°C to 800°C, Ni3Mo precipitation formed and depleted the γ matrix of molybdenum, yielding a decrease in γ lattice parameter, decreasing the magnitude of the mismatch. Above this temperature range, Ni3Mo dissolves and the mismatch parameter returns to typical values. In this dissertation, similar material behavior was observed on GTD111, which has the same FCC lattice structure as Ni3Mo and also possesses the γ and γ' phase.

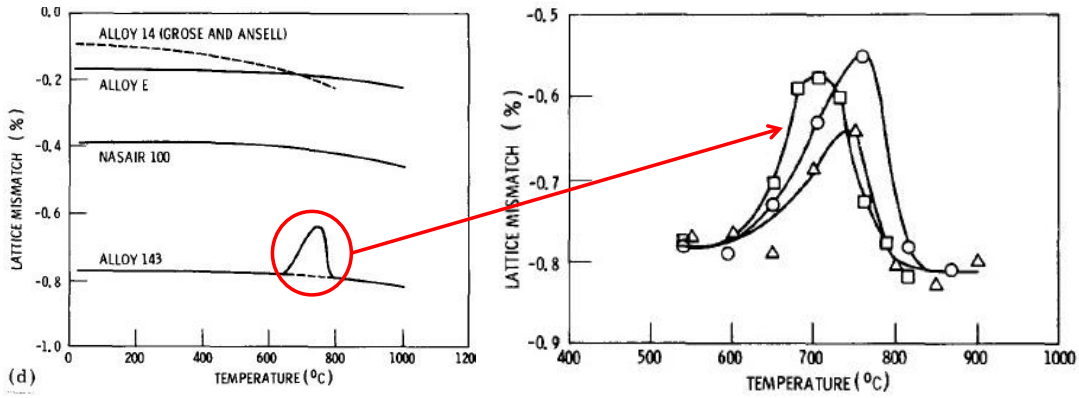

Figure 16: Anomalous lattice mismatch at elevated temperature [28].

In 2001, Glatzel concluded that lattice mismatch attribute anomalous behavior on nickel-based alloy CMSX-4 to two factors:

(*i*) Differences in macroscopic thermal expansion between γ' precipitates and γ matrix;

(*ii*) Compositional changes between the phases.

The mismatch can be controlled by altering the chemical composition, particularly the aluminum to titanium ratio. However, the influence of lattice mismatch is less significant when the diffusion process occurs. [27, 28, 29, 30, 31]

Coherency Strain at γ/ γ' interface

In Ni-based superalloys the γ'-phase [Ni3(Al,Ti)] acts as a coherent barrier to dislocation motion and as a precipitate strengthener. The size of coherent precipitate (γ'-phase) is critical. If the γ'-phase size is too small, some of the coherent precipitate generates a force on the dislocation line that aids movement along the strain path. If the γ'-phase size is too big, there is no enough resistant force generated, from these coherent precipitate, preventing dislocation motion. So within a certain temperature range, when γ and γ' lattice parameters are similar, the strengthening phenomenon is generated. Dislocations in the γ nevertheless find it difficult to penetrate γ', partly because the γ' is an atomically ordered phase. The order interferes with dislocation motion and hence strengthens the alloy. Obviously, the strengthening phenomenon is influenced by temperature, since the γ' coursing processing is induced by the interface energy, which is derived by the temperature between γ and γ' interface. The rate of coarsening process *k*, shown in equation (2.3), is minimized when interface energy reaches minimum value. [32]. The effects of coherency strain hardening are significant at a temperature of at least 800 ºC. One important process that occurs in superalloys at these temperatures is γ' coarsening. [28]

$$k = \frac{8 \cdot r_i \cdot V_m \cdot C_e \cdot D}{9 \cdot R \cdot T}, \tag{2.3}$$

where, r is the interfacial energy, V_m is the volume of precipitate, C_ε is the equilibrium concentration of solutes in the matrix, D is the effective diffusion coefficient, R is the universal gas constant, and T is the absolute temperature.

Ternary phase diagram is shown in Figure 17. For a given chemical composition, the fraction of γ' decreases as the temperature increases. This phenomenon is used to dissolve the γ' at a sufficiently high temperature followed by ageing at a lower temperature in order to generate a uniform and fine dispersion of strengthening precipitates. [31]

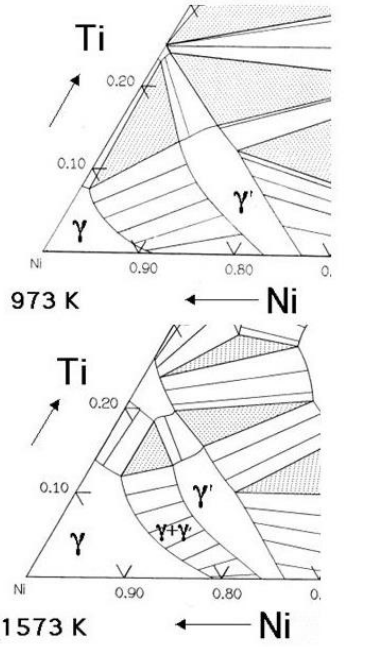

Figure 1: The Ni-Al-Ti ternary phase diagrams show the γ and γ' phase field.

Figure 17: Ternary phase diagram [31].

Anti-phase boundary (APB) in γ' phase

Dislocation dissociates in the γ'-phase, leading to the formation of an anti-phase boundary. At elevated temperature, the free energy associated with the anti-phase boundary is considerably reduced if it lies on a particular plane. This plane is not a permitted slip plane, so that the dissociated dislocation is effectively locked. Several workers have considered anti-phase boundary (APB) strengthening to be the major source for tensile strength in many superalloys. [28] In 2007, K.J. Ducki concluded that the APB is associated with strengthening phenomenon in γ'-phase Fe-Ni alloy. The energy of APB per unit area describes a resistant force to prevent dislocation motion when moving through γ' participate. Finally, these three key elements which are considered the most likely causes of the strengthening phenomenon in γ/ γ' alloys at elevated temperatures, are not independent. That is to say, a change in one most likely yields a change in the other parameters. [27, 28, 29, 30]

Constitutive Model Analysis

An accurate constitutive model is critical for FEM-based analysis. Identification of the constitutive model parameters and high strain rate deformation characteristics are important, since the plastic deformation performed in the cutting zone is fast (several microseconds), relative to the cutting process. Usually, the constitutive model parameters are obtained from Split Hopkins Bar Test (SHPB) at elevated temperatures and strain rates; however, the strain rate from SHPB test, which can reach up to 10^3 s^{-1}, cannot cover the large range of strain rates observed in the shearing zone during high speed cutting

(more than 10^4 s^{-1} in primary shear zone). In order to apply the constitutive model derived from relatively lower strain rate range to higher strain rate situation, an extrapolation method is always adopted.

Few researchers have attempted to model the white layer formation during machining, and then only by observing the chip morphology and microstructure. Even less work has focused on nickel-based superalloys with finite element method [33]. In 2008, M. Calamaz *et al.* developed an improved material model for Ti-6Al-4V with consideration of strain softening. In 2009, Ranganath *et al.* proposed a finite element model for Inconel 100 to predict the plastic strain of the workpiece surface under various cutting conditions during turning process [9]. In this research, the constitutive equation of Inconel 100 was depicted in two temperature ranges. In the course of developing the numerical model, a key need was an accurate model of the material behavior. For a large range of materials, the constitutive law was depicted well by Johnson-Cook (J-C) model, as shown in equation (2.4)[34]. The basic Johnson-Cook model incorporates material strain hardening, strain rate hardening, and thermal softening during the cutting process as follows:

$$\sigma = \left(A + B\varepsilon^{n}\right)\left(1 + C\ln\frac{\dot{\varepsilon}}{\dot{\varepsilon}_0}\right)\left(1 - \left(\frac{T - T_r}{T_m - T_r}\right)^{m}\right), \tag{2.4}$$

where σ is the equivalent flow stress, ε is the equivalent plastic strain, $\dot{\varepsilon}$ is the equivalent plastic strain rate, $\dot{\varepsilon}_0$ is the reference equivalent plastic strain rate, T is the workpiece temperature, T_m is material melting temperature and T_r is room temperature. The flow

stress of a nickel-based alloy (Inconel 100) was measured and compared to the theoretical Johnson-Cook model, and a significant disagreement was found, as shown in Figure 18. The disagreement was more significant when γ' strengthened Nickel-based superalloys were considered, since they are specially designed to exhibit stable properties at high temperatures.

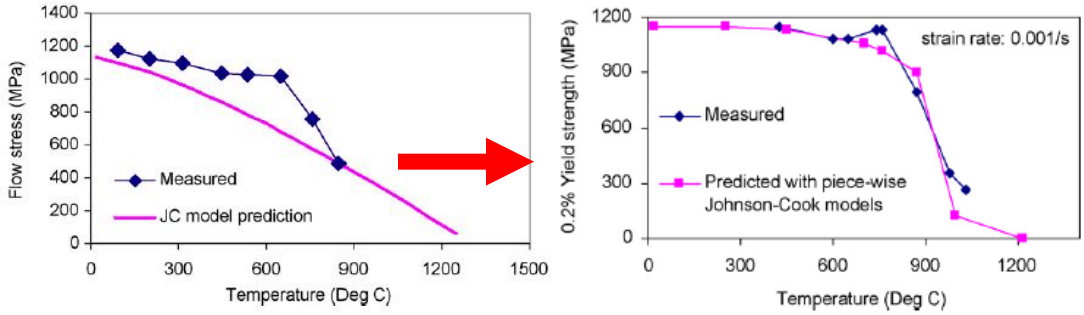

Figure 18: Modified Johnson-Cook constitutive model on Inconel 100 and Inconel 718 [9].

Meanwhile, other approaches for modifying the Johnson-Cook model were proposed by Sima *et al.* (2010). They compared three modified Johnson-Cook constitutive models for Ti-6Al-4V, which is also high thermal resistant alloy [10]. In their research, flow softening was considered, and was evaluated as function of both strain and temperature. As equation (2.5) shows, the first orange bracket represents the flow softening induced by strain, while the second orange bracket considers the flow softening induced by temperature. The three constitutive models for titanium alloys were compared with the experimental data. The third model that incorporates temperature dependent parameters and flow softening proved to be best suitable. It was observed that the

material constitutive model needed to be modified when advanced materials, such as Inconel 718 or titanium alloys were employed. In conclusion, better functions are needed in the equations in order to obtain an accurate material constitutive model.

$$\sigma = \left(A + B\varepsilon^{n} \left(\frac{1}{\exp\left(\varepsilon^{a}\right)} \right) \right) \left(1 + C \ln \frac{\dot{\varepsilon}}{\dot{\varepsilon}_0} \right) \left(1 - \left(\frac{T - T_r}{T_m - T_r} \right)^{m} \right) \left[D + (1 - D) \left(tanh \left(\frac{1}{(\varepsilon + p)^{r}} \right) \right)^{s} \right], \quad (2.5)$$

Other constitutive models are now compared with Johnson-Cook model in this chapter. There are a variety of well-developed models that are widely applied, depending on various experimental methods and research objectives. A power law model is generally accepted for plastic deformation processes at low temperatures and low strain rates. Zerilli-Armstrong (Z-A) model is another model that derived from dislocation mechanisms are the primary cause of the inelastic behavior and its flow stress under different load conditions. Usually, the Z-A model has two different functional forms that are applied to either FCC or BCC single phase material [35, 36]. Nemat-Nasser constitutive model that is developed from microstructure aspects is used commonly for large temperature and strain rate situation [37]. The BCJ model, an internal state variable model, is capable of modeling the complex loading history, recovery, and adiabatic effects of polycrystalline materials. However, the determination of parameters for this model is a complex process [38, 39].

FEM-Based Simulation

Simulation based on finite element method provides a relatively convenient way to obtain results without executing a series of experiments. This method provides more detailed information without actual measurements, such as the residual stress, strain in subsurface, temperature during machining and so forth. Once an accurate material constitutive model is known, an FEM simulation provides good predictions of subsurface damage during different machining process. The advantage of FEM-based analysis is: machining on superalloys is a nonlinear complex dynamic process that includes many random disturbances and cannot be depicted accurately by analytical models. FEM-based simulation method provide a means to obtain results by considering almost the random disturbances during machining process. Also, FEM-based simulation enables the consideration of tool wear during cutting process. The relationship between cutting inputs and subsurface damage can be obtained from the simulation if an accurate material constitutive model is used. The disadvantage of FEM-based method is the computational time that is usually much longer than the actual machining time. During previous research conducted on subsurface damage estimation, commercial FE software packages include ABAQUS, AdvantEdge, and Deform. Both 2D and 3D analysis were investigated. In 2D analysis, the distribution of strain, temperature, residual stress and thickness of white layer were studied during different machining process, such as orthogonal cutting on Ti-6Al-4V. Also, high speed orthogonal cutting 2qw performed on AISI 4340, turning on Inconel 718 and more [9, 40, 41, 42, 43, 44, 45, 46, 47, 48, 72].

Taking advantage of rapid development in computer hardware and numerical methods from prior research, FEM-based analysis has developed quickly for machining processes. To accomplish the separation between chip and workpiece, damage criteria [49, 50, 51] and remeshing technology were applied to these simulations [52, 53]. One of the challenges in the simulations is the difficulty of separating the chip from the workpiece. When referring to chip morphology research with FE method, artificial methods were applied to simulate the realistic situation, *i.e.* separating layer, Arbitrary Lagrangian Eulerian (ALE), in both 2D and 3D [54, 55, 56, 57]. FEM-based simulations were also used to investigate the machining of nickel-based alloys. In 2008, M. Calamaz *et al.* obtained the serrated chip with numerical simulation on Ti-6Al-4V by using temperature compensated material model [72]. Sievert *et al.* (2003) utilized the Johnson-Cook constitutive model to simulate high speed machining of Inconel 718 nickel alloy and provided a ductile damage model [57, 58]. In 2004, Mitrofanov *et al.* studied FE simulation of machining Inconel 718 under ultrasonic assisted turning conditions [59]. Ranganath and Guo (2009) investigated the prediction of white layer formation in Inconel 718 using FEM analysis and piecewise method of temperature was proposed [6]. Uhlmann *et al.* (2007) also utilized the Johnson-Cook material model to simulate cutting of Inconel 718 and used model parameters proposed by Sievert *et al.* [57, 60]. During the research mention above, FEM software ABAQUS 2D, 3D and DEFORM-2D were compared. In conclusion, ABAQUS/Explicit solver is widely accepted in analyzing the extremely plastic deformation and thermal mechanical coupling process, which is applied in this research.

Recrystallization Technology

With the annealing process, new free grains grow until original deformed strain totally consumed. The stored energy in original strain is entirely released from recrystallization process. Main factors in recrystallization process include temperature, annealing time, order of severity from plastic deformation among others.

After a metal has completely recrystallized, if the high temperature is maintained, the grains grow in size. The driving force for this growth is in the surface energy of the grain boundaries. The process measurably decreases the yield strength of the material as the yield stress is inversely proportional to the mean grain diameter. Ductility, on the other hand, increases. Hot working allows recrystallization to occur simultaneously with plastic strain because of the higher temperature. In 1972, M. Filed discussed that this technique was widely utilized in measuring surface integrity with exception of machined surface. [61] In 1991, T. Y. Kim *et al.* applied the recrystallization technique on estimate plastic strain in a machined surface on SS41. [62] In T. Y. Kim's research (1991) tensile tests were conducted to obtain the relationship between equivalent plastic strain and size of recrystallized grain. With various machining inputs, the machined affected zone was investigated with recrystallization technique. Relationship between hardness, equivalent plastic strain and depth of machined affected zone has been developed as well. Also, T. Y. Kim observed that a minimum amount of plastic deformation is the requirement to produce a nucleation of new grains followed by the grain growth. In 1976, T. Shoji revealed that the various metal deformations, such as compression, tension, torsion and

combination of torsion and compression, do not influence the relationship between equivalent plastic strain and recrystallization grain size. [61, 62, 63] Since recrystallization technique can provide a subjective method to distinguish the boundary of subsurface damage, this is utilized in this research for subsurface damage measurements.

Concluding Remarks

In this chapter, several aspects related to machining affected zone are summarized from literature researches. The machining affected zone was experimentally investigated for Inconel 690, Inconel 718, Ti-6Al-4V. The residual stress in machined affected zone decreased associated with the distance from the machined. Also, the residual stress transformed from tension to compression after a certain distance, and ultimately becomes neutral (0 MPa). [6, 10, 21]

The anomalous strengthening phenomenon under elevated temperature was mainly explained from lattice parameter mismatch, coherency strain at γ and γ' phase interface and anti-phase boundary aspects. Also, various constitutive models are compared in order to apply in γ'-strengthened nickel-based superalloy.

Johnson-Cook model is widely accepted and utilized in numerical calculation with finite element method. This model is determined from experimental data at various strain rates and temperatures. Work was performed on improving the Johnson-Cook constitutive model for titanium alloys and nickel-based superalloys. In 2009, Ranganath *et al.* proposed a material model for Inconel 100 to predict the plastic strain of the

workpiece surface under various cutting conditions with finite element method [9]. In this research, the constitutive equation of Inconel 100 was depicted in two temperature ranges based on Johnson-Cook model. In Sima's research, flow softening was considered and evaluated at both strain and temperature [10]. Ultimately, Johnson-Cook constitutive model was selected based on the softening phenomenon and FCC lattice structure.

User defined material subroutine (VUMAT) is developed in this research, since the novel material plastic behavior need to be depicted with modified Johnson-Cook model. Also, ABAUQS/Explicit solver is regarded to have better performance on non-linear material behavior analysis and thermo-mechanical coupling analysis, which is dominant the cutting process during machining process.

In addition, the recrystallization technique is applied in this work. As mentioned earlier, it is a technique to relate plastic strain to the grain size obtained after recrystallization. In this work, the machined samples are recrystallized and the depth of subsurface damage is measured quantitatively.

CHAPTER THREE

DEVELOPMENT OF NOVEL CONSTITUTIVE MODEL FOR γ' STRENGTHENED NICKEL-BASED SUPERALLOYS

In this chapter, a modified Johnson-Cook material model is developed from elevated temperature tensile tests. In this γ' strengthened nickel-based superalloys constitutive model, strain hardening function, thermal sensitivity function, and flow softening function are determined. Also, a piece-wise method is applied as a function of the temperature ranges. These functions are introduced to modify the Johnson-Cook model to be able to capture the specific behavior of the nickel-based superalloys over a large range of temperature, especially the increase in strength at high temperatures.

Preliminary Results

In the course of developing a more complex constitutive model, initial investigations are performed using existing model and simple tensile tests performed at room temperature. The data collected are introduced in FEA simulation of 3D orthogonal cutting tests, together with material parameters used for Inconel 718. The simplified Johnson-Cook material model is derived from these data. After the simulations are conducted, the subsurface damage is estimated and compared to results from experimental orthogonal cutting tests. The material used is GTD111, which is a nickel based alloy and shares similar chemical composition and phases with Inconel 718, but is much more difficult to machine.

FEA simulation development

Room temperature tensile test were performed at the Clemson University – International Center of Automotive Research. A strain rate of 0.005 s^{-1} and a temperature of 295K were used for these tests. The engineering data are converted into true strain and true stress. The true strain-stress data are applied to derive the modified power law, which is a simplified format of Johnson-Cook model. Equation (2.6) shows the format of power law.

$$\sigma = \left(A + B\varepsilon^{n} \right) , \tag{2.6}$$

where A is the yield strength, n is the hardening coefficient and B is derived using regression method, as shown in Figure 19.

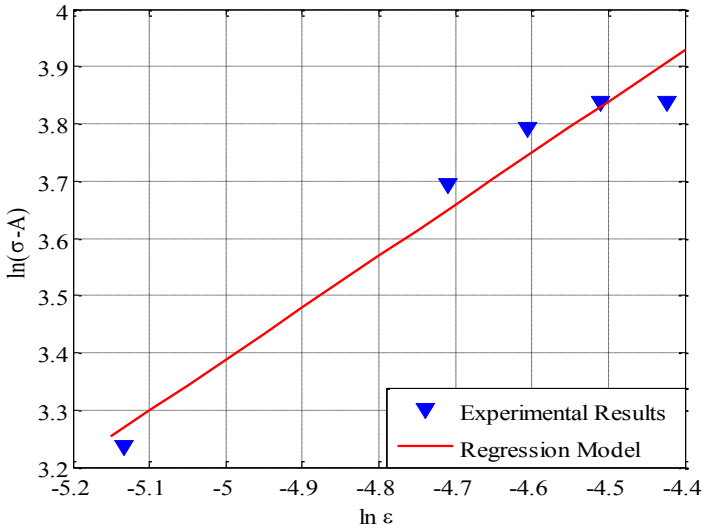

Figure 19: Regression method to determine parameter of power law.

Regression method was used on the data from Figure 19 to generate the three parameters from equation (2.6). The results from the regression method are summarized in Table 1.

Table 1 Parameters of Power Law model

A	774 MPa
B	2256 MPa
n	0.97

Then, equation (2.6) is written as equation (2.7).

$$\sigma = \left(774 + 2256\varepsilon^{0.97}\right), \tag{2.7}$$

Assumptions used in the simulations:

- The material properties are similar to Inconel 718, as shown in Table 2.

Table 2 Parameters/Properties of workpiece [64]

Properties	Value
Elastic Modulus	200 GPa
Density	8220 Kg/m^3
Thermal Expansion	7.1x10^-6/°F
Thermal Conductivity	18.0 w/m.k
Specific Heat Capability	435 J/kg.K

- The material is assumed to be isotropic.
- Plastic data and hardening characteristics are obtained from tensile test at room temperature, and they are assumed as temperature-independent up to 1500ºC. Although simplifying, this assumption is valid since the superalloys are specially designed to maintain constant properties at very high operating temperatures.
- The element type selected for the workpiece is C3D8RT, allows for thermal mechanical coupling processing specific to cutting. The workpiece is meshed with 6173 elements.
- The cutting tool is assumed as analytical rigid body, and it is meshed in 3000 elements. The properties of the tool are summarized in Table 3.

- Since cutting process includes large deformation, Arbitrary Lagrangian Eulerian meshing (ALE) is applied in the simulations. Also, the relax stiffness method is applied to control the hourglassing and avoid extreme distortion of the elements [65].

Table 3 Properties of tool. [66, 67]

Properties	Value
Thermal Conductivity	46 w/m.k
Density	1420 kg/m^3
Specific Heat Capability	39.8 J/mol K

- Since the modeled cutting process occurs in very short time, adiabatic heating is assumed.
- The friction coefficient is set as 0.1 between all the interfaces.
- The cutting tool remains sharp during the entire cutting process.
- Material plastic property does not take softening effect into consideration.
- No vibrations occurred between workpiece and cutting tool.
- To fulfill the chip separation from workpiece, shear failure criteria and element deletion are applied in ABAQUS/Explicit. Shear failure criterion is defined by comparing the equivalent plastic strain to a failure value. Elements deletion is defined when the damage parameter, ω, exceeds 1. The damage parameter, ω, is defined as in equation (2.8):

$$\omega = \frac{\bar{\varepsilon}_0^{pl} + \sum \Delta \bar{\varepsilon}^{pl}}{\bar{\varepsilon}_f^{pl}}, \tag{2.8}$$

where $\bar{\varepsilon}_0^{pl}$ is the initial equivalent plastic strain, $\Delta \bar{\varepsilon}^{pl}$ is an increment of the equivalent plastic strain, and $\bar{\varepsilon}_f^{pl}$ is the strain at fracture point.

The cutting force is given by the reaction force from the elastic and plastic deformation, measured from the reference point, and also with the friction force. In the simulation, some oscillations were observed in the resultant force due to the deletion of elements, and this aspect cannot be found in the empirical force. But experiments show an increasing trend attributed to the tool wear that cannot be reproduced yet in the simulations. Thus, the simulation force is compared to the force at the beginning of the test, after 1 revolution. Figure 20 compares the forces from the experiments (after 1 and 5 revolutions) to the FEA predicted force. The maximum error is ~16%. However, in the experiments, tool wear appears immediately after the cutting tool is engaged into the cut. Moreover, there is also the thermal softening effect occurring.

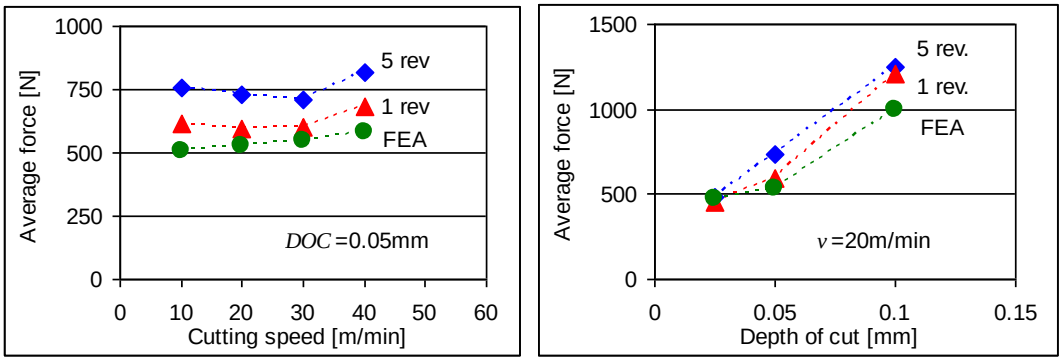

Figure 20: Force comparison between Experiments and FEA.

In FEA simulation, the depth of subsurface damage layer that presents straining is measured and compared to the experimental results. By removing surface elements, the cross-section of tool/chip interaction and machined surface is obtained. Figure 21 exemplifies the procedure for speed of 20m/min, and depth of cut of 0.1mm. The measurement is taken after a 2mm length is cut in the test. It is concluded that finite element simulations can be used for estimating damage, and the trial-and-error tests can be reduced/avoided, as well the need for destructive methods for evaluation.

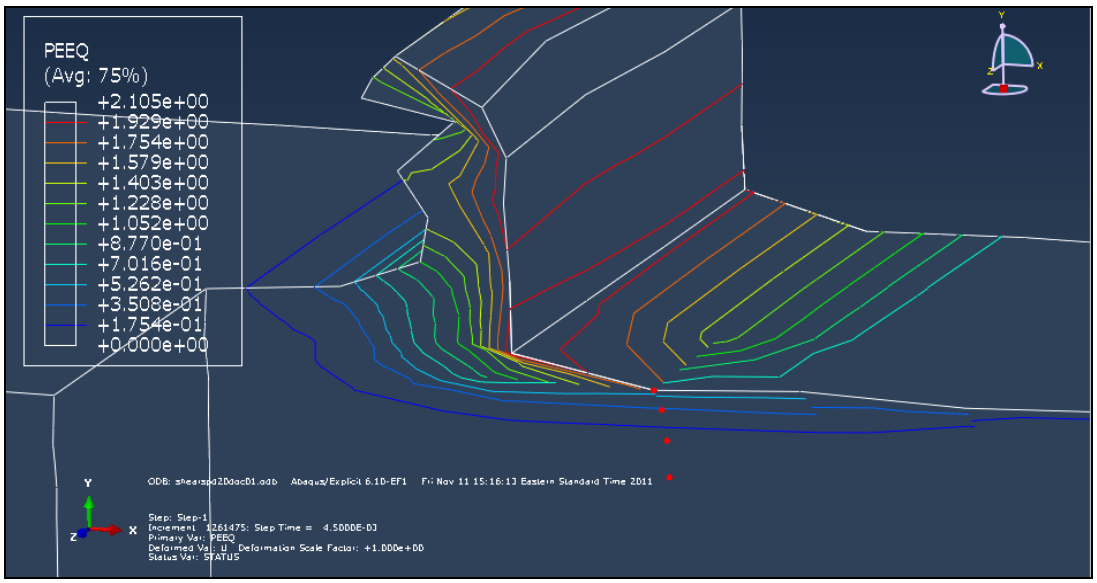

Figure 21: PEEQ contour and method for measuring depth of subsurface damage - line contour with cutting speed v= 20m/min; Depth of cut: 0.1mm.

Experimental sample preparation

In order to compare the FEA results to experimental results, subsurface damage measurement from experiments has been investigated. Initially, the specimens are

prepared for the metallographic analysis. The specimens are cut using an electric discharge wire cutting machine to avoid plastic deformation near the surface, then embedded in resin, ground in steps to the smallest grit size, and polished with 1μm polycrystalline diamond suspension and 0.05μm alumina slurry. The polished specimens are etched using Marble's reagent. The subsurface layers are analyzed under the scanning electron microscope (SEM - Hitachi 3400) under variable pressure. The types of damage obtained in the machined layer are: and (i) micro-cracks possible related to the presence of γ'-phase inclusions (Figure 22), and (ii) deformed structure with elongated grains.

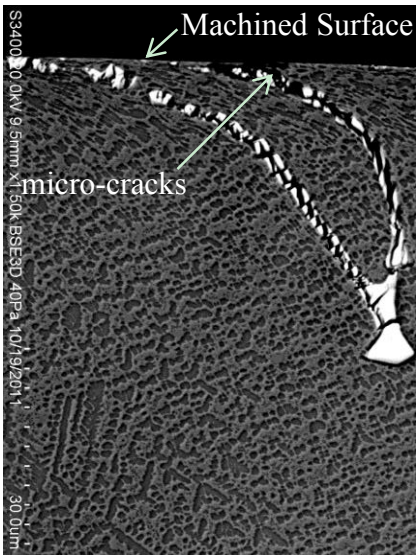

Figure 22: Micro-cracks in the machining affected layer (DoC=0.050mm, v=40m/min).

The depth of the machining affected layer varies based on the cutting conditions used. Figure 23 shows two cases, with small and large depth of subsurface damage. The

depth of subsurface damage is measured for all the tests around the circumference of the cylindrical specimens, and an average subsurface damage is determined.

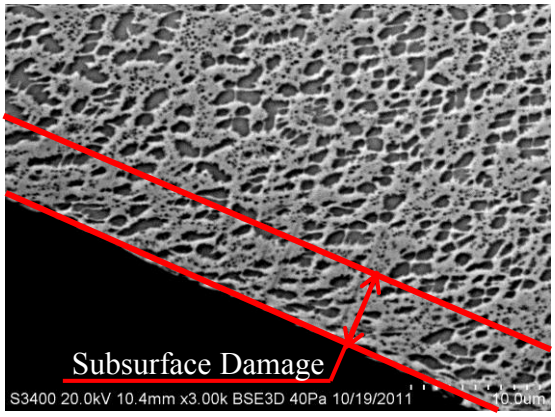

(a)

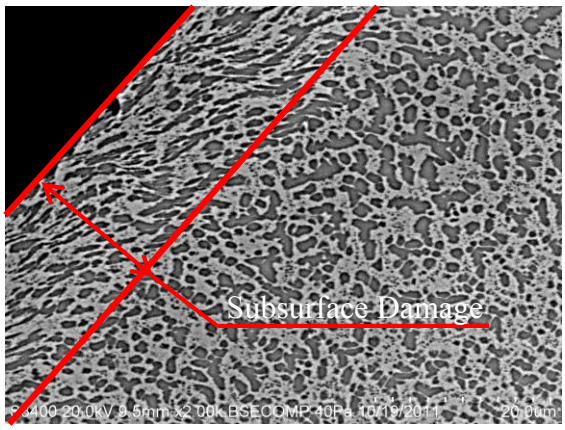

(b)

Figure 23: Subsurface damage for DoC=0.050mm and the cutting speed of (a) 30m/min and (b) 40m/min.

One drawback of using the micrographs for evaluating the subsurface damage is that it is highly subjective. Not only that the operator can interpret, but even the statistical

method applied to the image gives errors, since it cannot see the whole distorted structure [7]. In reality, even if small plastic strains occurred in the microstructure, they are still considered damage since they can result in residual stress, but it may be not observable in the micrograph.

The similar trends of the depth of subsurface damage and forces with cutting conditions suggest that there is a correlation between the cutting force and depth of subsurface damage, and an empirical model can be determined by using the regression analysis, more specifically the least squares method. Figure 24 shows a quadratic model for the depth of machining zone (d_{MAZ}), as given by equation (2.9):

$$d_{MAZ} = \beta_0 + \beta_1 \cdot F - \beta_2 \cdot F^2, \tag{2.9}$$

$$\beta_0 = 1; \beta_1 = 0.01865; \beta_2 = 0.000008, \tag{2.10}$$

where the unit for the force , F, is Newton, and the units for the parameters $\beta_0, \beta_1, \beta_2$ are adjusted such that subsurface damage resulted is in microns. This model is valid only in the range of parameters sued in the present work, and it can be used when is possible that the cutting force is controlled.

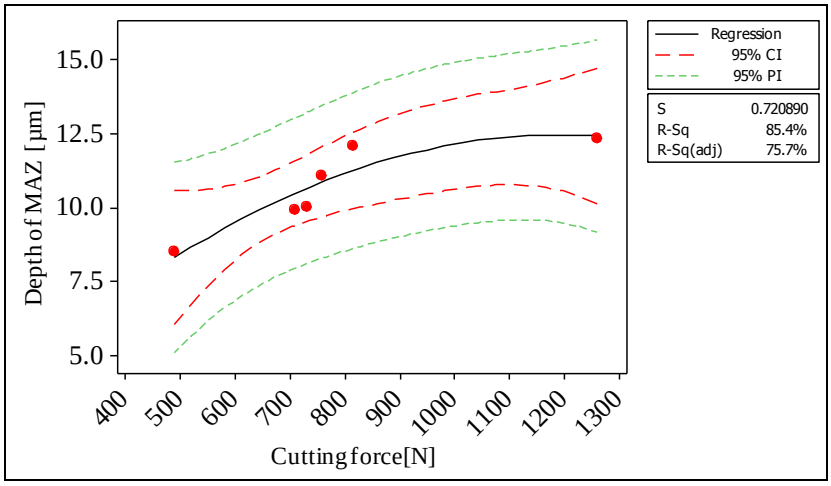

Figure 24: Regression model (quadratic fit) for the depth of machining affected zone as a function of force.

Comparison and Conclusion

When comparing the FEA predicted and experimentally measured (using SEM) depth of subsurface damage, shown in Figure 25, these results are seen to have a significant difference. This difference may be induced by two aspects: (*i*) the material model is not accurate and/or (*ii*) the way to measure empirical subsurface damage is not sufficient. Therefore, these two aspects are investigated further to improve predicting the depth of subsurface damage.

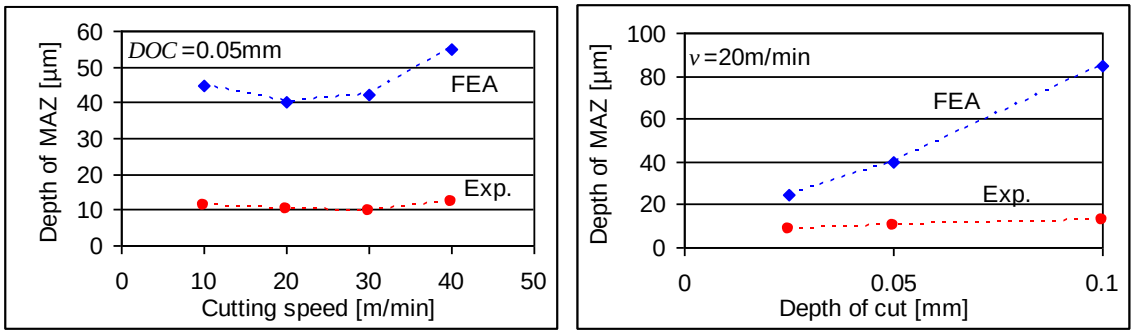

Figure 25: Experiment-Simulation comparison for the effect of DoC and speed on MAZ.

Elevated Temperature Tensile Tests and Discussion

As it mentioned in last section in order to obtain more accurate FEA simulation results, the elevated temperature tests are necessary to derive an improved material model for γ'-strengthened nickel-based superalloy.

Material Composition

In this research, the material has been investigated on is GTD111, which is a γ'-strengthened nickel-based superalloy. In 2003, Alejandro R. Ibanez and Richard W. Neu have completed the tensile tests at elevated temperatures on directionally solidified GTD111 [69]. The chemical composition of directionally solidified GTD111 is summarized in Table 4.

Table 4 Chemical Components of GTD111. [69]

	Cr	Co	Al	Ti	W	Mo	Ta	C	Zr	B	Fe	Si	Mn	Cu	P	S	Ni
Min	13.7	9.0	2.8	4.7	3.5	1.4	2.5	0.08	0.005	-	-	-	-	-	-	-	Bal
Max	14.3	10.0	3.2	5.1	4.1	1.7	3.1	0.12	0.04	0.02	0.35	0.3	0.1	0.1	0.015	0.005	Bal

Specimens Preparation

The specimens were prepared as cylinders, with the diameter and length of gage area of 4.064 mm and 25.4 mm, respectively, as shown in Figure 26. The extensometer was applied to measure the displacement during the tests. There are three locator holes, which were used for mounting the extensometer, on the grip section between the pull rod and specimen. These help keeping the plastic deformation only in the gauge section, improving the accuracy of the strain measurement from the gauge portion.

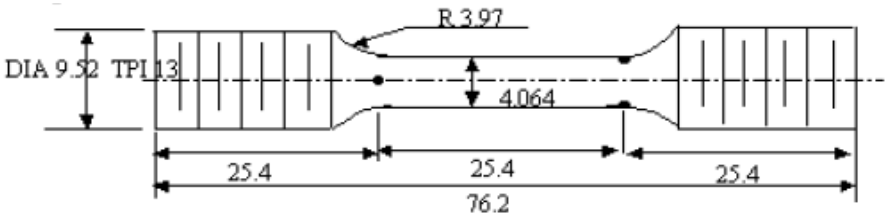

Figure 26: Specimen dimensions [71].

Tensile Test Setup

Uniaxial tensile tests were performed in longitudinal direction conform to the ASTM standard E1820-96 [70]. Strain rate was set to a constant value of 1.6×10^{-4} s^{-1}. The specimens were heated in furnace to the specified temperature for each test. The pull rods and grips were fabricated with Inconel 713C with high temperature environment

operation purpose. Displacements and loads were recorded during each test and converted to true strain-stress results. The temperature was measured by K-type thermocouples. Two thermocouples were attached at the top and bottom of the gage area to ensure that the temperature distributed homogeneously. The design of tests is shown in Table 5. The test setup is shown in Figure 27. Each test condition was repeated three times.

Table 5 The design of the tensile tests.

	Longitudinal and Transversal			
Temperature [K]	294	922	1033	1144
Replicates	3	3	3	3

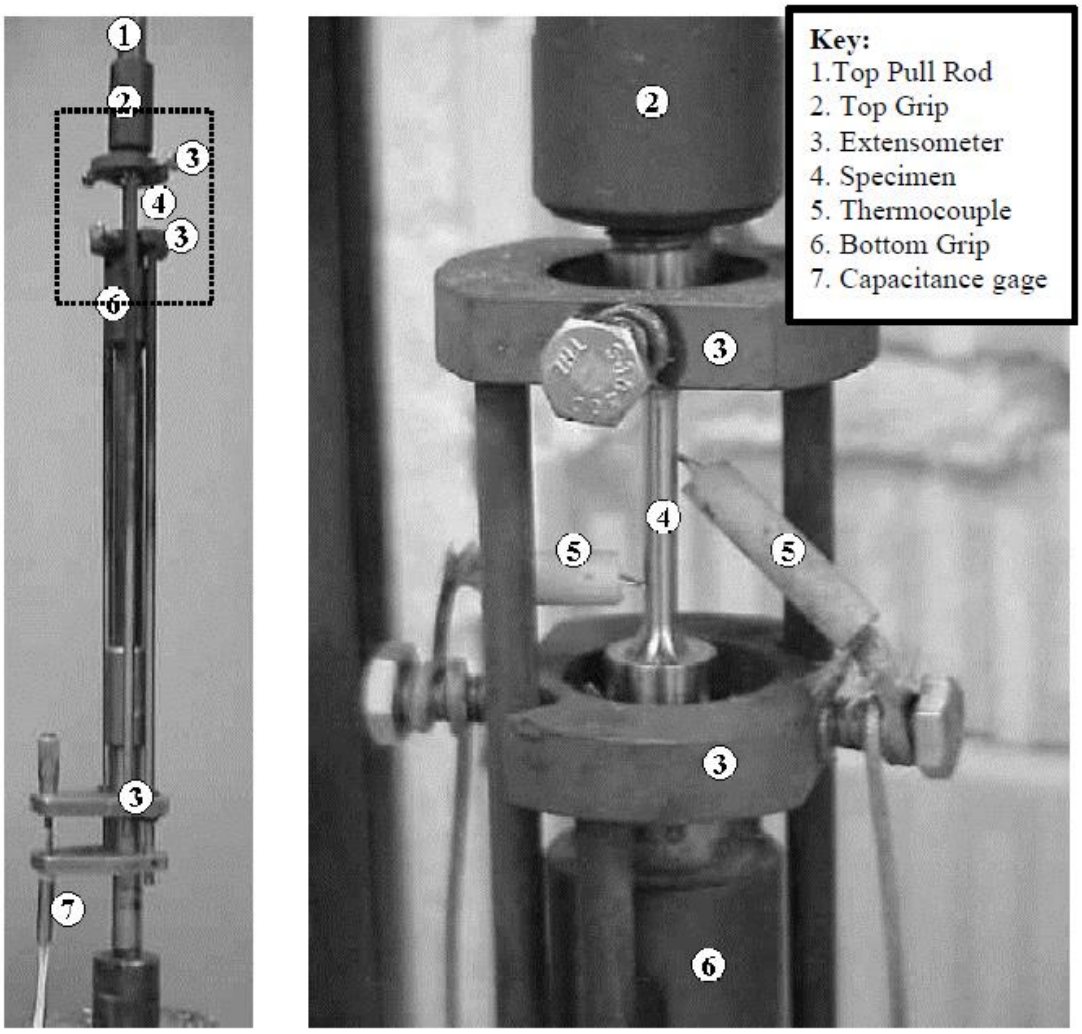

Figure 27: Elevated tensile test setup [69].

Tensile Tests Results

Since this material is directional, the results were recorded for longitudinal and transversal directions. Also, in order to determine which directional results are applied in this research, the two directional results were compared with the equiaxed result published by Daleo and Wilson. [71]

Since, ultimate tensile strength, elongation and reduction of area are reported as the indicators of deformation characteristics of the material, the results are compared on these three aspects, as shown from Figure 28 to Figure 30. As Figure 28 shown, the anomalous ultimate tensile strength trend is observed in both longitudinal, transversal and equiaxed materials. When comparing longitudinal direction material and equiaxed material, similar trend and values were recorded, especially for the higher temperature range. In Figure 29 and Figure 30, for the specimen cut in longitudinal direction, both percent elongation and area reduction keep on a relatively constant level at lower temperature range. Then, gradient becomes steeper when the temperature is greater than 1033K. This may be related to the sharp reduction in yield strength and the change in slip mechanism in Ni3Al beyond that temperature. The same behavior is observed for the equiaxed material, as seen in Figure 29 and Figure 30. For the specimen prepared in transversal direction, the changes in ductility with temperature are not as noticeable as in the longitudinal direction. Moreover, for transversal directional material, the material performance associated with the rising temperature is reversed as compared to the longitudinal and equiaxed material after 923K [69].

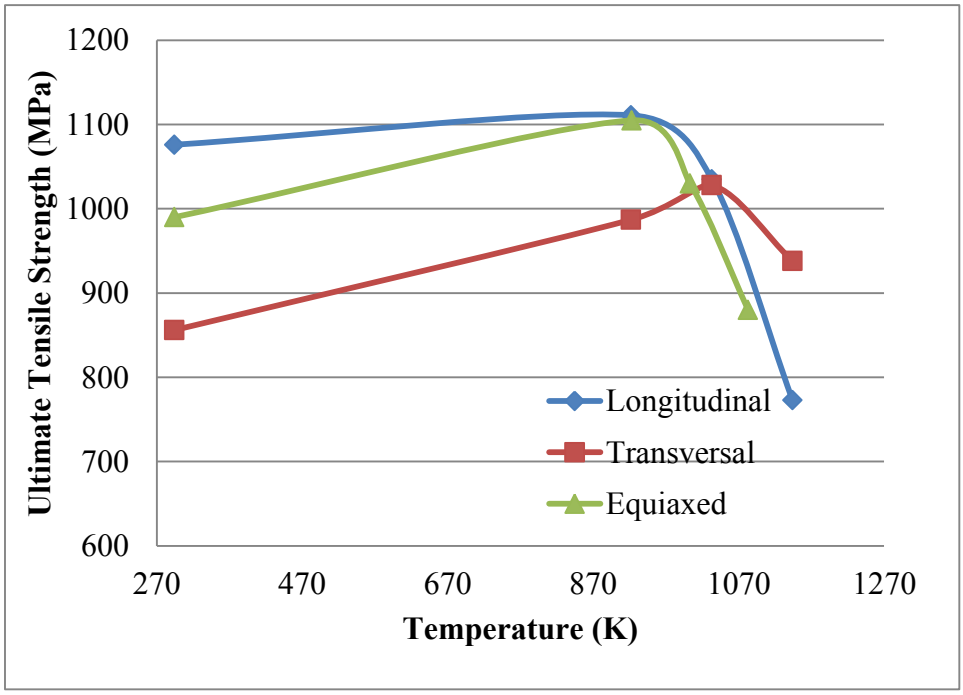

Figure 28: UTS vs. Temperature – Longitudinal, Transversal and Equiaxed materials.

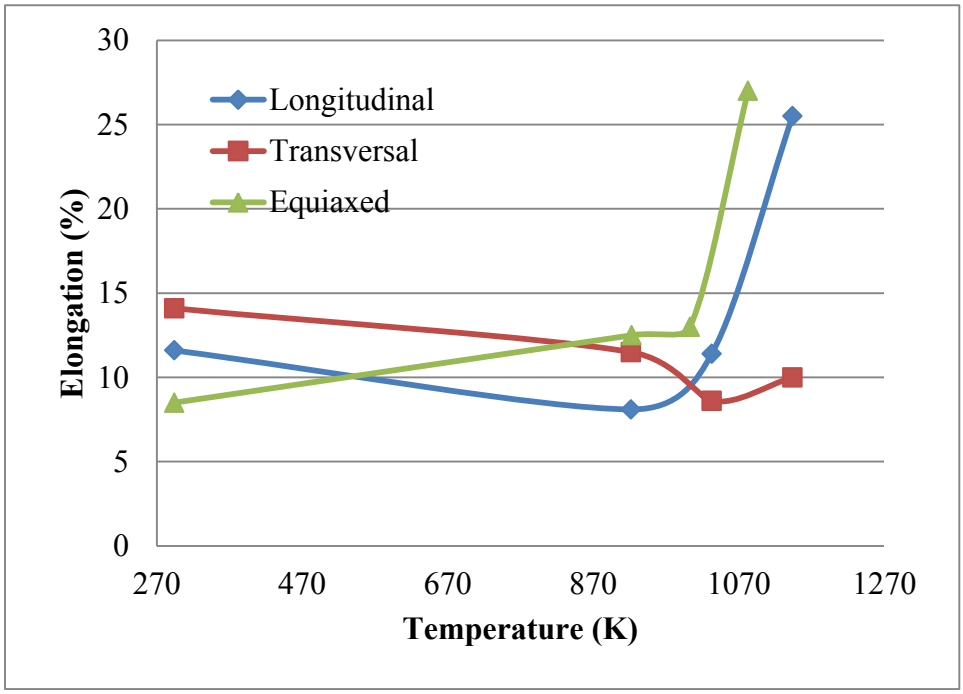

Figure 29: Elongation vs. Temperature – Longitudinal, Transversal and Equiaxed materials.

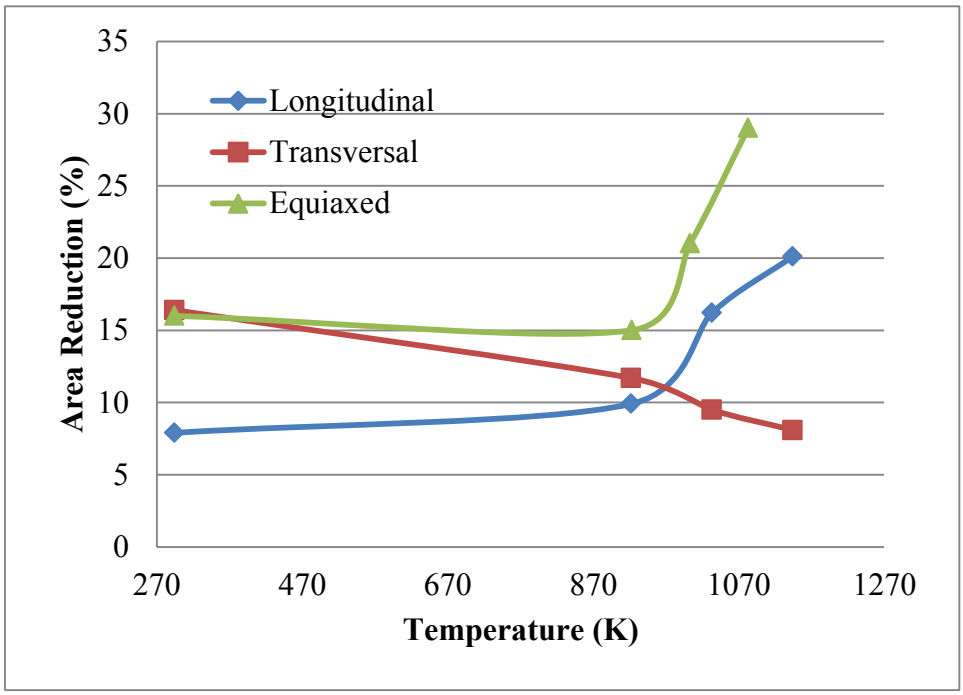

Figure 30: Area reduction vs. Temperature – Longitutinal, Transversal and Equiaxed materials.

In conclusion, when comparing ultimate strength, elongation and cross-section reduction, the longitudinal material exhibits similar plastic properties as equiaxed material. Total elongation and area reduction are the two indicators to describe material ductility. Ductility is commonly defined as the materials ability to plastically deform. Therefore, longitudinal direction results can be used for developing the novel material constitutive model for GTD111 in this research.

Development of an Improved Material Model

In Figure 31, strain-stress curves show the results recorded for four temperatures: 294K, 922K, 1033K and 1144K. The results are the averaged data from three replicates in longitudinal direction. The strain and stress in Figure 31 are true data, as derived by

$$\sigma_E = \frac{P}{A_0}, \tag{3.1}$$

$$\varepsilon_E = \frac{\Delta l}{l_0}, \tag{3.2}$$

$$\sigma_{TRUE} = \sigma_E \cdot (1 + \varepsilon_E), \tag{3.3}$$

$$\varepsilon_{TRUE} = \ln(1 + \varepsilon_E), \tag{3.4}$$

where σ_E is engineering stress, P is the external load, A_0 is original cross-section area, ε_E is engineering strain, l_0 is the original sample dimension, Δl is increased dimension, σ_{TRUE} is true stress, and ε_{TRUE} is the true strain.

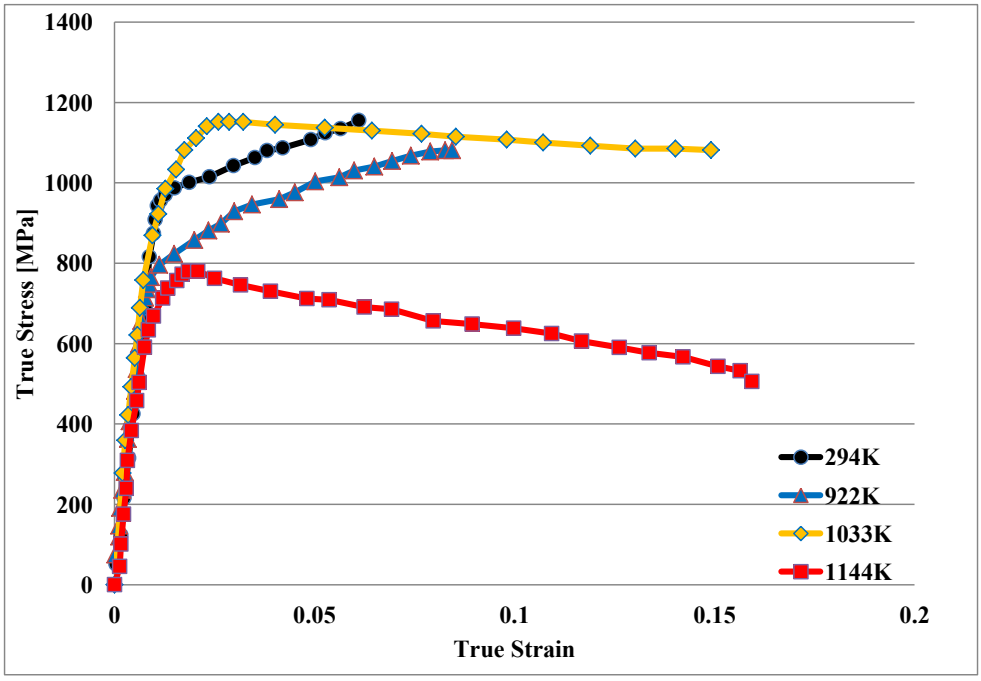

Figure 31: True strain-stress curves at various temperatures.

After analyzing the results of the elevated temperature tensile tests performed on γ'-strengthened nickel-based superalloy, few observations are made:

- The flow softening phenomenon. Flow softening is a phenomenon induced by dynamic recrystallization and recovering. In this research, flow softening is a function of strain and temperature coupling effect, which was observed for 1033K and 1144K.
- Anomalous strengthening phenomenon. This phenomenon is observed at temperature around 1033K.

- Difference in strain hardening. By comparing the four strain-stress curves between yield point and ultimate tensile strength section, material performance is distinctively different, which is due to the changes in γ and γ' microstructure [25].

Constitutive models are widely used to depict the material flow stress during plastic deformation. Among these constitutive models, Johnson-Cook (J-C) model is highly recommended in machining investigation, which is under high strain rate and high temperature environment. The existing Johnson-Cook constitutive model must be modified for γ'-strengthened nickel-based superalloy, and the modifications must address these observations, such that the predictions of the new model demonstrate improvement. The flow scheme of developing a modified Johnson-Cook model is shown in Figure 32.

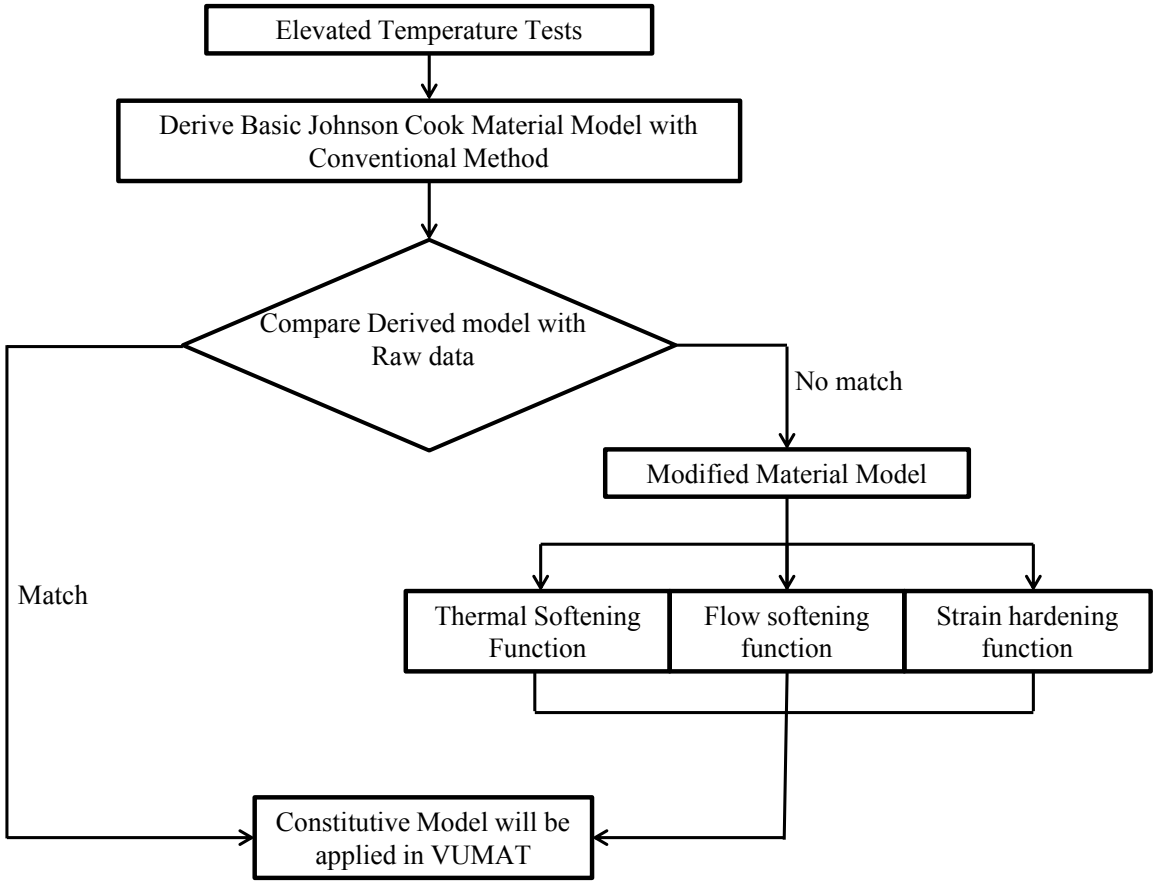

Figure 32: Flow scheme of developing material model.

Johnson-Cook Model

Johnson-Cook constitutive model depicts the flow stress as a function of strain, strain rate and temperature, and it is commonly embedded into commercial finite element analysis software, such as AdvantEdge and ABAQUS. Johnson-Cook model given in equation (3.5) is based on the experimental data obtained from elevated temperature tensile/compression test with different strain rate [58]. In this material model, strain hardening, strain rate sensitivity and thermal softening are considered.

$$\sigma = \left(A + B\varepsilon^n\right)\left(1 + C\ln\frac{\dot{\varepsilon}}{\dot{\varepsilon}_0}\right)\left(1 - \left(\frac{T - T_r}{T_m - T_r}\right)^m\right), \tag{3.5}$$

where σ is equivalent flow stress, ε is equivalent plastic strain, $\dot{\varepsilon}$ is strain rate, T is temperature of material, T_m is the melting temperature, $\dot{\varepsilon}_0$ is the reference strain rate, T_r is the reference temperature. A, B, m and n are the four coefficients needed to be empirically determined. Elevated temperatures tests were performed with constant strain rate. So, strain rate sensitivity is not taken into consideration at this moment. As the flow chart in Figure 32 shown, the basic Johnson-Cook material model needs to be developed and compared with experimental data. In order to obtain the coefficients of basic Johnson-Cook model, strain hardening must to be determined first.

Determine Strain Hardening Coefficients

At this step, the reference temperature is set to 294K (room temperature), so the Johnson-Cook model can be written as modified power law, as follows:

$$\sigma = A + B\varepsilon^n, \tag{3.6}$$

After applying natural logarithm to both side of the equation, equation (3.7) is obtained:

$$\ln(\sigma - A) = \ln B + n\ln\varepsilon, \tag{3.7}$$

Using the least square method, as shown in Figure 33, the coefficients A, B and n are obtained as follows:

$$A = 975$$
$$B = 1.97 \times 10^3, \tag{3.8}$$
$$n = 0.79$$

After replacing the numerical values, the strain hardening term of the Johnson-Cook model can be written as follows:

$$\sigma = 975 + 1.97 \times 10^3 \cdot \varepsilon^{0.79}, \tag{3.9}$$

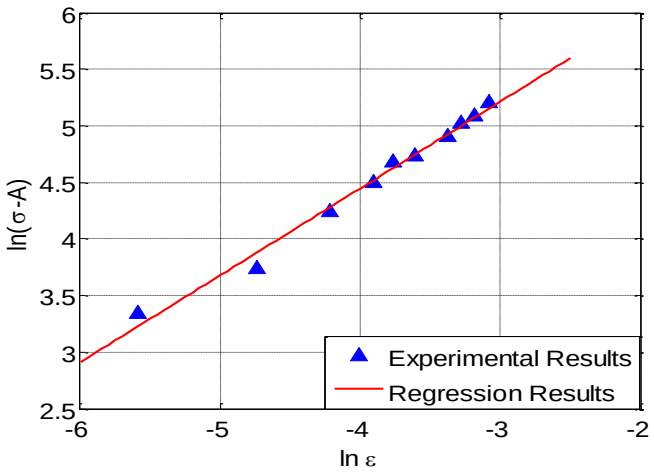

Figure 33: Least square method is used to determine the coefficients A, B and n.

The strain hardening term in Johnson-Cook model determines nonlinear relation between equivalent plastic strain and effective stress. This term is also referred to as work hardening function, and it quantifies the work hardening due to dislocation generation and dislocation movements. In Figure 34, the obtained strain hardening function is compared with the true strain and stress data from experiment for the temperature of 294K. As it is expected, the model has a good fit with experimental data.

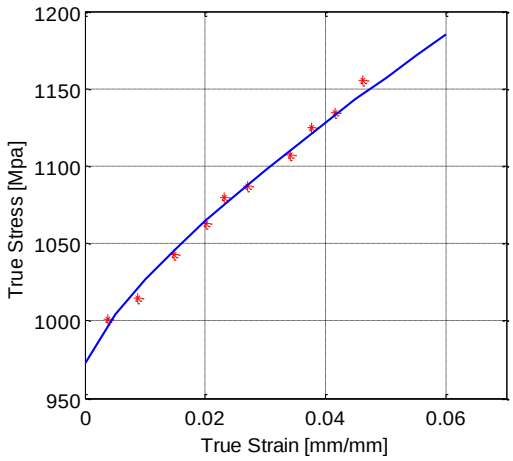

Figure 34: Strain hardening function compared with experimental data for the temperature of 294K.

Determine Thermal Softening Coefficients

After including the strain hardening term, the Johnson-Cook model can be written as follows:

$$\sigma = \left(975 + 1.97 \times 10^{3} \cdot \varepsilon^{0.79}\right)\left(1 - \left(\frac{T - T_r}{T_m - T_r}\right)^{m}\right), \tag{3.10}$$

In order to obtain the linear relationship between temperature and effective stress, equation (3.10) is modified by taking natural logarithm to both sides of equation. Then, equation (3.11) is obtained as:

$$\ln\left(1 - \frac{\sigma}{\left(A + B\varepsilon^{n}\right)}\right) = m \ln\left(\frac{T - T_r}{T_m - T_r}\right), \tag{3.11}$$

The coefficient m is the unknown to be determined and T is instant temperature. The melting temperature is T_m=1523K [69]. The anomalous behavior observed at 1033K

is not yet taken into consideration at this point, but only the behavior at 922K, 1144K and 1523K (melting temperature). The data from these three temperatures are plotted in Figure 35 with red dots. Figure 35 also shows the regression method used to determine the coefficient as m=3.1. After replacing this value, the Johnson-Cook is written as in equation(3.12), and plotted in Figure 36.

$$\sigma = \left(975 + 1.97\times10^{3}\cdot\varepsilon^{0.79}\right)\left(1-\left(\frac{T-T_r}{1523-T_r}\right)^{3.1}\right), \tag{3.12}$$

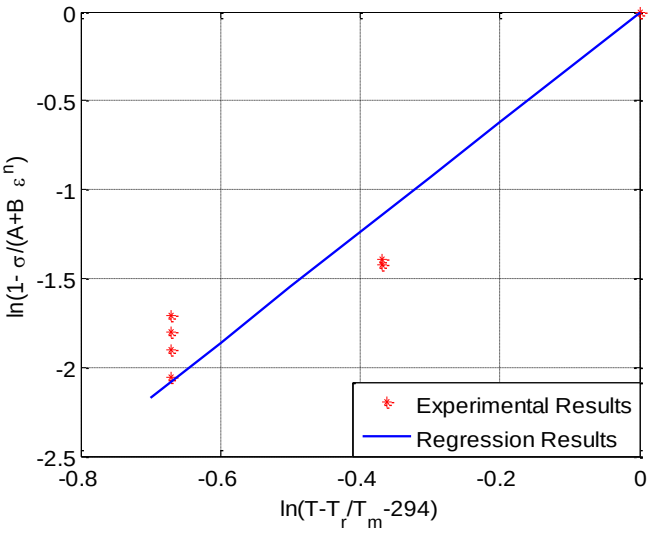

Figure 35: Linear fit is used to determine the coefficient m.

As Figure 36 shown, this model is able to predict material behavior at referenced temperature (294K). For 1033K, this model does not accurately match the experimental results, as expected due to the anomalous strengthening phenomenon. However, for temperatures of 922K and 1144K, this derived basic Johnson-Cook model failed to

predict the experimental data as well, due to taking 1523K into consideration. Thus, to satisfy the melting point, the accuracy at lower temperature range is sacrificed.

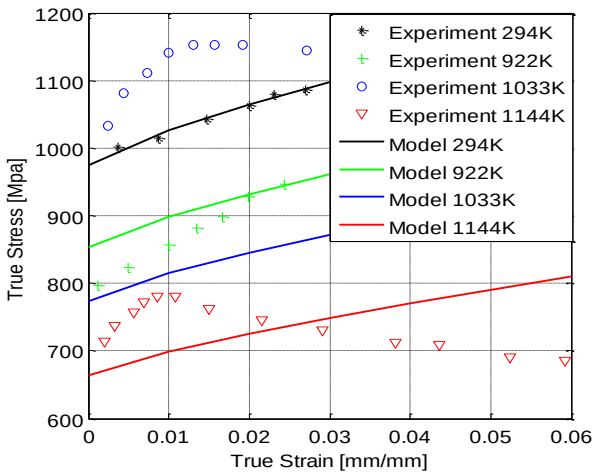

Figure 36: Johnson-Cook model compared with experimental data.

Modified Johnson-Cook Model

In this research, during machining on γ' strengthened nickel-based superalloy process, the temperature does not reach the melting temperature. Thus, compared to melting temperature, the temperatures at lower range (room temperature to 1144K) are more important to this research. In order to obtain more accurate predictions for thermal softening function, the constitutive model is modified and the steps followed are described below.

Improve Thermal Softening Function $f_{Ts(T)}$

Thermal softening phenomenon has been observed for most types of materials. In this research, since it is proven that the basic thermal softening function is not able to

depict the temperature influence on the plastic behavior, an exponential term is proposed to be multiplied into the thermal softening function, as shown in equation (3.13):

$$\sigma = \left(A + B\varepsilon^{n}\right)\left(1 - e^{h}\left(\frac{T - T_r}{T_m - T_r}\right)^{m}\right), \tag{3.13}$$

The new coefficients, *m* and *h*, are determined using the data for the temperatures of 922K and 1144K by linear regression method from slope and intercept respectively, which is shown in Figure 37.

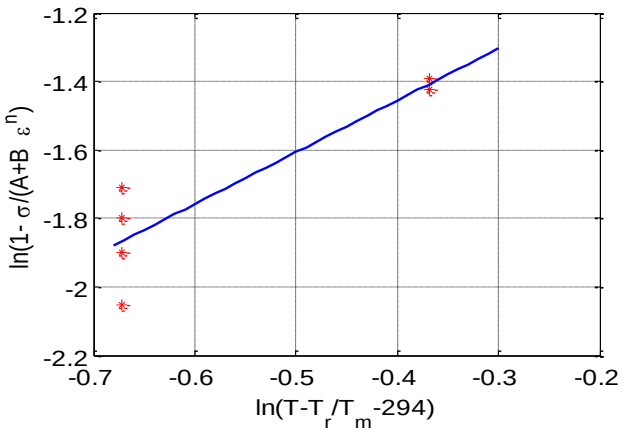

Figure 37: Linear fit used to determine coefficients *m* and *h*.

With the linear fitted coefficients *m*=1.5 and *h*=-0.85, the modified material model is expressed in equation (3.14):

$$\sigma = \left(975 + 1.97\times10^{3}\varepsilon^{0.79}\right)\left(1 - e^{-.85}\left(\frac{T - T_r}{1523 - T_r}\right)^{1.5}\right), \tag{3.14}$$

With the improved thermal softening function, the model is compared with experimental data in Figure 38.

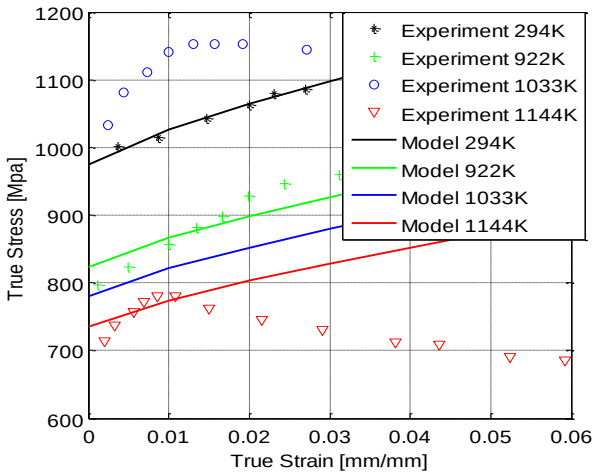

Figure 38: Modified Johnson-Cook model is compared with experimental data.

In equation (3.14), since the melting temperature point is not take into consideration, there are errors for ~1523K. However, after analyzing and comparing Figure 36 to Figure 38, it is concluded that the modified thermal softening function significantly improved the accuracy at temperatures of 294K, 922K and 1144K, which covers the cutting zone temperature range [68]. The results are re-plotted in Figure 39 for the entire strain range.

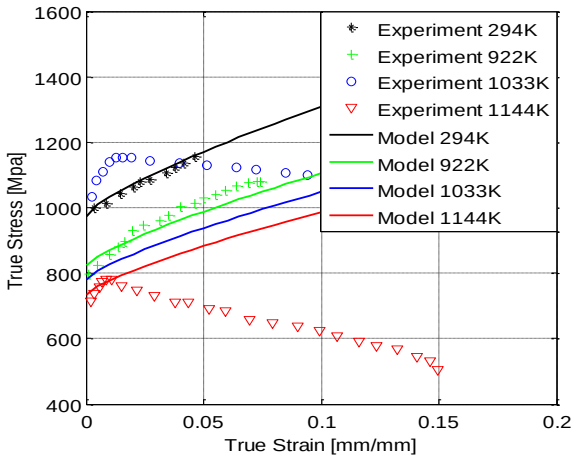

Figure 39: Although improvement is observed after thermal softening is added, more modifications are needed.

The behavior observed in Figure 39, particularly for the temperatures of 922K and 1033K, is related to the lattice parameters of γ and γ', as explained in the background chapter. At those temperatures, the lattice parameters reach the closest value, thus resulting in reduction of the mismatch at the grain boundary. The inhomogeneity in localized strains increases and the number of slip bands decreases. The density of dislocations increases at the interface of γ and γ', which impedes the further dislocation motion. Therefore, the material exhibits higher strength with increasing temperature, as observed for the temperature of 1033K.

From Figure 39, it is concluded that several functions are needed to merge into basic Johnson-Cook model to depict this material behavior. The modifications proposed for the model include a thermal sensitivity function with piecewise method. Also, the flow softening effect induced by the coupling effect of temperature and must be taken

into consideration. Thus, the proposed modified Johnson-Cook equation can be expressed as:

$$\sigma = f_{A(\varepsilon,T)} \cdot f_{Ts(T)} \cdot f_{S(T)} \cdot f_{F(\varepsilon,T)} \cdot f_{(\dot{\varepsilon})}, \tag{3.15}$$

where $f_{A(\varepsilon,T)}$ is the strain hardening function, which determines the beginning of increasing portion of strain-stress curve; $f_{Ts(T)}$ is the improved thermal softening function, $f_{S(T)}$ is the temperature sensitivity function, which determines the shift in the strain-stress curve, up or down depending on the temperature range; and $f_{F(\varepsilon,T)}$ is flow softening function, which is related to the coupling effects of thermal and strain softening; $f_{(\dot{\varepsilon})}$ is strain rate sensitivity function, which is related to dynamic recrystallization and recovering process.

Determine thermal sensitivity function $f_{S(T)}$

In the temperature range from 294K to 922K, with improved thermal softening term, the constitutive model is written as below:

$$\sigma = f_{A(\varepsilon,T)} \cdot \left(1 - e^{h}\left(\frac{T - T_r}{T_m - T_r}\right)^{m}\right) \cdot f_{T(\varepsilon,T)}, \tag{3.16}$$

However, the anomalous strengthening phenomenon is observed during the experiments for the temperatures between 922K and 1144K, as shown in Figure 40. Due to the anomalous strengthening behavior, this material has unique mechanical property in the high temperature, high pressure environment. However, during machining this alloy, this temperature zone needs to be avoided.

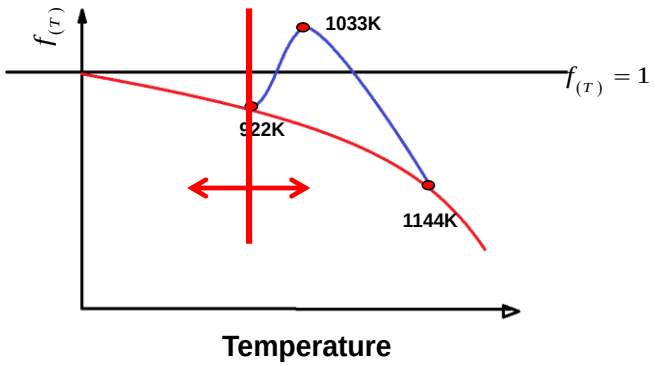

Figure 40: Temperature sensitivity function.

Reflected in $\ln\left(\frac{T-T_r}{T_m-294}\right)$ vs. $\ln\left(1-\frac{\sigma}{\left(A+B\varepsilon^n\right)}\right)$ plot, there are two methods that may be used to depict the anomalous material behavior: ***(i)*** Quadratic function; ***(ii)*** temperature piecewise method, as shown in Figure 41. The linear fit, which is represented with blue line, results in significant error, as shown in the figure.

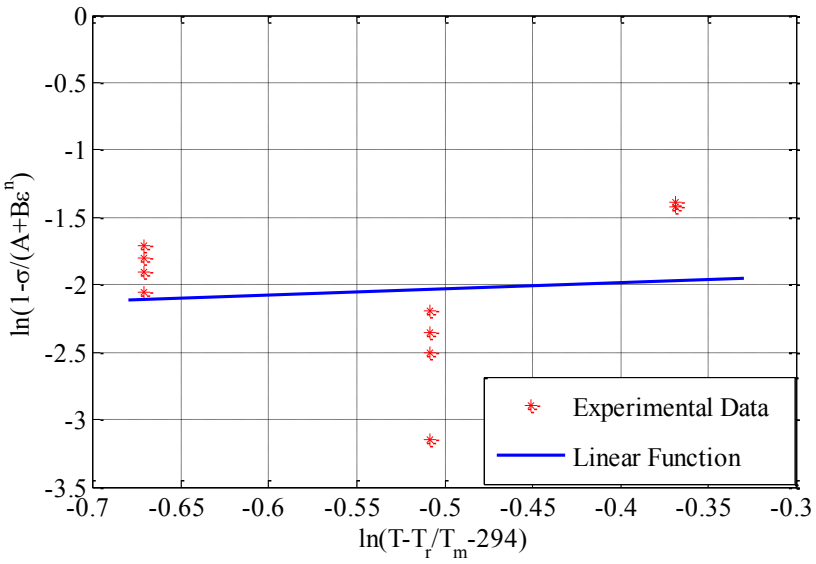

Figure 41: Comparison between novel function and piecewise method.

From Figure 41, it is concluded that for the higher temperature range, quadratic function can not express the material behavior well. So, the piecewise method is chosen to improve the accuracy of this material model. By applying piece-wise method as a function of temperature, equation (3.17) is derived as follows:

$$\sigma = \begin{cases} f_{A(\varepsilon,T)} \cdot \left(1 - e^{h}\left(\dfrac{T - T_r}{1523 - T_r}\right)^{m}\right) & \mathrm{T}_r \le \mathrm{T} < \mathrm{T}_l \\ f_{A(\varepsilon,T)} \cdot \left(q_1 \left(T - T_p\right)^2 + q_2\right) & \mathrm{T}_l \le \mathrm{T} \le \mathrm{T}_m \end{cases} \tag{3.17}$$

In this equation, T_r=294K, T_l=922K, T_p=1033K, and T_m=1523K. Through regression method, the coefficients h, m, q_1 and q_2 are determined. When the temperature is less than 922K, the material model have similar format as the conventional materials, however, when temperature is higher than 922K, the anomalous strengthening behavior is depicted by a quadratic function of temperature.

This thermal sensitivity is explained by the work of Sajjadi *et al*. from the microstructural aspect during tensile testing [27]. Increasing temperature leads to increased number of slip bands and a homogeneous distribution of dislocation structure forms, when the temperature is below 873K. Therefore, higher elongation and lower strength are expected with rising temperature. For the temperatures from 873K to 1023K, the inhomogeneity in localized strains increases and the number of slip plans decreases. Higher density of dislocation forms at γ - γ’ interface and only a few stacking faults are produced. The dislocation tangles formed at γ and γ’ interface impede the movement of dislocation and further elongation. From 1023K to 1173K, dislocations start to appear

within matrix γ and through γ' grain, and stacking faults form in γ' phase at a higher temperature ranges, that reduce the strength of the material again.

Determine flow softening function $f_{F(\varepsilon,T)}$

In the basic Johnson-Cook model, only strain hardening, strain rate sensitivity and thermal softening effects are included, while the strain and temperature coupled softening phenomenon cannot be reflected by the model. For the higher temperatures, beside the dynamic recrystallization and recovering, γ' precipitate starts the coarsening process, which weakens the coherency strain effect at the γ and γ' interface. Since the coupling of temperature and strain softening phenomenon can be only observed at temperature 1033K and above, a switch function is proposed to transfer the monotonic increasing to decreasing during 922K and 1033K, as depicted by equation (3.18):

$$f_{F(\varepsilon,T)} = \tanh\left(\frac{1}{\left[q_3 \cdot \tanh\left(\left(T - T_p\right)/q_4\right) + q_6\right] \cdot \varepsilon}\right)^{q_5}, \tag{3.18}$$

where q_3, q_4 and q_5 are determined from regression method. The coefficients q_3 and q_4 determine how fast the softening effect occurs, while q_5 is applied to enforce the switch function *tanh*. After including the flow softening function into the constitutive model,

Figure 42 is obtained.

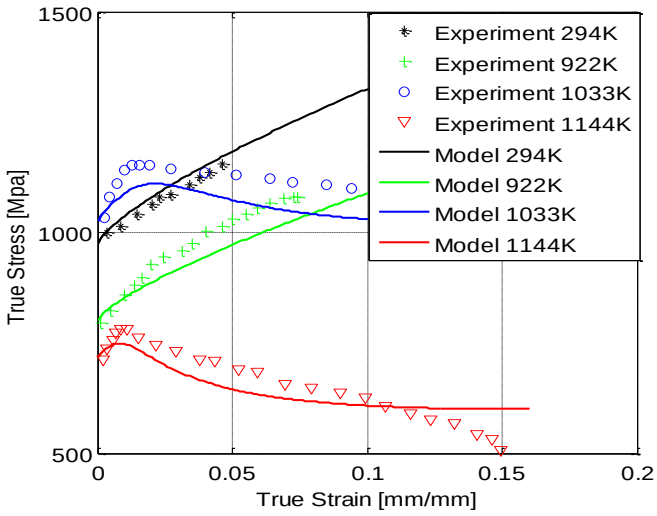

Figure 42: The proposed softening function is included.

As Figure 42 shown, the thermal sensitivity function and flow softening function successfully predicted the thermal softening/hardening and flow softening.

Determine enhanced strain hardening function $f_{n(T)}$

As mentioned before, from Figure 42 it is concluded that between yield point and ultimate tensile strength, the hardening rate is different for low and high temperatures. The higher the temperature is, the larger the slope is observed. This phenomenon is explained as the mismatch between γ and γ' at various temperatures. In a higher temperature range, the transformation between γ and γ' also affects this phenomenon. [23] Therefore, in equation (3.19), the *n*-value in strain hardening function is proposed to be expressed as a function of temperature:

$$f_{A(\varepsilon,T)} = 975 + 1.97\times10^{3}\cdot\varepsilon^{f_{n(,T)}}. \tag{3.19}$$

Between 922K and 1033K, the slope of strain-stress curve changes dramatically, thus a switch function is proposed. The coefficient q_6 describes the rate of mismatch decreasing between γ and γ' phase according to the temperature:

$$f_{n(T)} = \tanh\left(q_7\cdot\left(T - T_l\right) + q_8\right), \tag{3.20}$$

where q_6 and q_7 are obtained using regression method.

Discussion and Concluding Remarks

After including the terms of strain hardening, thermal softening, thermal sensitivity and flow softening, the proposed model is written in equation (3.21). All the coefficients are summarized in Table 6.

$$\sigma = \begin{cases} f_{A(\varepsilon,T)}\cdot\left(1 - e^{h}\left(\dfrac{T - T_r}{1523 - T_r}\right)^{m}\right)\cdot f_{T(\varepsilon,T)} & \mathrm{T}_r \le \mathrm{T} < \mathrm{T}_l \\ f_{A(\varepsilon,T)}\cdot\left(q_1\left(T - T_p\right)^2 + q_2\right)\cdot f_{T(\varepsilon,T)} & \mathrm{T}_l \le \mathrm{T} \le \mathrm{T}_e \end{cases} \tag{3.21}$$

Table 6 Summarized coefficients of the proposed model.

A	B	h	m	q_1	q_2
975MPa	1.97 $\times 10^3$MPa	-0.85	1.3	-1.8	1.05
q_3	q_4	q_5	q_6	q_7	q_8
30	40	0.27	31	-0.07	0.71

In Figure 43, material model is compared with the experimental results demonstrating an improved match with the experimental results.

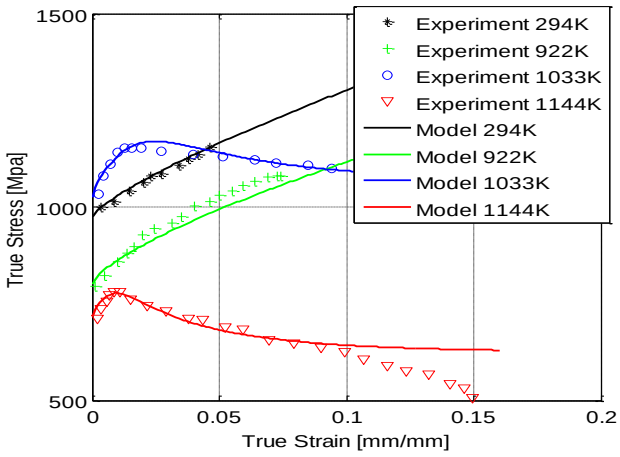

Figure 43: Proposed model compared with experimental results.

In order to quantify the goodness of fit of the model, indicator R-square is applied conform to equation (3.22) to evaluate all tests.

$$R_g^{\,2} = 1 - \frac{\sum\left(\sigma_{Exp}^{i} - \sigma_{Mod}^{i}\right)^2}{\sum\left(\sigma_{Exp}^{i} - \overline{\sigma}\right)^2}, \tag{3.22}$$

where σ_{Exp} is the experimental data, σ_{Mod} is the stress from improved model, $\overline{\sigma}$ is the average value of experimental data. The values of R_g are summarized in

Table 7. It can be observed that the R_g values are close to 1 for all tests, and that indicates good agreement between the proposed model and the experimental data.

Table 7 Goodness of fit.

Temperature [K]	294	922	1033	1144
R_g^2 [%]	99.4	94.3	91.0	84.9

Since the elevated temperature tests were conducted with a constant strain rate, the strain rate sensitivity cannot be derived. For nickel-based superalloys, the dynamic material behavior is not available. By using modified Johnson-Cook model, Ulutan *et al*. [33] concluded that the material (Inconel 718) property performance barely varied associated with increasing strain rate from 10^{-4} s^{-1} to 10^{4} s^{-1}, which is shown in Figure 44.

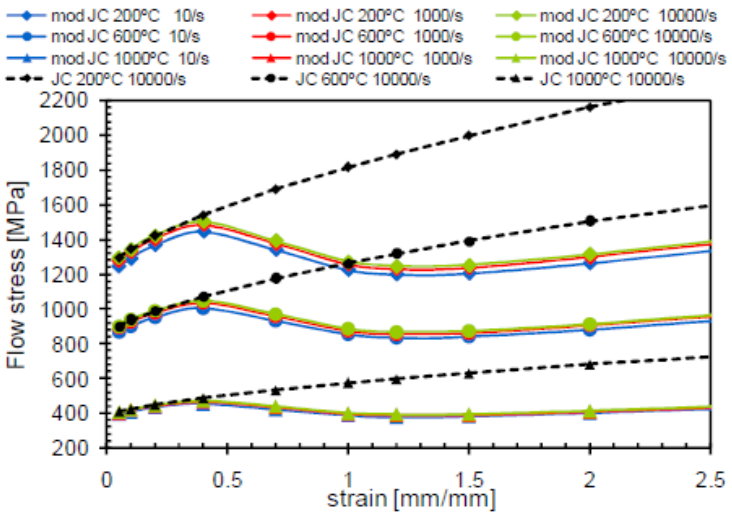

Figure 44: Modified flow stress curves for Inconel 718 [54].

The strain rate function is written as [58]:

$$f_{(\dot{\varepsilon})} = 1 + C \ln \frac{\dot{\varepsilon}}{\dot{\varepsilon}_r}, \tag{3.23}$$

where C is the coefficient of strain rate sensitivity function, $\dot{\varepsilon}$ is the current strain rate, and $\dot{\varepsilon}_r$ is the reference strain rate. From the literature, the strain rate sensitivity for Inconel 718 is summarized in Table 8.

Table 8 Strain rate Sensitivity Summary.

Strain Rate Sensitivity	References
0.0134	[33]
0.017	[61]
0.0132	[9]

With the strain rate sensitivity coefficients from the table, Figure 45 is obtained. It is concluded that for these three values, the difference in the strain rate sensitivity function is within 3%. Meanwhile, within strain rate from 10^{-4} s^{-1} to 10^{4} s^{-1}, the strain rate function $f_{(\dot{\varepsilon})}$ increased within 20%. This shows that the strain rate sensitivity is not a significant factor for nickel based alloys. Therefore, in this research, the material model derived from low strain rate range has been performed in the FEA simulations with strain rate sensitivity value 0.0134.

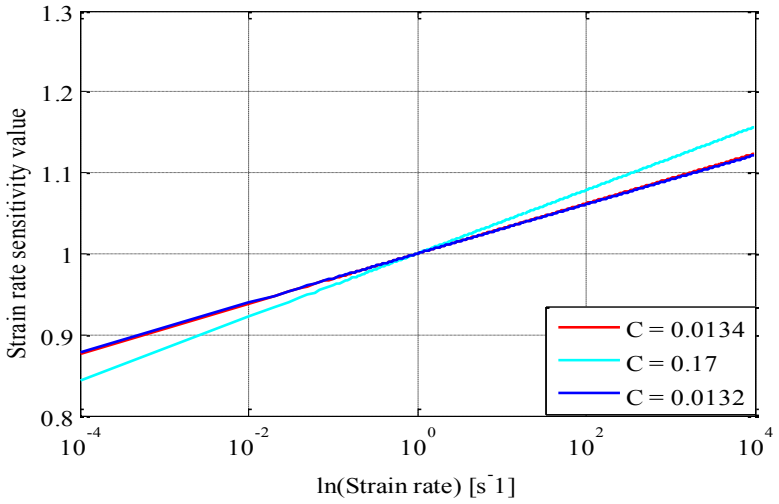

Figure 45: Strain rate Sensitivity Comparison.

In summary, due to the changes in the microstructure of γ and γ', anomalous yield strengthening is observed at high temperature range. This phenomenon is modeled by a proposed temperature sensitivity function, $f_{S(T)}$. GTD111 exhibited two different types of plastic behavior as a function of temperature, so piece-wise method is applied to depict this behavior at different temperature ranges. Since the strain hardening term in the Johnson-Cook model is not able to depict this particular behavior, a strain hardening function, $f_{A(\varepsilon,T)}$, and a *n*-value function, $f_{n(T)}$, are introduced to improve the accuracy of the model. Under the assumption that the softening phenomenon is induced by the coupling effect of temperature and strain, flow softening function $f_{F(\varepsilon,T)}$ is introduced into the constitutive model to express the flow softening phenomenon for the higher temperature region. The strain rate sensitivity coefficient is adopted from the previous

research on Inconel 718. The final constitutive model of GTD111 is given by equation (3.24).

$$\sigma = \begin{cases} f_{A(\varepsilon,T)} \cdot \left(1 + C \ln \dfrac{\dot{\varepsilon}}{\dot{\varepsilon}_r}\right) \cdot \left(1 - e^{h}\left(\dfrac{T - T_r}{1523 - T_r}\right)^{m}\right) \cdot f_{T(\varepsilon,T)}, & \mathrm{T}_r \le \mathrm{T} < \mathrm{T}_l \\ f_{A(\varepsilon,T)} \cdot \left(1 + C \ln \dfrac{\dot{\varepsilon}}{\dot{\varepsilon}_r}\right) \cdot \left(q_1 \left(T - T_p\right)^2 + q_2\right) \cdot f_{T(\varepsilon,T)}, & \mathrm{T}_l \le \mathrm{T} \le \mathrm{T}_m \end{cases} \tag{3.24}$$

CHAPTER FOUR

FINITE ELEMENT MODELING

The previous chapter presented the development of a modified Johnson-Cook constitutive model has been proposed for GTD111. In this chapter, the material model is incorporated in the finite element analysis. A user defined material subroutine (VUMAT) integrates Johnson-Cook constitutive model by FORTRAN code, which is shown in Appendix A. The subroutine is called at each calculation point in FEA, in order to update the stress components according to the mechanical constitutive behavior of the material. By developing stress updating subroutine, the user can define various material constitutive models, which is not limited within the existing models. Meanwhile, the user can update the state variables and output any history and field variables from finite element analysis process. For, this stress update subroutine, two methods (explicit and implicit) is compared on one element analysis. Then, orthogonal cutting FEA simulation on GTD111 is implemented with validated explicit subroutine by applying modified Johnson-Cook material model. After the validation via experiments, more FEA simulation is carried out and their results is used to derive subsurface damage data for orthogonal cutting processes under various cutting conditions.

Solving method in finite element analysis

There are several hardening phenomena widely accepted. After the linear relationship between the strain, ε, and the stress, σ, in the elastic portion, the strain continues increasing without any increment from the stress or external load for ideal

plastic hardening, or follows the linear relationship in linear strain hardening. Also, strain hardening phenomenon follows power law, as shown in

Figure 46. Johnson-Cook model is a modified power law model with strain rate and thermal sensitivity considerations.

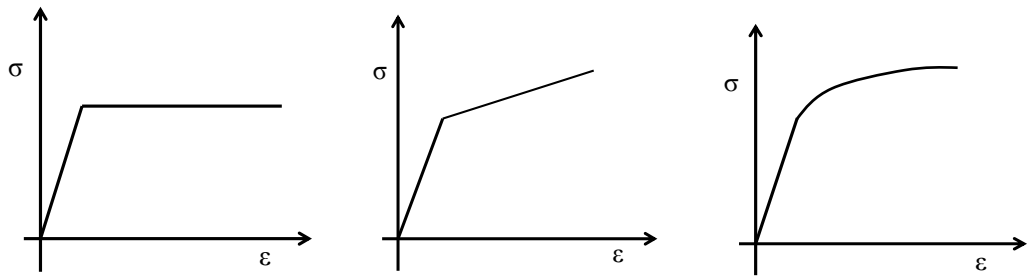

Figure 46: Ideal plastic hardening, Linear strain hardening and Power law hardening.

For isotropic material, during the non-linear deformation, the yield surface expands in all directions uniformly. In this chapter, first Johnson-Cook model is selected as constitutive model during developing the stress update subroutine. Since this model is already embedded in ABAQUS software, it is used as the comparison for subroutine development. After Johnson-Cook model is validated in subroutine, the modified constitutive model is applied to develop the orthogonal cutting simulation on GTD111. The yield function is defined as:

$$f = \sigma_e - \sigma_p^y = 0, \tag{4.1}$$

where $\sigma_p^y = \sigma_0^y + r(p)$, σ_p^y is the new yield surface value, σ_0^y is the original yield surface value and $r(p)$ is hardening function shown in Figure 47. In Figure 47, on the left side, is

the principal stress plane showing the yielding surface of the isotropic material expanded with the uniaxial stress increment $r(p)$.

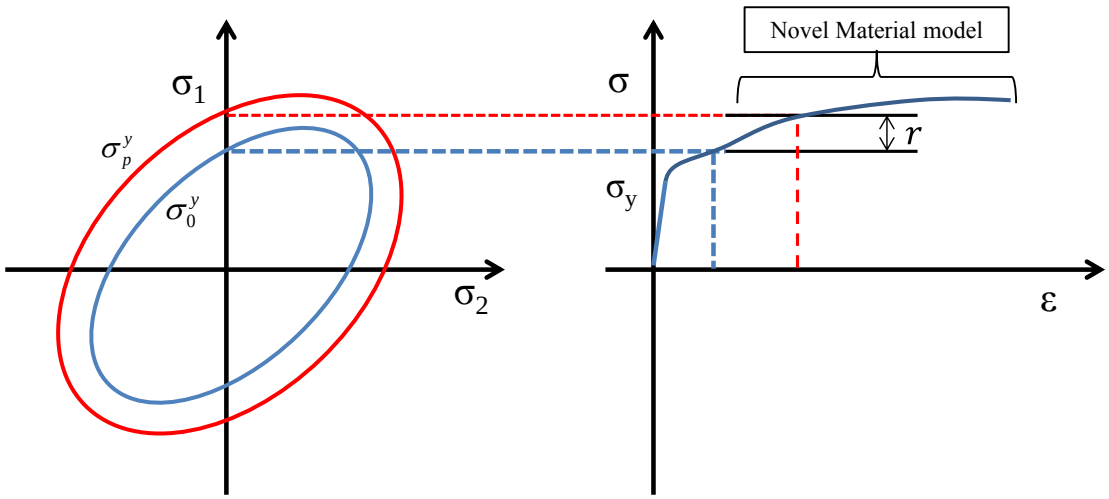

Figure 47: Yield surface expands when material undertakes plastic deformation.

Figure 48 shows how stress update subroutine is developed. In this research, there are two different schemes (explicit and implicit) are introduced, which is explained in the following sections.

As the flow chart shows, the subroutine is called to update the strain at each calculation point. At zero step time, the initial values is input into stress update subroutine with initial $\Delta\varepsilon$ =10E^{-10} at each integration point. Then the trace strain is obtained from three initial strain increments. The tress components induced by trace strain is calculated by Hooke's law at each integration points. Deviatoric stress is derived based on the updated stress components and hydrostatic stress. Trial stress (von Mises stress) is derived to compare with the original yield surface in order to judge if the

material has yielded. If the material has not yield yet, the stress update is completed with a linear calculation, $\sigma_{t+\Delta t} = \sigma_t + \Delta\sigma$. If the material exceeds the yield surface, the plastic flow theory is applied to determine the equivalent plastic strain increment. Radius return method is applied to drag trial stress back to the yield surface. There are two schemes, explicit and implicit, that calculate the increment of equivalent plastic strain and bring the stress components back to the yield surface. These two algorithms are compared in the following section.

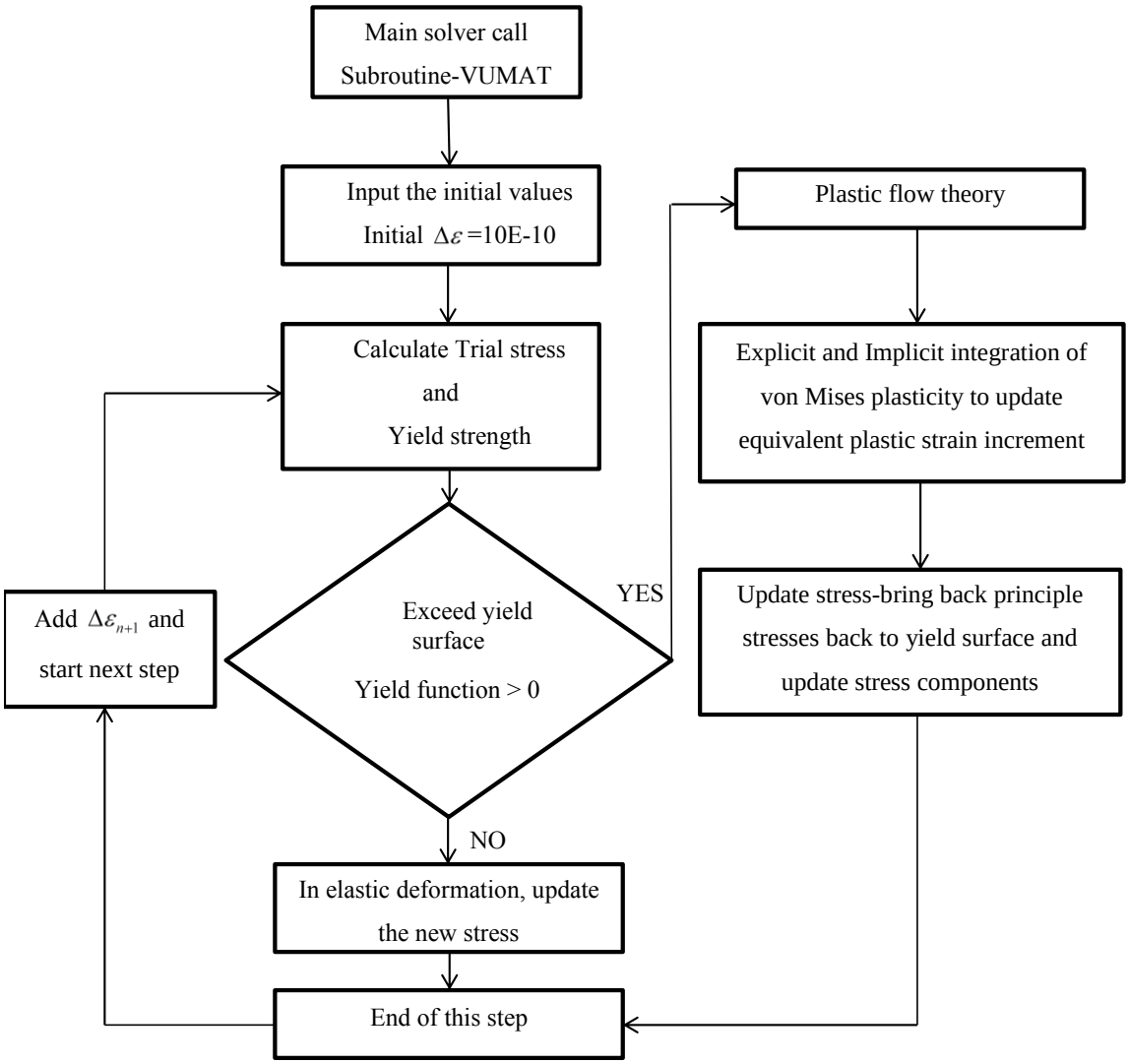

Figure 48: Flow chart of stress update in user defined subroutine.

Explicit Scheme

In this section, explicit scheme is explained and applied for Johnson-Cook constitutive model. From the elastic theory and computational plasticity [73], it is conclude that:

$$G=\frac{E}{2(1+\nu)}, \tag{4.2}$$

$$\lambda=\frac{E\cdot\nu}{(1-2\nu)\cdot(1+\nu)}, \tag{4.3}$$

where E is young's modulus, ν is Poisson ratio, λ is first Lame parameter and G is second Lame factor, which is also named as shear modulus.

In this subroutine, when step time is zero, the initial parameters are defined and the initial trace strain and stress are calculated. After the time starts to increase by Δt, according to Hooke's law:

$$\boldsymbol{\sigma}=2G\cdot\boldsymbol{\varepsilon}+\lambda\cdot tr(\boldsymbol{\varepsilon})\cdot\mathbf{I}, \tag{4.4}$$

where $\boldsymbol{\sigma}$ is stress component tensor, G is shear modulus (first Lame factor), λ is second Lame factor, $\mathbf{I}$ is unit matrix and $tr(\boldsymbol{\varepsilon})$ is the trace strain. Also, equation (4.4) can be written as equation (4.5) in term of tensors.

$$\begin{bmatrix}\sigma_{11} & \sigma_{12} & \sigma_{13}\\ \sigma_{21} & \sigma_{22} & \sigma_{23}\\ \sigma_{31} & \sigma_{32} & \sigma_{33}\end{bmatrix}=2\cdot G\cdot\begin{bmatrix}\varepsilon_{11} & \varepsilon_{12} & \varepsilon_{13}\\ \varepsilon_{21} & \varepsilon_{22} & \varepsilon_{23}\\ \varepsilon_{31} & \varepsilon_{32} & \varepsilon_{33}\end{bmatrix}+\lambda^{e}\cdot\sum_{i=1}^{3}\varepsilon_{ii}\cdot\begin{bmatrix}1 & 0 & 0\\ 0 & 1 & 0\\ 0 & 0 & 1\end{bmatrix}, \tag{4.5}$$

where σ_{ij} is stress components. If hydrostatic stress and strain are defined as

$$\sigma_m = \frac{1}{3}\left(\sigma_{11} + \sigma_{22} + \sigma_{33}\right) \tag{4.6}$$

$$\varepsilon_m = \frac{1}{3}\left(\varepsilon_{11} + \varepsilon_{22} + \varepsilon_{33}\right) \tag{4.7}$$

where σ_m is hydrostatic stress. The stress components are written as:

$$\begin{aligned}
\sigma_{11} &= \lambda \cdot \left(\varepsilon_{11} + \varepsilon_{22} + \varepsilon_{33}\right) + 2 \cdot G \cdot \varepsilon_{11} = 3 \cdot \lambda \cdot \varepsilon_m + 2 \cdot G \cdot \varepsilon_{11} \\
\sigma_{22} &= 3 \cdot \lambda \cdot \varepsilon_m + 2 \cdot G \cdot \varepsilon_{22} \\
\sigma_{33} &= 3 \cdot \lambda \cdot \varepsilon_m + 2 \cdot G \cdot \varepsilon_{33} \\
\sigma_{12} &= 2 \cdot G \cdot \varepsilon_{22} \\
\sigma_{23} &= 2 \cdot G \cdot \varepsilon_{22} \\
\sigma_{13} &= 2 \cdot G \cdot \varepsilon_{13}
\end{aligned} \tag{4.8}$$

Since the hydrostatic stress does not bring plastic deformation, the deviatoric stress which is shown in equation (4.9), is used for effective stress calculation.

$$\begin{aligned}
\sigma'_{11} &= \sigma_{11} - \sigma_m = 2 \cdot G \cdot \left(\varepsilon_{11} - \varepsilon_m\right) = 2 \cdot G \cdot \varepsilon'_{11} \\
\sigma'_{22} &= 2 \cdot G \cdot \varepsilon'_{22} \\
\sigma'_{33} &= 2 \cdot G \cdot \varepsilon'_{33} \\
\sigma'_{12} &= 2 \cdot G \cdot \varepsilon'_{22} \\
\sigma'_{23} &= 2 \cdot G \cdot \varepsilon'_{22} \\
\sigma'_{13} &= 2 \cdot G \cdot \varepsilon'_{13}
\end{aligned} \tag{4.9}$$

where σ'_{ij} is deviatoric stress. Also, equation (4.9) can be written as:

$$\boldsymbol{\sigma}'_{trial} = \boldsymbol{\sigma} - \frac{1}{3} \cdot Tr\left(\boldsymbol{\sigma}\right) \cdot \mathbf{I} = \boldsymbol{\sigma} - \sigma_m \cdot \mathbf{I} \tag{4.10}$$

where $\boldsymbol{\sigma}'_{trial}$ is deviatoric stress tensor. From equation (4.9), it is concluded that

$$\boldsymbol{\sigma}' = 2 \cdot G \cdot \boldsymbol{\varepsilon}' \tag{4.11}$$

At time $t + \Delta t$, the trail stress is expressed as:

$$ {}_{t+\Delta t}\boldsymbol{\sigma}'_{trial} = {}_{t}\boldsymbol{\sigma}' + 2\cdot G\cdot \Delta\boldsymbol{\varepsilon}'^{\,total}_{t+\Delta t} \tag{4.12} $$

The equivalent trail stress is written with deviatoric stress tensor as:

$$ \sigma^{trial}_{t+\Delta t} = \left(\frac{3}{2}\cdot {}_{t+\Delta t}\boldsymbol{\sigma}'_{trial} : {}_{t+\Delta t}\boldsymbol{\sigma}'_{trial} \right)^{1/2} \tag{4.13} $$

The next step is comparing the new updated von Mises equivalent trial stress to the yield stress. In another words, the yield function

$$ f = {}_{t+\Delta t}\sigma_{trial} - \sigma^{y}{}_{t+\Delta t}, \tag{4.14} $$

is compared with zero to determine if the material is still in elastic deformation or it enters into plastic deformation phase.

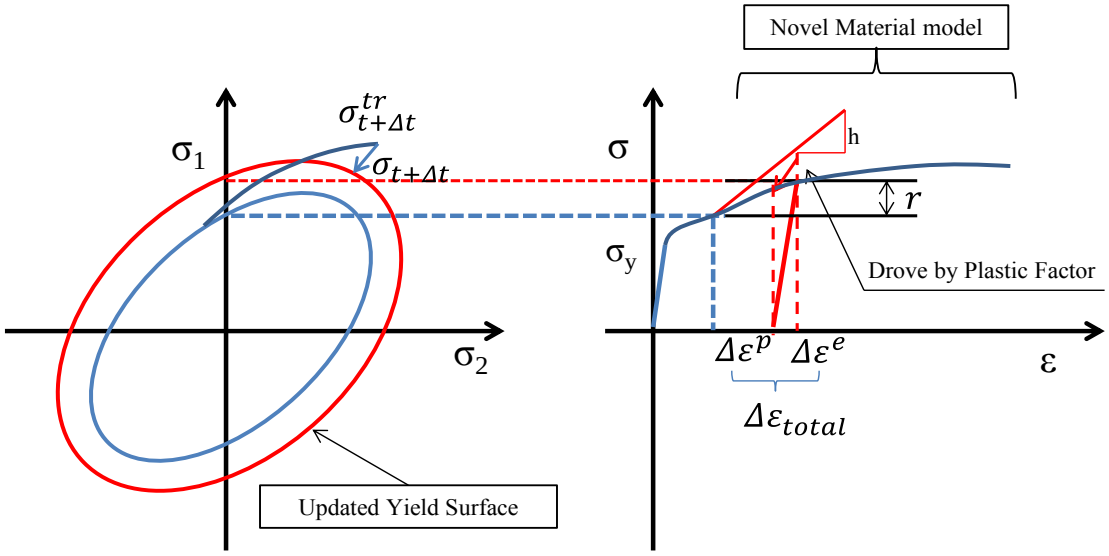

Figure 49: Radius Return Method by Factor *m*.

If the effective trial stress is outside of yield surface, the material enters into plastic deformation. So, plastic flow theory is adopted for stress update. As Figure 49 shows, at time $t+\Delta t$, the increment of equivalent plastic strain is obtained by explicit

method in this section. Also, as equation (4.15) shows, the deviatoric stress is scaled back to yield surface by a modification factor *m*.

$$ {}_{t+\Delta t}\boldsymbol{\sigma} = m \cdot {}_{t+\Delta t}\boldsymbol{\sigma}'_{trial} \tag{4.15} $$

where

$$ m = \frac{\sigma^{y}_{t+\Delta t}}{\sigma^{tr}_{t+\Delta t}} \tag{4.16} $$

When material enters into plastic deformation range, both elastic and plastic strain are coexist. So in order to obtain the increment of deviatoric plastic strain $\Delta\boldsymbol{\varepsilon}'^{\,p}_{t+\Delta t}$, the deviatoric elastic strain increment $\Delta\boldsymbol{\varepsilon}'^{\,ela}_{t+\Delta t}$ is subtracted from total deviatoric strain increment $\Delta\boldsymbol{\varepsilon}'^{\,total}_{t+\Delta t}$, which is shown in equation (4.17).

$$ \Delta\boldsymbol{\varepsilon}'^{\,p}_{t+\Delta t} = \Delta\boldsymbol{\varepsilon}'^{\,total}_{t+\Delta t} - \Delta\boldsymbol{\varepsilon}'^{\,ela}_{t+\Delta t} = \Delta\boldsymbol{\varepsilon}'^{\,total}_{t+\Delta t} - \frac{\left({}_{t+\Delta t}\boldsymbol{\sigma}' - {}_{t}\boldsymbol{\sigma}'\right)}{2 \cdot G} \tag{4.17} $$

From equation (4.12), it concluded that the total deviatoric strain increment is written as:

$$ \Delta\boldsymbol{\varepsilon}'^{\,total}_{t+\Delta t} = \frac{{}_{t+\Delta t}\boldsymbol{\sigma}'_{trial} - {}_{t}\boldsymbol{\sigma}'}{2 \cdot G} \tag{4.18} $$

After substituting equation (4.18) into equation (4.17), equation (4.19) is obtained.

$$ \Delta\boldsymbol{\varepsilon}'^{\,p}_{t+\Delta t} = \frac{\left({}_{t+\Delta t}\boldsymbol{\sigma}'_{trial} - {}_{t}\boldsymbol{\sigma}'\right)}{2 \cdot G} - \frac{\left({}_{t+\Delta t}\boldsymbol{\sigma}' - {}_{t}\boldsymbol{\sigma}'\right)}{2 \cdot G} = \frac{\left({}_{t+\Delta t}\boldsymbol{\sigma}'_{trial} - {}_{t+\Delta t}\boldsymbol{\sigma}'\right)}{2 \cdot G} \tag{4.19} $$

In equation (4.19), there are two variables. ${}_{t+\Delta t}\boldsymbol{\sigma}'_{trial}$ is known, but ${}_{t+\Delta t}\boldsymbol{\sigma}'$ is unknown. So in order to solve for $\Delta\boldsymbol{\varepsilon}'^{\,p}_{t+\Delta t}$, equation (4.20) is derived by substituting equation (4.15) into equation (4.19).

$$\Delta\boldsymbol{\varepsilon}_{t+\Delta t}^{'\,p}=\frac{\left({}_{t+\Delta t}\boldsymbol{\sigma}_{trial}^{'}-{}_{t+\Delta t}\boldsymbol{\sigma}^{'}\right)}{2\cdot G}=\frac{(1-m)}{2\cdot G}\cdot{}_{t+\Delta t}\boldsymbol{\sigma}_{trial}^{'} \tag{4.20}$$

In order to reflect stress/strain tensors to equivalent strain and effective stress from material constitutive model, the tensor $\Delta\boldsymbol{\varepsilon}_{t+\Delta t}^{'\,p}$ needs to be expressed as a scalar, $\Delta\varepsilon_{t+\Delta t}^{\;p}$, shown in the following equation

$$\Delta\varepsilon_{t+\Delta t}^{p}=\left(\frac{2}{3}\cdot\Delta\boldsymbol{\varepsilon}_{t+\Delta t}^{'\,p}\cdot\Delta\boldsymbol{\varepsilon}_{t+\Delta t}^{'\,p}\right)^{1/2}=\frac{{}_{t+\Delta t}\sigma_{trial}^{'}-\sigma_{t+\Delta t}^{y}}{3\cdot G} \tag{4.21}$$

As equation (4.21) shows, on the right side, $\sigma_{t+\Delta t}^{y}$ is still unknown. Taylor expansion, which is show in equation (4.22), is applied to transfer the nonlinear relationship to linear.

$$\sigma_{t+\Delta t}^{y}=\sigma_{t}^{y}+\frac{\partial\sigma_{t}^{y}}{\partial\varepsilon^{p}}\cdot\Delta\varepsilon_{t+\Delta t}^{p}+....(\text{higher order terms}), \tag{4.22}$$

The higher order items is neglected. Thus, the increment of plastic strain is derived as:

$$\Delta\varepsilon_{t+\Delta t}^{p}=\frac{\sigma_{t+\Delta t}^{trial}-\sigma_{t}^{y}}{3\cdot G+\dfrac{\partial\sigma_{t}^{y}}{\partial\varepsilon^{p}}}, \tag{4.23}$$

With the increment of strain, the trail stress $\sigma_{t+\Delta t}^{tr}$ can be obtained at $t+\Delta t$. The other factors is derived from time *t*. Then, from equation (4.23), the $\Delta\varepsilon_{t+\Delta t}^{p}$ is obtained based on Johnson-Cook constitutive model. If the trial stress excesses yield surface, yield function takes partial differential of equivalent plastic strain:

$$h=\frac{\partial\sigma_t^y}{\partial\varepsilon^p}=\left[B\cdot n\cdot\varepsilon_{t+\Delta t}^p\right]\cdot\left[1+C\ln\left(\frac{\Delta\varepsilon_{t+\Delta t}^p\Big/dt}{\dot{\varepsilon}_r}\right)\right]\cdot\left(1-\left(T^*\right)^m\right)+ \\ \left(A+B\cdot\varepsilon_{t+\Delta t}^p\right)\cdot\left(C\Big/\Delta\varepsilon_{t+\Delta t}^p\right)\cdot\left(1-\left(\frac{T-T_r}{T_m-T_r}\right)^m\right) \quad , \tag{4.24}$$

From equation (4.23) and equation (4.24), the increment of equivalent plastic strain is:

$$\Delta\varepsilon_{t+\Delta t}^p=\frac{\sigma_{t+\Delta t}^{tr}-\sigma_t^y}{3\cdot G+h}\,, \tag{4.25}$$

As, equation (4.25) shown, the increment of equivalent plastic strain at $t+\Delta t$ is calculated from the variables at time *t*. At $t+\Delta t$, the new updated equivalent plastic strain is obtained as:

$$\varepsilon_{t+\Delta t}^p=\varepsilon_t^p+\Delta\varepsilon_{t+\Delta t}^p\,, \tag{4.26}$$

The updated yield strength is derived as:

$$\sigma_{t+\Delta t}^y=\left(A+B\cdot\varepsilon_{t+\Delta t}^p\right)\cdot\left[1+C\ln\left(\frac{\Delta\varepsilon_{t+\Delta t}^p}{\Delta t}\right)\right]\cdot\left(1-\left(T^*\right)^m\right), \tag{4.27}$$

However, since at $t+\Delta t$, explicit method does not ensure that the yield function f is always zero, the solution may drift from yield surface and lead to inaccurate results. Also, this explicit scheme is conditional stable. In conclusion, the time step needs to be carefully determined and the load increment needs to be small enough to ensure the precision. This means that longer computer time is needed to implement the calculation. In the subroutine, radius return method is applied to solve the offset of yield surface problem. A correction factor is multiplied on the trial stress to bring it back to the yield

surface. The correction factor is calculated by $m = \frac{\sigma^{y}_{t+\Delta t}}{\sigma^{tr}_{t+\Delta t}}$ and the trial stress back is brought back to the yield surface by

$$\boldsymbol{\sigma}_{t+\Delta t} = \boldsymbol{\sigma}^{'}_{t+\Delta t} \cdot m + \sigma_m \cdot \boldsymbol{I} \tag{4.28}$$

At $t+\Delta t$, the inelastic specific internal energy ΔE_{inela} is the reason to induce the temperature change, which is calculated as follows:

$$E^{Inelas}_{t+\Delta t} = E^{Inelas}_{t} + \Delta E^{Inelas}, \tag{4.29}$$

$$\Delta E_{inela} = \sigma^{y}_{t+\Delta t} \cdot \Delta \varepsilon^{p}_{t+\Delta t}, \tag{4.30}$$

$$\Delta E_{inela} = C \cdot M \cdot \Delta T, \tag{4.31}$$

where ΔE_{inela} is inelastic specific internal energy, M is mass and ΔT is the increase in temperature. Assuming that 90% internal energy is dissipated by workpiece during deformation process [65], the increment of temperature is written as:

$$\Delta T = \frac{0.9 \cdot \sigma^{y}_{t+\Delta t} \cdot \Delta \varepsilon^{p}_{t+\Delta t}}{C \cdot \rho}, \tag{4.32}$$

Meanwhile, the raised temperature induces thermal strain, which is calculated by:

$$\varepsilon_T = \alpha \cdot \Delta T, \tag{4.33}$$

where ε_T is thermal strain. According to Hooke's law, thermal stress is given by:

$$\sigma_T = E \cdot \alpha \cdot \Delta T, \tag{4.34}$$

The stress components $\boldsymbol{\sigma}$ is updated by thermal stress $\boldsymbol{\sigma}_{\mathrm{T}}$ as shown in equation (4.35)

$$\boldsymbol{\sigma} = \boldsymbol{\sigma}^{'} \cdot m + \sigma_m + \boldsymbol{\sigma}_{\mathrm{T}}, \tag{4.35}$$

So, all the stress components are updated at time $t + \Delta t$.

Implicit Scheme

In this section, the subroutine with implicit method is expained. The difference between implicit and explicit scheme consists in the methodology to solve the increament of equivalent plastic strain and bring the trial stress back to yield surface.

With implicit method, the stress components is guaranteeed on the yield surface. Figure 50 shows the radial return method. When the step time increases by Δt from t, the strain increases by $\Delta t \cdot \dot{\varepsilon}$. By applying Newton iteration method, the plastic strain increment is derived from total strain increment. With this plastic strain increment, an updated yield surface is obtained.

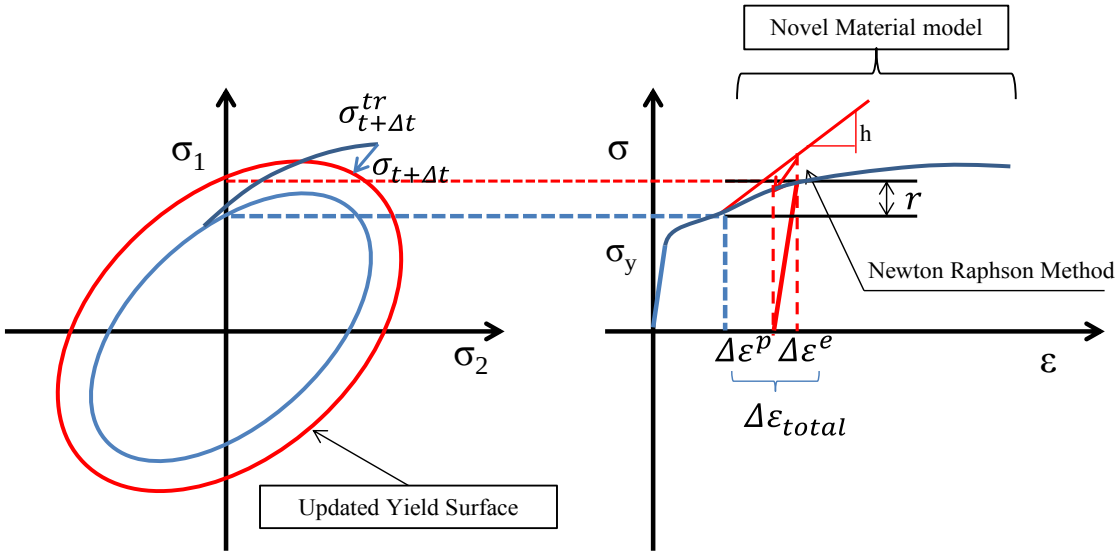

Figure 50: Radius Return Method by Newton-Raphson Method.

Equations (4.36) to (4.38) are employed if plastic deformation occurred. With Hooke's law, the following equations are derived [73].

$$\boldsymbol{\sigma} = 2G \cdot \boldsymbol{\varepsilon}^{e} + \lambda \cdot Tr\left(\boldsymbol{\varepsilon}^{e}\right) \cdot \mathbf{I}, \tag{4.36}$$

$$\boldsymbol{\sigma}'_{trial} = \boldsymbol{\sigma} - \frac{1}{3} \cdot Tr\left(\boldsymbol{\sigma}\right) \cdot \mathbf{I} = \boldsymbol{\sigma} - \sigma_{m} \cdot \mathbf{I} \tag{4.37}$$

$$\sigma_{t+\Delta t}^{trial} = \left(\frac{3}{2} \cdot {}_{t+\Delta t}\boldsymbol{\sigma}'_{trial} : {}_{t+\Delta t}\boldsymbol{\sigma}'_{trial} \right)^{1/2} \tag{4.38}$$

If $\sigma_{t+\Delta t}^{trial}$ exceeds the yield surface, the increment of equivalent plastic strain is written as equation (4.39).

$$\Delta\varepsilon_{t+\Delta t}^{p} = \left(\frac{2}{3} \cdot \Delta\boldsymbol{\varepsilon}'^{\,p}_{t+\Delta t} \cdot \Delta\boldsymbol{\varepsilon}'^{\,p}_{t+\Delta t} \right)^{1/2} = \frac{{}_{t+\Delta t}\sigma'_{trial} - \sigma^{y}_{t+\Delta t}}{3 \cdot G}, \tag{4.39}$$

The multiaxial yield function is defined as

$$f = \sigma_{t+\Delta t}^{tr} - 3G \cdot \Delta\varepsilon_{t+\Delta t}^{p} - \sigma_{t+\Delta t}^{y} = 0, \tag{4.40}$$

$$f' = -3G - \frac{\partial\sigma^{y}}{\partial\Delta\varepsilon_{t+\Delta t}^{p}}, \tag{4.41}$$

In order to solve for the updated $\Delta\varepsilon_{t+\Delta t}^{p}$, Newton-Raphson iteration is applied. At iteration *n*, the yield function is written as:

$$f\left(\Delta\varepsilon_{t+\Delta t}^{p}\right) = 0 \approx f\left({}_{n}\Delta\varepsilon_{t+\Delta t}^{p}\right) + f'\left({}_{n}\Delta\varepsilon_{t+\Delta t}^{p}\right) \cdot \left({}_{n+1}\Delta\varepsilon_{t+\Delta t}^{p} - {}_{n}\Delta\varepsilon_{t+\Delta t}^{p}\right), \tag{4.42}$$

$${}_{n+1}\Delta\varepsilon_{t+\Delta t}^{p} - {}_{n}\Delta\varepsilon_{t+\Delta t}^{p} = d\Delta\varepsilon_{t+\Delta t}^{p} = -\frac{f\left({}_{n}\Delta\varepsilon_{t+\Delta t}^{p}\right)}{f_{t}'\left({}_{n}\Delta\varepsilon_{t+\Delta t}^{p}\right)}, \tag{4.43}$$

During each iteration, after ${}_{n+1}\Delta\varepsilon_{t+\Delta t}^{p}$ being solved, updated yield surface is determined by:

$$f_{t+\Delta t} = \sigma^{tr}_{t+\Delta t} - 3G \cdot \left({}_{n+1}\Delta\varepsilon^{p}{}_{t+\Delta t} \right) - \sigma_{t+\Delta t}{}^{y}, \tag{4.44}$$

At n iterations, if $f_{t+\Delta t}$< 1.e-5, which means the iteration converged. Then, ${}_{n+1}\Delta\varepsilon^{p}_{t+\Delta t}$ is the solution for the yield function at time $t+\Delta t$. With the solution ${}_{n+1}\Delta\varepsilon^{p}_{t+\Delta t}$, the rest steps follow equations from equation (4.26) to equation (4.35).

In conclusion, in this section, two methods (Implicit and Explicit) are introduced for stress update. In order to determine the better method for orthogonal cutting FEA simulation, these two schemes are compared with ABAQUS/CAE based on one element. Several aspects (*i.e.*, CPU time cost, von Mises stress and internal energy from history flied output) are compared in the following section.

Finite Elements Method Simulation Development

In order to investigate the code efficiency and accuracy, the subroutine is first developed for one element. The one element FEA setup is shown in Figure 58. The material is Inconel 718 and the parameters of constitutive model are summarized in Table 9. Young's modulus is defined as 2×10^5 MPa and the plastic property follows Johnson-Cook model.

Table 9 Material properties for one element simulation. [53]

Variables	$\dot{\varepsilon}_r$ $[s^{-1}]$	A [MPa]	B [MPa]	C	m	n
Value	1	450	1700	0.017	1.3	0.65

In Figure 51, on the right side, four nodes are fixed for all the six degrees of freedom. The element is elongated 0.2 mm by defining the velocity and step time at four nodes on the left side.

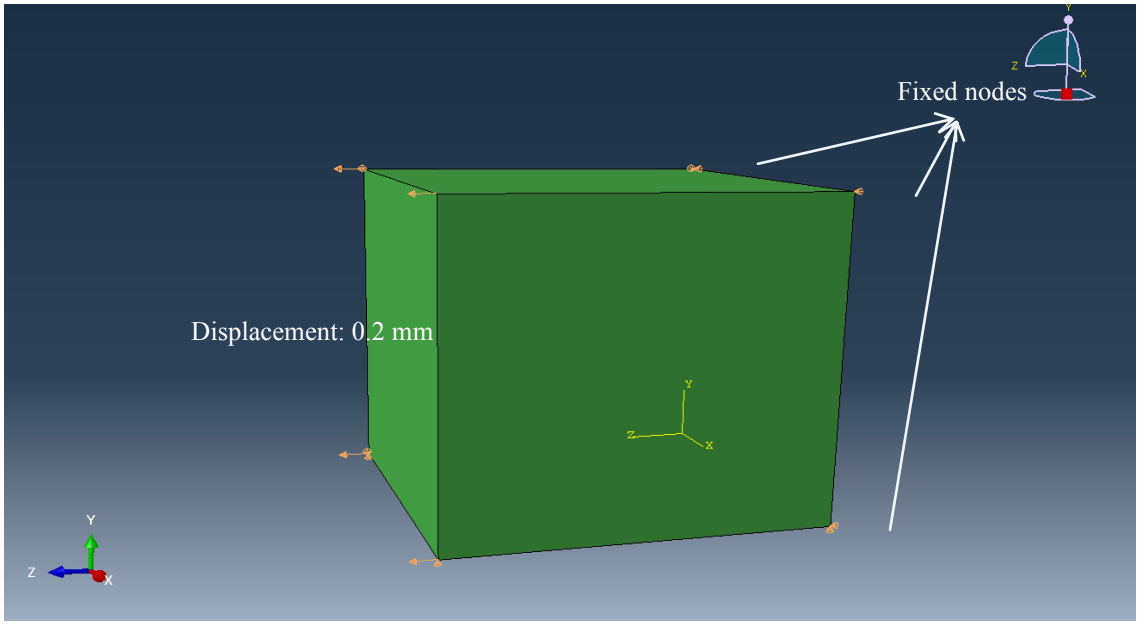

Figure 51: One element FEA model setup.

All the FEA simulations in this research are conducted with ABAQUS 6.10-EF1. Dell precision WorkStation T3500, which is equipped with Intel® Xeon CPU- W3520 @2.67GHz and 24574 MB RAM, is used.

In implicit method code, Newton iteration method is utilized in stress updated subroutine. Thus, an investigation in convergence criterion is necessary for implicit method. Convergence criterion is related to CPU time cost and the accuracy of the result. Three convergence criteria 0.1, 10^{-5}, 10^{-10} are compared.

Figure 52 show the typical von Mises contour from implicit methods with 0.1 convergence criteria, the rest of the results are shown in Appendix B. The stress and CPU time cost are summarized in Table 10.

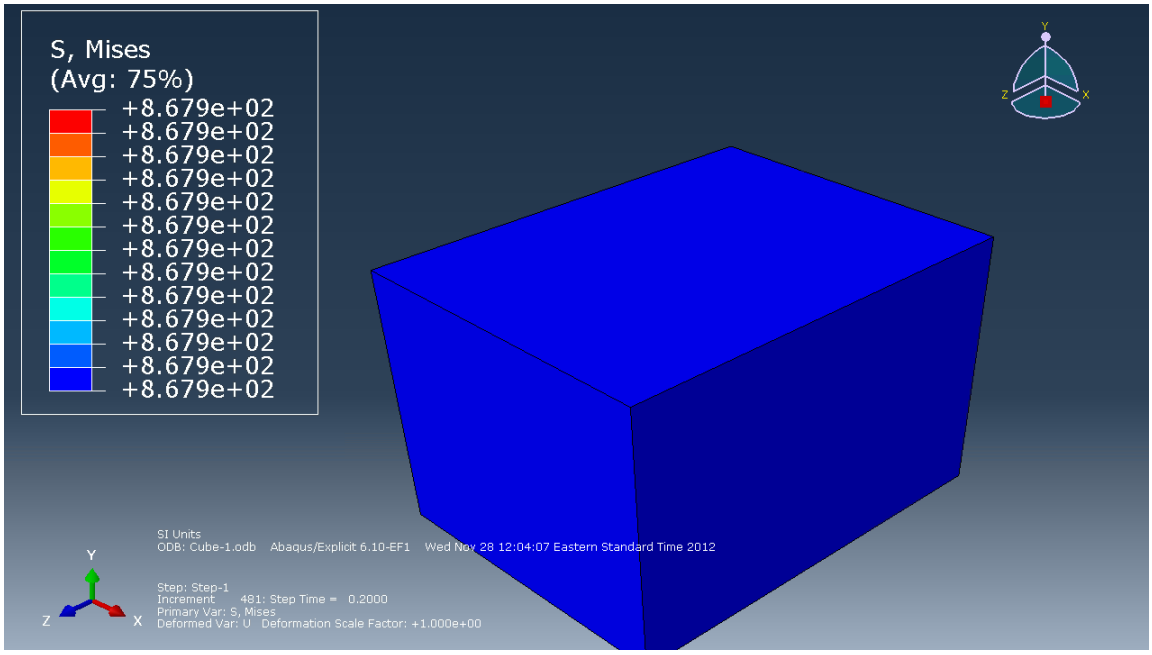

Figure 52: Implicit - One element simulation with convergence criterion 0.1 [stresses unit is MPa].

As shown in Table 10, by decreasing the convergence criterion from 0.1 to 10^{-10}, the CPU time increases twice and the von Mises stress keeps a constant level of 8.683×10^2 MPa when convergence criterion is equal or larger than 10^{-5}. In conclusion, the final value is set to 10^{-5} to make the result accurate and saving CPU cost. The explicit method generates 8.677×10^2 MPa von Mises stress, which is similar to the implicit method. In regard to the CPU time cost, the explicit result keeps the same level with the least CPU time cost from implicit method.

Table 10 CPU Time Cost with Different Methods.

	Implicit Method		Explicit Method	
Convergence Criterion	von Mises Stress (MPa)	CPU Time Cost (s)	von Mises Stress (MPa)	CPU Time Cost (Second)
10^{-1}	8.679×10^2	0.1	8.677×10^2	0.1
10^{-5}	8.683×10^2	0.1		
10^{-10}	8.683×10^2	0.2		

In order to monitor the whole deformation processing instead of the final result at the end of step time (von Mises), history values (Internal Energy) must be compared. The internal energy is defined as: [65]

$$\mathrm{ALLIE} = \mathrm{ALLSE} + \mathrm{ALLPD} + \mathrm{ALLCD} + \mathrm{ALLAE}, \tag{4.45}$$

where ALLIE is the total internal energy, ALLSE is the recoverable strain energy, ALLPD is the plastic dissipation energy, ALLCD is the energy dissipated by creep and viscoelasticity, and ALLAE is the artificial strain energy.

The internal energies from implicit method with various convergence criteria are compared in Figure 53. It is concluded that with three different convergence criteria, the internal energy curve barely changed during the whole step time.

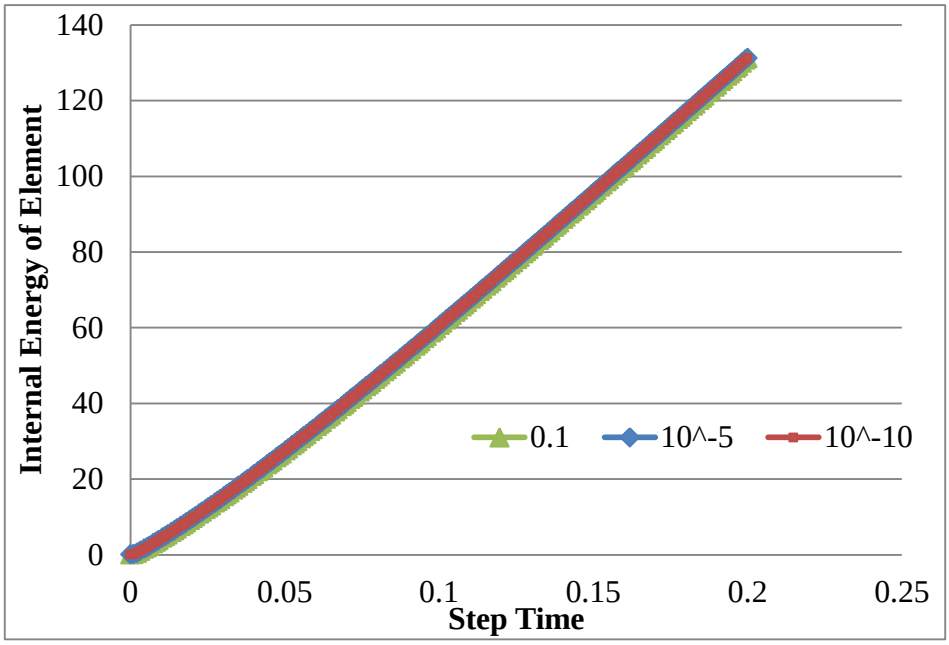

Figure 53: Comparison of internal energy for different convergence criteria.

CAE is a visible operation interface with Johnson-Cook model embedded in ABAQUS, which allows the user to input the six coefficients of the material model directly. By comparing the internal energy between CAE, Explicit and Implicit methods, it is concluded that total internal energy between these three methods do not show significant differences (Figure 54).

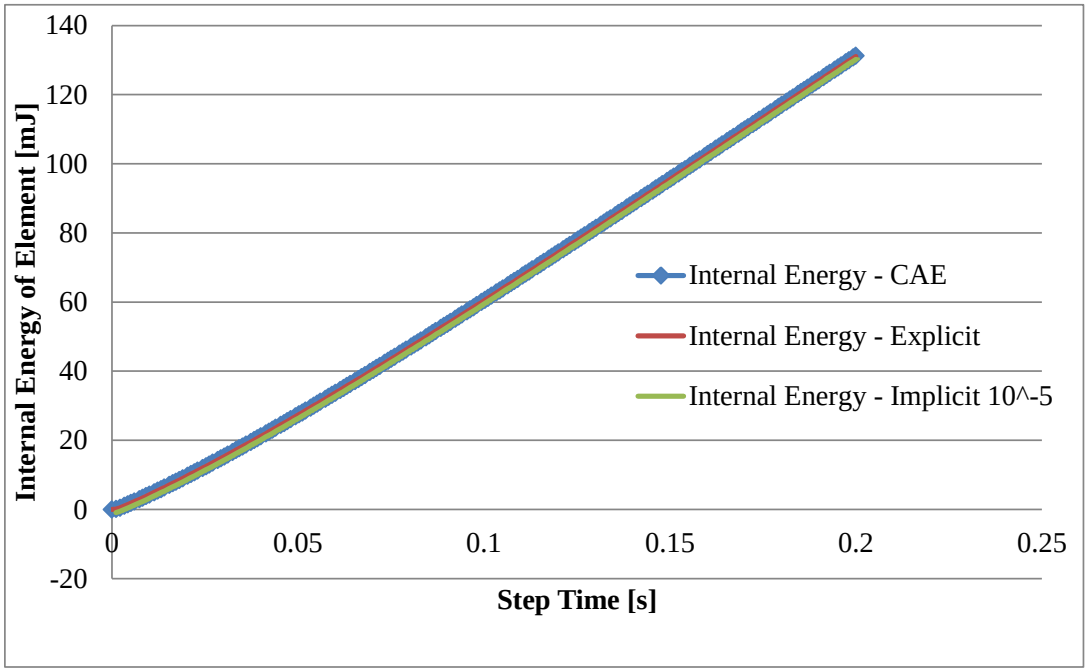

Figure 54: Comparison of internal energies for different methods.

In conclusion, based on one element, the CPU time, field output and history output are compared. It is observed that the CPU time cost increased when convergence criterion decreased with implicit method. The explicit method consumes same CPU time as the optimized implicit method (convergence is 10^{-5}), and the von Mises stress and internal energy are constant with CAE results. Since the machining process is a short time with extremely plastic deformation process, the convergence is a potential issue for implicit method. Also, the CPU time between these two methods have no obvious difference. In conclusion, the explicit scheme is applied for the stress update subroutine during the developing of the machining simulation.

Validation of FEA Approach for a Known Material - Inconel 718

From the one element stress evaluation, there is still 0.25% error between the results for the CAE and the explicit scheme. Orthogonal cutting process is a tremendous elements deformation process, thus validation between CAE and subroutine (Explicit) on orthogonal cutting simulation is necessary. The setup of FEA simulation is shown in Figure 55. The bottom of the workpiece is restricted for all six degrees of freedom and a reference point is attached to the tool. The cutting speed is applied to this reference point and the reaction cutting force is extracted from this point. Element delete is applied to fulfill the separation between chip and workpiece.

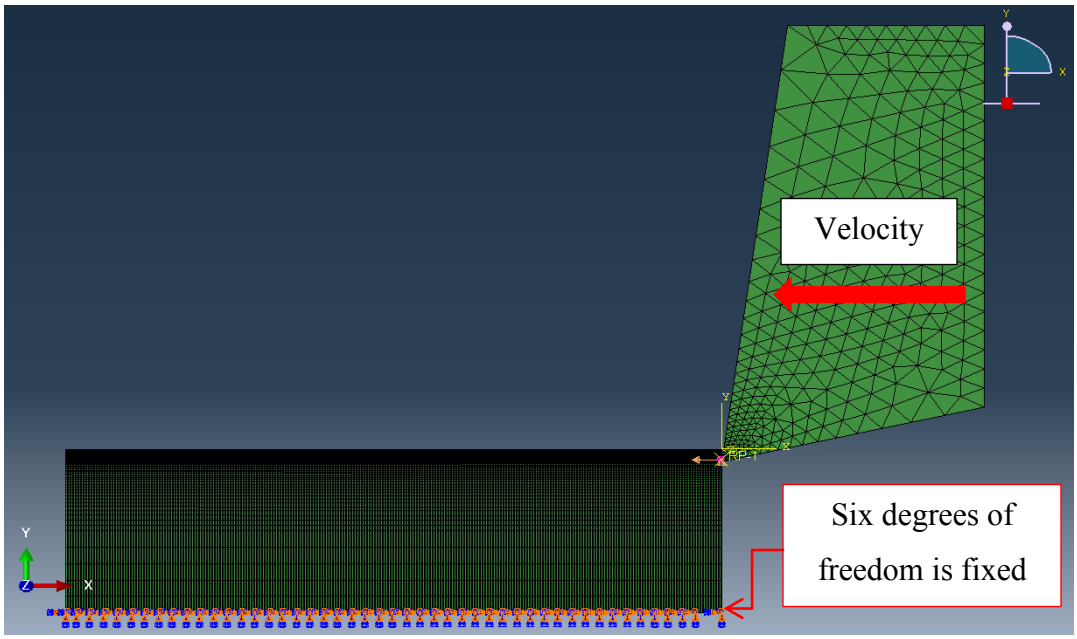

Figure 55: Set up of orthogonal cutting in FE simulation.

Since Johnson-Cook model for Inconel 718 has already been developed and validated in previous research, this model is adopted in this section to compare explicit subroutine and CAE result [57]. If the results of orthogonal cutting of Inconel 718, determined by the explicit subroutine, are similar to that of CAE; then the modified Johnson-Cook constitutive model of GTD111 is applied in finite element analysis with a high confidence.

ABAQUS/Explicit solver with CAE on Inconel 718

In this section, the orthogonal cutting simulations is performed by ABAQUS/CAE which is embedded with Johnson-Cook model (equation (4.46)).

$$\sigma = \left(A + B\varepsilon^{n}\right)\left(1 + C\ln\frac{\dot{\varepsilon}}{\dot{\varepsilon}_0}\right)\left[1 - \left(\frac{T - T_r}{T_m - T_r}\right)^{m}\right]. \tag{4.46}$$

The workpiece material is Inconel 718 and Johnson-Cook parameters are selected from literature, which shown in Table 11.

Table 11 Parameters of Johnson-Cook model for Inconel 718. [53]

Variables	$\dot{\varepsilon}_r$ $[s^{-1}]$	A [MPa]	B [MPa]	C	m	n
Value	1	450	1700	0.017	1.3	0.65

Finite element simulations are developed to study the mechanics of machining, and to estimate the amount of plastic deformation induced subsurface damage in the

workpiece. ABAQUS software is used to simulate the same process conditions as in the experiments. The finite element modeling is executed as follows:

- Inconel 718 Johnson-Cook constitutive model is applied in ABAQUS/CAE. The other material properties are shown in Table 2.
- Depth of cut is 0.1 mm and surface speed is 20m/min.
- The material is assumed isotropic.
- Workpiece size is 1.5mm high and 5 mm long with 2D dimension.
- The elements of the workpiece and the tool model are four-node bilinear displacement and temperature quadrilateral elements (CPE4RT) and a plane strain assumption for the deformations in orthogonal cutting. CPE4RT allows for thermal mechanical coupling processing, especially for machining. The workpiece had 60120 elements. Bias mesh is applied to finer the mesh size around the radius of tool. The minimum size is 0.001mm.
- The cutting tool is assumed as analytical rigid body.
- The thermal expansion and conduction are taken into consideration.
- Since cutting process includes large deformation, Arbitrary Lagrangian-Eulerian meshing (ALE) is applied in the simulations. Also, relax stiffness method is applied to control the hourglassing and avoid extreme distortion of the elements.
- The friction coefficient is set as 0.3 between all the interfaces between tool and workpiece.
- No vibrations occur between workpiece and cutting tool.

- To fulfill the chip separation from workpiece, element deletion is applied, as shown in Figure 56. A state variable is defined to indicate the deletion of element with 0 and 1 value.

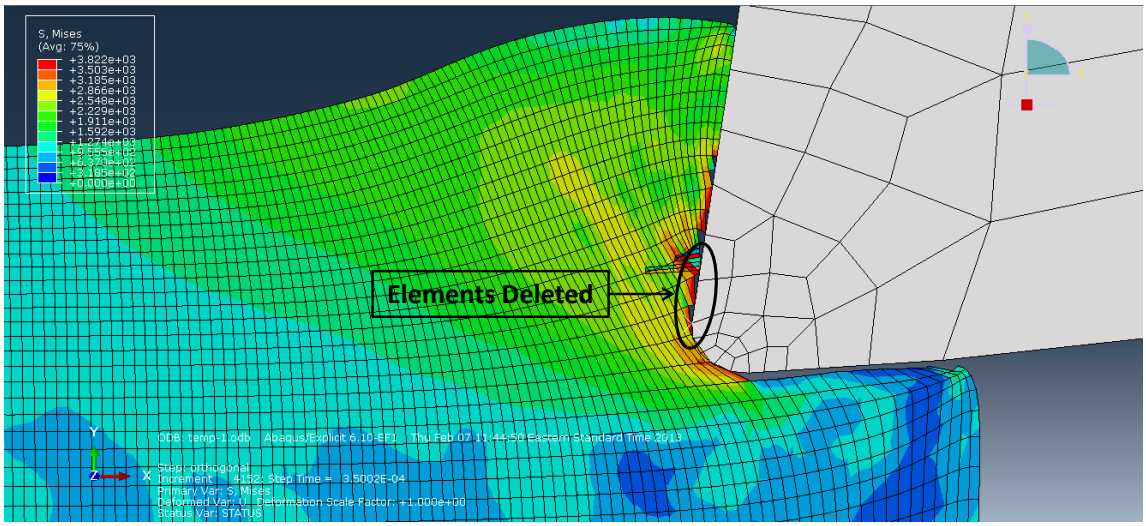

Figure 56: ABAQUS/Explicit: Deletion of Excessive Distorted Element.

- Failure criterion is defined by comparing the equivalent plastic strain to a failure value. Elements deletion is defined when the damage parameter ω exceeds 1. The damage parameter ω is defined by the equation:

$$\omega = \frac{\bar{\varepsilon}_0^{pl} + \sum \Delta \bar{\varepsilon}^{pl}}{\bar{\varepsilon}_f^{pl}}, \tag{4.47}$$

where $\bar{\varepsilon}_0^{pl}$ is the initial equivalent plastic strain, $\Delta \bar{\varepsilon}^{pl}$ is an increment of the equivalent plastic strain, and $\bar{\varepsilon}_f^{pl}$ is the strain at fracture point.

The CAE results of von Mises stress are shown in Figure 57. Depth of subsurface damage are measured to compare with subroutine results.

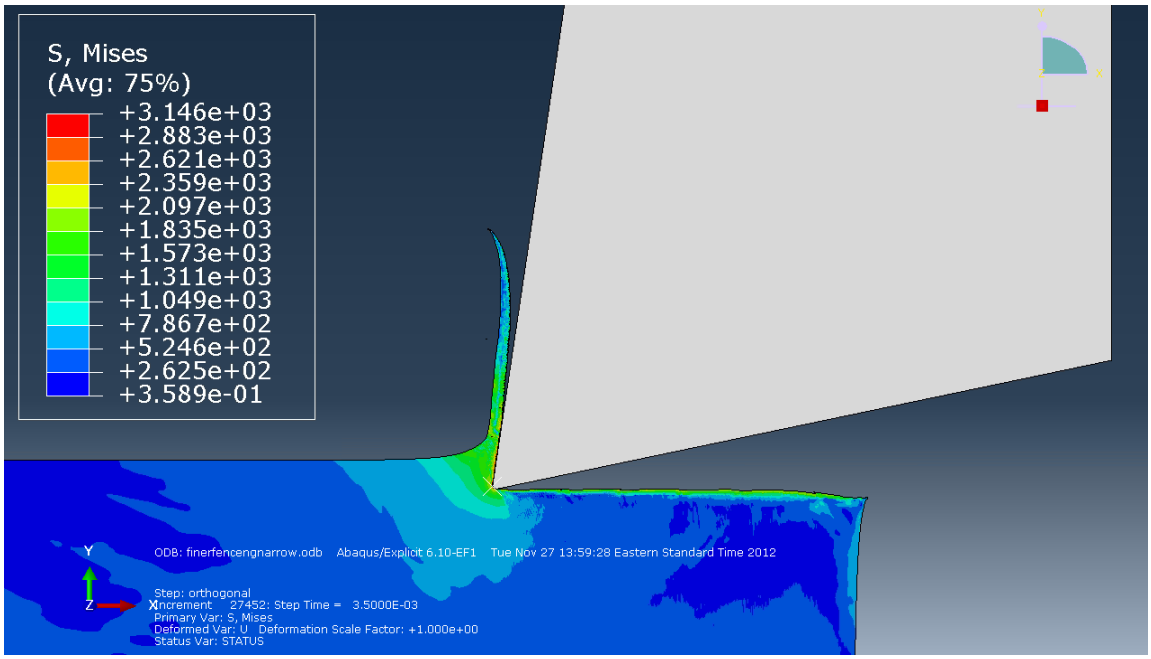

Figure 57: von Mises contours from ABAQUS/CAE; Stresses in MPa.

ABAQUS/Explicit solver with explicit subroutine on Inconel 718

Since ABAQUS/Explicit solver has a strong capability on non-linear analysis, subroutine (explicit) is coded with FORTRAN to depict Johnson-Cook constitutive model. Subroutine code is showed in the Appendix A. The FEA setup for explicit stress updated subroutine shares the same code with CAE method, except the material property section. The von Mises contour from explicit subroutine method is shown in Figure 58.

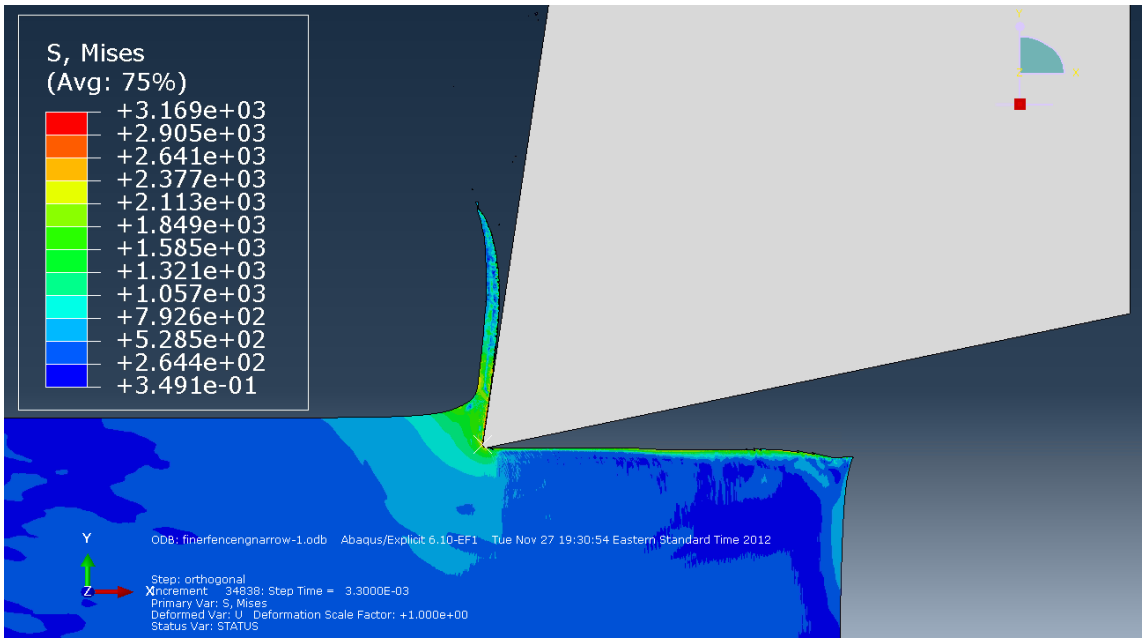

Figure 58 : von Mises contour results from ABAQUS/Explicit – explicit subroutine; Stresses in MPa.

A comparison between the results from CAE and subroutine is performed and the results are summarized in Table 12. Residual stress and PEEQ are presented in this table. PEEQ is the equivalent plastic strain, which is a scalar measure of all the components of plastic strain remained in the machining affected layer. In order to compare the CAE and subroutine results, a threshold stress of 550MPa is selected and used to determine the depth of machining affected zone. In conclusion, the estimated plastic equivalent strains and residual stresses show an agreement of 97.6% and 95.0%, respectively, between CAE and subroutine. This high agreement indicates that explicit subroutine with basic Johnson-Cook model works properly on orthogonal cutting simulation. Next step is

applying the novel constitutive model of GTD111 into this explicit subroutine and compared with experimental results.

Table 12 PEEQ and residual stress comparison between CAE and explicit subroutine.

		Depth of MAZ [μm]
CAE	PEEQ	121
	Residual Stress	38
explicit subroutine	PEEQ	124
	Residual Stress	40

NOTE: The threshold of residual stress is selected as 550MPa.

FEM Simulation Setup and Results for GTD111

In this section, the validated subroutine and modified constitutive model is applied in orthogonal cutting simulations based on ABAUQS/Explicit solver. Similar to the setup for Inconel 718, workpiece is restricted for all six degrees of freedom on the bottom and a reference point is attached to the tool. The cutting speed is applied to this reference point and the reaction cutting force is extracted from the point. Element delete is applied to fulfill the separation between chip and workpiece. The finite element modeling is executed as follows:

- With the verified explicit subroutine, the novel constitutive model derived in Chapter 3 is used. The material model is shown in equation (4.48). Due to the limitations of

FEA, the softening phenomenon ($\frac{d\sigma}{d\varepsilon} < 0$) can not be taken into consideration with continuum plastic material model.

$$\sigma = \begin{cases} f_{A(\varepsilon,T)} \cdot \left(1 + C \ln \frac{\dot{\varepsilon}}{\dot{\varepsilon}_r}\right) \cdot \left(1 - e^h \left(\frac{T - T_r}{1523 - T_r}\right)^m\right), & \mathrm{T}_r \le \mathrm{T} < \mathrm{T}_l \\ f_{A(\varepsilon,T)} \cdot \left(1 + C \ln \frac{\dot{\varepsilon}}{\dot{\varepsilon}_r}\right) \cdot \left(q_1 \left(T - T_p\right)^2 + q_2\right), & \mathrm{T}_l \le \mathrm{T} \le \mathrm{T}_m \end{cases} , \quad (4.48)$$

- The material is assumed isotropic. The material properties are defined in Table 2,
- and Table 6.
- Workpiece size is 1mm in height and 5 mm in length.
- The elements of workpiece and the tool model are four-node bilinear displacement and temperature quadrilateral elements (CPE4RT), and a plane strain assumption for the deformations in orthogonal cutting. The workpiece had 35751 elements. Bias mesh is applied to finer the mesh size around the radius of tool. The minimum size is 0.001mm.
- The cutting tool is assumed as analytical rigid body.
- The thermal expansion and conduction are taken into consideration.
- Since cutting process includes large deformation, Arbitrary Lagrangian-Eulerian meshing (ALE) is applied in the simulations. Also, relax stiffness method is applied to control the hourglassing and avoid extreme distortion of the elements.
- The cutting tools are defined as the rigid body and the properties are defined in
- .

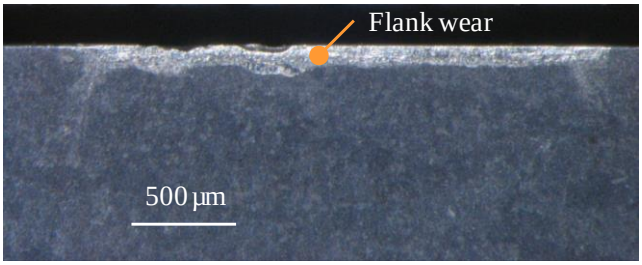

Figure 59: Flank wear from orthogonal cutting.

- Also, flank wears are measured from orthogonal cutting experiment, which is shown in Figure 59. Tool wear in each simulation are defined according to the measurements from experiments. In the simulations, the flank wear is defined by modifying the tool radius and release face of the insert, as shown in Figure 60. This modification induces lower depth of cut and larger contact area.

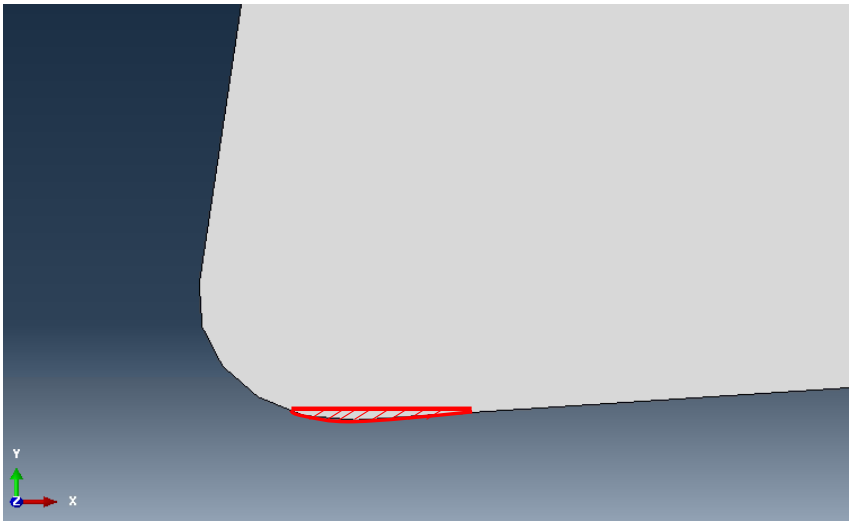

Figure 60: Tool wear definition.

- The contact between tool and workpiece is defined as penalty contact. The friction coefficient is set as 0.3 between all the interfaces. The coefficient of friction is determined by matching FEA simulations to the experimental data. Table 13 presents the results of the FEA analysis for coefficients of friction between 0.1 and 0.4. As the smallest deviation from the experimental number is generated by the FEA using a coefficient of friction value of 0.3, that is the value used for all simulations in this research. To provide a better understanding of the sensitivity of the model to variations in the coefficient of friction, the data from Table 13 are plotted in Figure 61. As can be seen from Figure 61, small deviations from the nominal value of the coefficient of friction result in fairly good match to the experimental data. However, larger variations of the coefficient of friction do yield unacceptable deviations between the model and the experimental data.

Table 13 Friction coefficients sweep comparison with speed: 10m/min, Doc: 0.05mm.

Friction Coefficient μ	Averaged Resultant Cutting Force from FEA Simulation [N]	Averaged Resultant Cutting Force from Experiment [N]
0.1	593	748
0.15	644	
0.2	683	

0.25	723	
0.3	751	
0.35	776	
0.4	797	

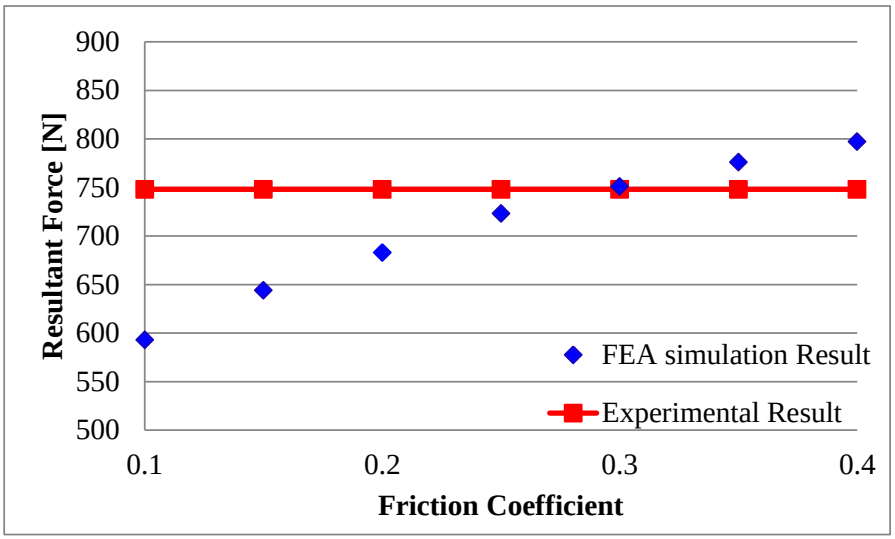

Figure 61: Friction coefficients sweep comparison with speed: 10m/min, Doc: 0.05mm.

- The code to define Coulomb friction contact is shown as:

```
*Surface Interaction, name=IntProp-1
*Friction
 0.3,
** Interaction: Int-1
```

*Contact Pair, interaction=IntProp-1, mechanical constraint=PENALTY, cpset=Int-1 (All faces from workpiece, outside face of tool)

- The cutting simulation is an extremely large plastic deformation process, during which the face of the tool makes contact with all of the four faces of the elements in workpiece, as shown in Figure 62. Face one (F1) to face four (F4) in each element is defined with the contact property mentioned above, thus, the penetrating phenomenon does not appear during orthogonal cutting.

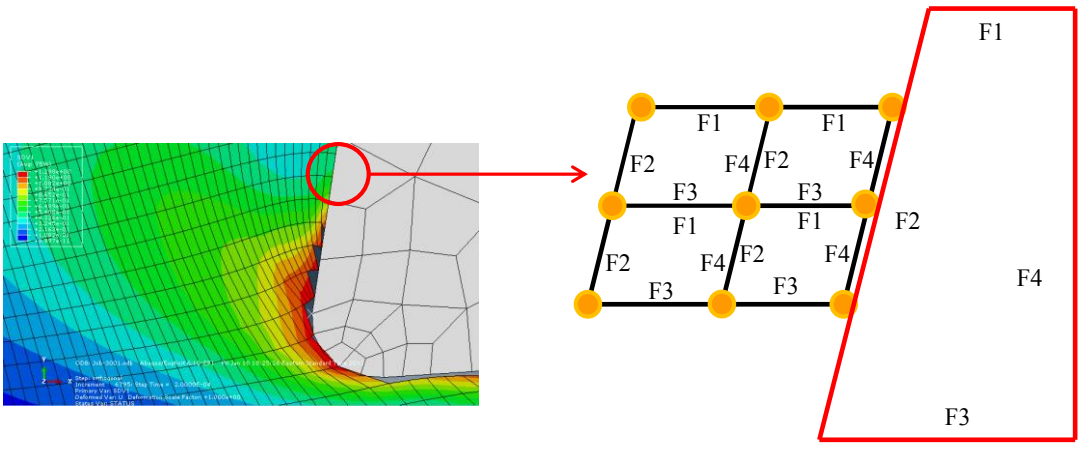

Figure 62: Faces of elements contact between tool and workpiece.

- No vibrations occur between workpiece and cutting tool.
- To fulfill the chip separation from workpiece, failure criteria and element deletion are applied in orthogonal cutting simulation, which is shown in Figure 56. Failure criterion is defined by comparing the equivalent plastic strain to a failure value. Elements deletion is defined when the damage parameter ω exceeds 1. The damage parameter ω is defined as the equation:

$$\omega = \frac{\bar{\varepsilon}_0^{pl} + \sum \Delta \bar{\varepsilon}^{pl}}{\bar{\varepsilon}_f^{pl}} \ , \tag{4.49}$$

where $\bar{\varepsilon}_0^{pl}$ is the initial equivalent plastic strain, $\Delta \bar{\varepsilon}^{pl}$ is an increment of the equivalent plastic strain, and $\bar{\varepsilon}_f^{pl}$ is the strain at fracture point. A state variable is defined to indicate the deletion of element with 0 and 1 value.

With all the setup mentioned above, FEA simulation results are shown from Figure 63 to Figure 67. As these figures shown, the von Mises contour is observed. The chips separated from workpiece successfully. The subsurface damage information are derived and compared with experimental results. The equivalent plastic strain and temperature contour are summarized in Appendix C.

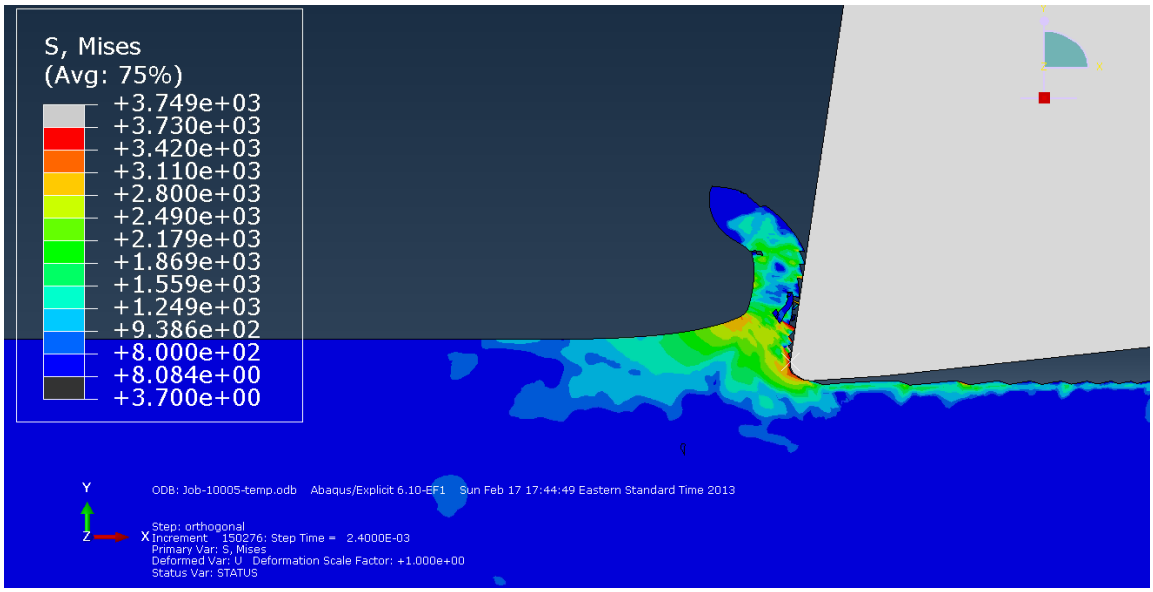

Figure 63: Stress distribution for Speed: 10 m/min, DoC: 0.05 mm; Stress in MPa.

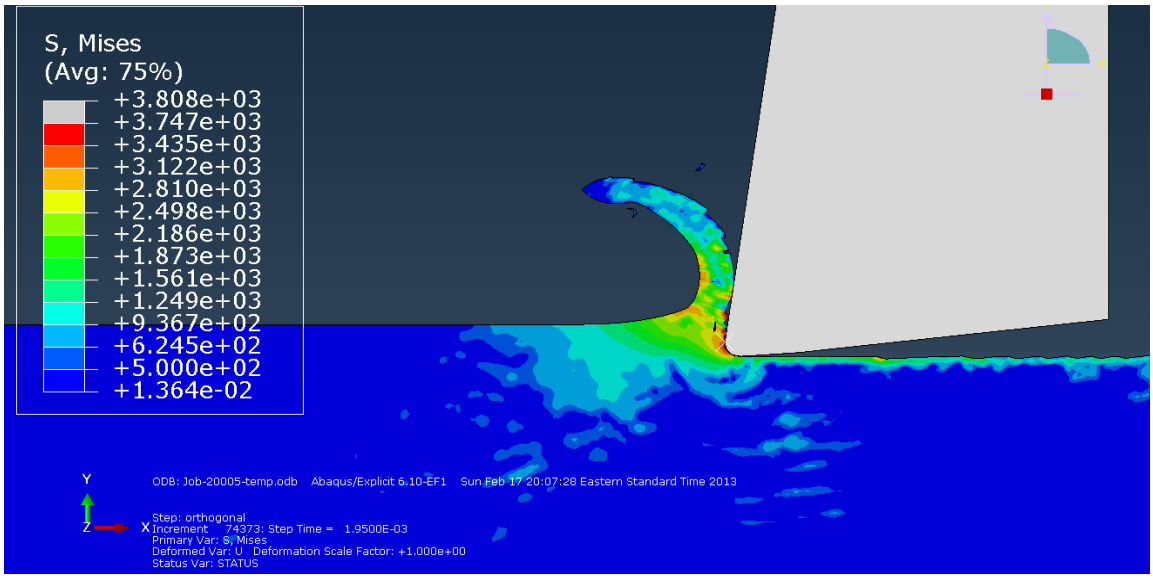

Figure 64: Stress distribution for Speed: 20 m/min, DoC: 0.05 mm; Stress in MPa.

Figure 65: Stress distribution for Speed: 30 m/min, DoC: 0.05 mm; Stress in MPa.

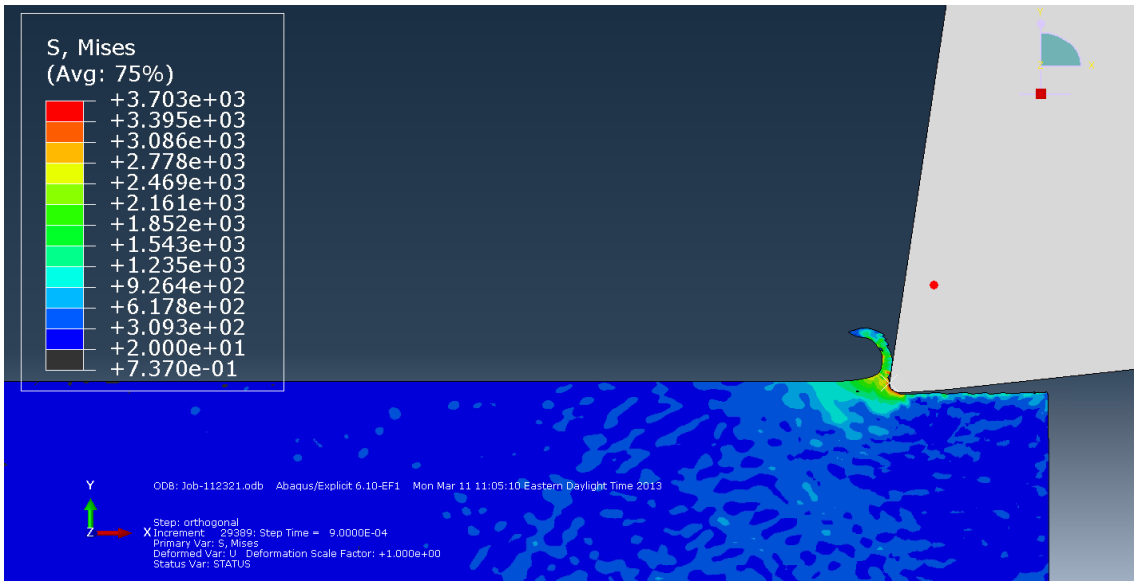

Figure 66: Stress distribution for Speed: 20 m/min, DoC: 0.025 mm; Stress in MPa.

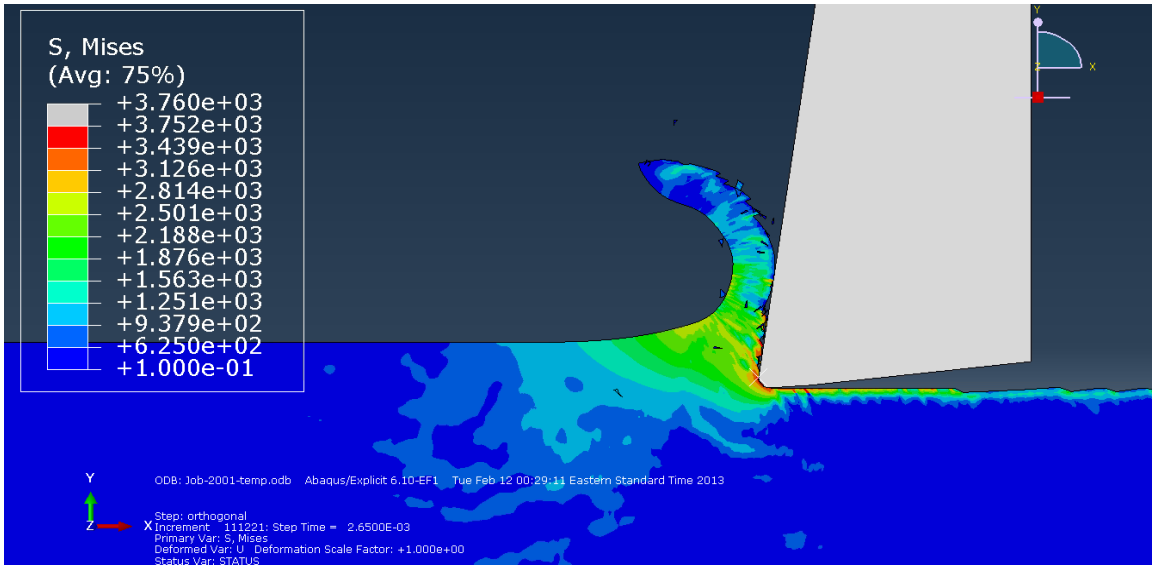

Figure 67: Stress distribution for Speed: 20 m/min, DoC: 0.1 mm; Stress in MPa.

In summary, two schemes of integration method (explicit and implicit) are explained. Based on the two schemes, two subroutines are developed for stress updating during each time increment. In order to verify the accuracy of subroutines, the CAE are developed as a contrast. The CPU time and von Mises outputs are compared and explicit scheme is chosen for the further investigation. After validate the explicit subroutine, modified Johnson-Cook model is adopted to depict the material plastics behavior. Based on the ABAUQS/Explicit solver, the finite element analysis on orthogonal cutting has been developed with material GTD111. Meanwhile, the flank wear from experiments is defined in FEA simulations. The following chapter presents experimental validation of the simulations from cutting force and subsurface damage aspects.

CHAPTER FIVE

EXPERIMENTAL VALIDATION OF THE PROPOSED MODEL

A modified material's constitutive model is developed in Chapter 3 using tensile tests performed at elevated temperatures, and by modifying the Johnson-Cook model. The new model is integrated in a user defined subroutine for finite element analysis. Orthogonal cutting simulations are carried out, and stresses, strains and forces are determined. This chapter presents the validation of the finite element model via experiments. The validation is required to ensure that the FEA orthogonal cutting model can be further applied to derive subsurface data for statistical analysis and modeling of subsurface damage. The experimental investigations are performed using the same cutting parameters used in the finite element analysis simulations. The resultant reaction force, temperature of chip/tool and depth of subsurface damage are investigated.

Experimental Setup

The experimental setup is shown in Figure 68. The workpiece is mounted in the spindle of an Okuma 3-axis milling center, while the orthogonal cutting tool is mounted on the Kiesler piezoelectric dynamometer. Kiesler piezoelectric dynamometer is used to record the cutting forces during orthogonal cutting process.

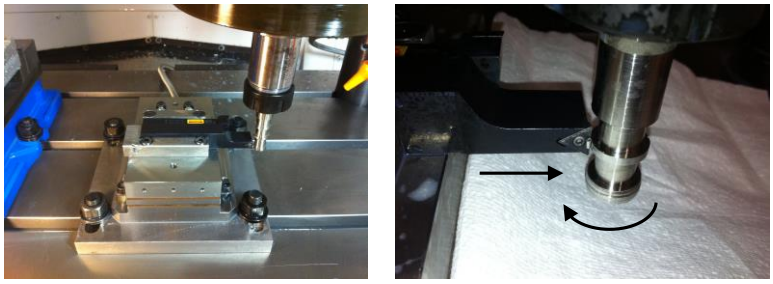

(a) (b)

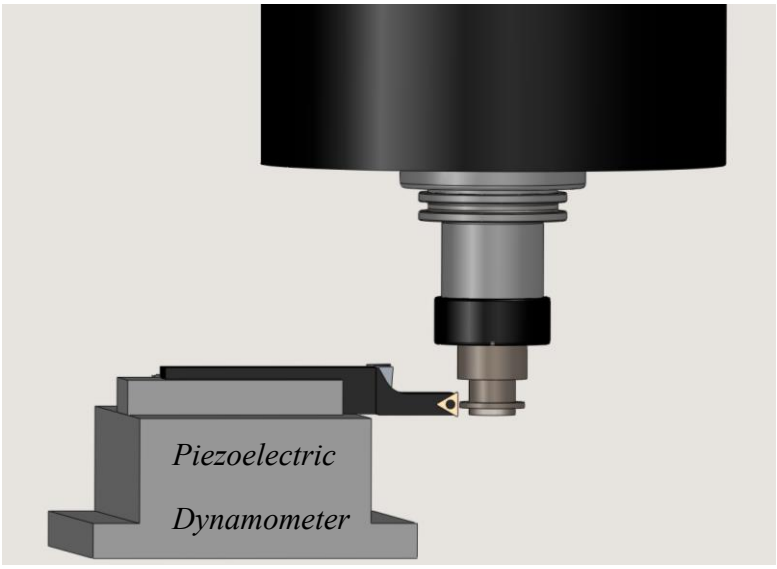

(c)

Figure 68: Experimental setup and design of the tests.

As shown in Figure 68, orthogonal tests are performed on a cylindrical workpiece. Groves are made to create the testing zones with a width of 2.5mm, which is 25 times larger than the deepest depth of cut in the tests performed. So, this makes the orthogonal cutting process to be a plane strain situation, as it is performed in the FEA simulation. The workpiece material is a nickel-based cast superalloy (GTD111) currently used for

fabricating gas turbine blades; the carbide tool is TCMT 11 03 04-MM 1105 with PVD coated insert (TiAlN). The test matrix is given in Table 14.

Table 14 Design of orthogonal cutting tests.

Effect investigated	Cutting speed [m/min]	Depth of cut [mm]
Cutting speed	10	0.05
	20	
	30	
	40	
Depth of cut	20	0.025
		0.05
		0.1

The movement of the tool (feed) gives the desired depth of cut. The surface speed is calculated by:

$$v = w \cdot \pi \cdot D_c , \tag{5.1}$$

where v is surface speed, w is spindle speed and D_c is the diameter of the specimen.

The triangular insert has 12° rake angle. Each test is quick-stopped after five revolutions of the workpiece. During the first revolution, the tool engaged gradually the depth of cut increases to the desired value, and is kept constant for the rest of the test. No coolant is employed, and a new cutting edge is used for each test. Each test is repeated 3-4 times.

The tangential force and radial force are explained in Figure 69. Tangential force is consistent with friction force and horizontal component force from rake face. The radial force is consistent with normal pressure from flank face and vertical component force form rake face. Resultant force is calculated as:

$$F_{res} = \sqrt{\left(F_{Radial}\right)^2 + \left(F_{Tangential}\right)^2}, \tag{5.2}$$

Figure 70 plots the two components of the resultant force: radial force and tangential force. As this graph shows, the same continuous increase of both radial and tangential forces is observed and it attributed to the severe tool wear. The radial force reaches a relative stable stage earlier than the tangential force. After 140mm cutting distance, due to the increased friction force, the tangential force exceeds the radial force. This means the tool wear induced significant friction force. From this point of view, the tool wear must be considered in FEA simulation for γ'-strengthened nickel-based superalloy.

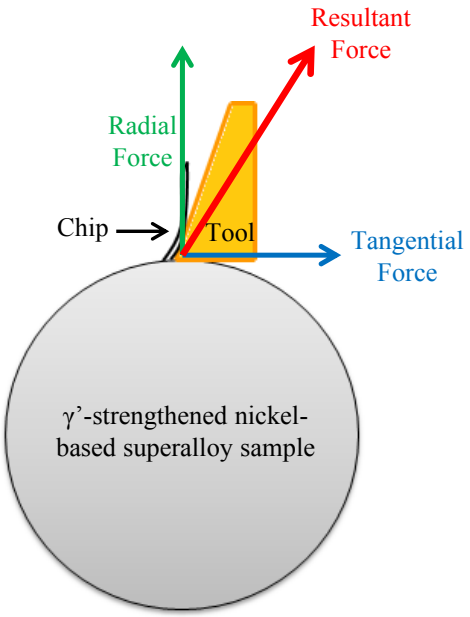

Figure 69: Force components explanation.

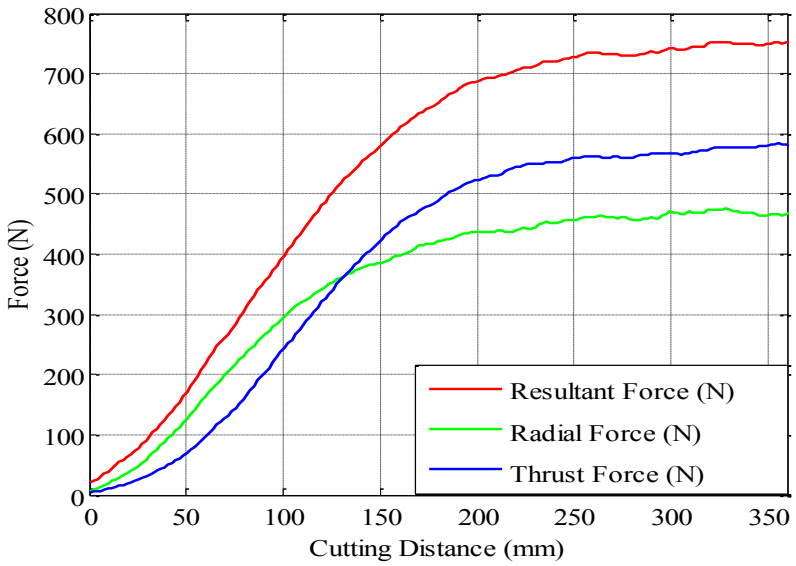

Figure 70: Two components of the cutting force for v=10m/min, DoC=0.05mm.

In order to compare force results between different tests, the processed force are compared. Figure 71 shows the average force versus cutting distance for test 1 (v=10m/min, DoC=0.050mm). The blue line is the raw data, which is directly exported from orthogonal tests with sample frequency of 6000Hz by Dynoware software. The red line represents the data processed with low-pass Butterworth filter and a moving average window. If for the 1st revolution this is expected due to the progressive increase in the depth of cut, the force increase from the 2nd to 5th revolutions indicates severe tool wear due to harsh nature of cutting of nickel-based superalloys. After the first pass, the depth of cutting remains at a constant level, which is shown with green curve in Figure 71. Thus, the force increase after 70 mm is due to the rapid tool wear. After 200mm the tool wear maintains relatively constant. This graph shows a typical tool wear stage. Also it is concluded tool wear during the 5th revolution remains fairly constant.

Since severe tool wear is observed at the end of each experiment, in FEA simulation, the tool wear is defined correspondingly. Typical flank wear is shown in Figure 72. The measurements of Vb are summarized in Table 15.

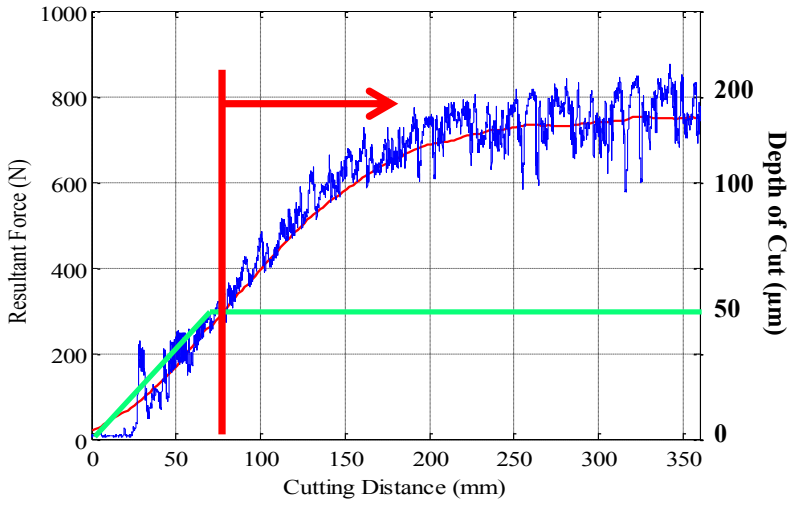

Figure 71: Cutting forces for v=10m/min, DoC=0.05mm.

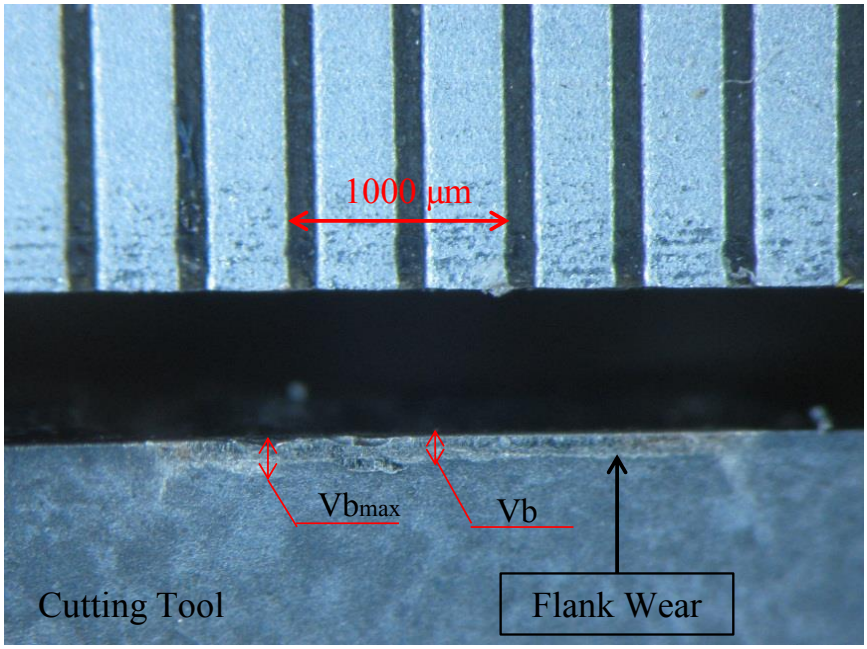

Figure 72: Tool wear for v=10m/min, DoC=0.05mm.

Table 15 Desgin of Experiments with Tool Wear Measurements.

Effect investigated	Cutting speed [m/min]	Depth of cut [mm]	Tool Wear [μm]
Cutting speed	10	0.05	126
	20		104
	30		82
	40		Catastrophic Failure
Depth of cut	20	0.025	61
		0.05	104
		0.1	118

Cutting Force Comparison

In orthogonal cutting simulation, the reaction cutting force is given by the reaction force from the elastic and plastic deformation as well as friction force. In the simulations, oscillating forces are observed in the resultant force due to the deletion of elements, thus a direct comparison of the force profile is not possible. Another aspect is that the experiments show an increasing trend attributed to the tool wear, which cannot be reproduced yet in the simulations. In order to compare the cutting force between FEA simulation and experiments, the average maximum cutting force from a relatively constant stage are selected for experimental results. As previously mentioned, on the 5th revolution of the orthogonal cutting the tool wear and the force keep at a stable level. These are the results to be compared to the FEA simulation performed for a similar tool wear (Figure 73).

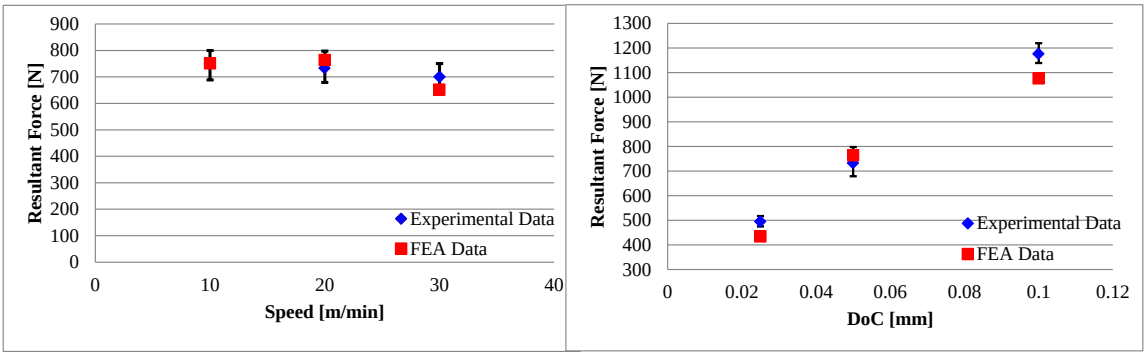

(a) (b)

Figure 73: Resultant force comparison: (a) Resultant cutting force vs. surface speed, (b) Resultant cutting force vs. Depth of cut.

It is concluded that the maximum error between experimental resultant force and FEA simulation force is ~15%. After the cutting force being validated, the depth of subsurface damage from FEA simulation is compared with the experimental results in next chapter.

CHAPTER SIX

ESTIMATION OF SUBSURFACE DAMAGE AND VERIFICATION

In this chapter, the von Mises stresses are output from the nodes along the depth of machining affected zone. Then, threshold stress values (von Mises stress and equivalent plastic strain) are determined by comparing to the experimental results. Also, the temperature fields in subsurface damage are investigated from FEA simulation.

Depth of subsurface damage measurements from experimental samples

Thermal recrystallization is a grain growth and recovery process, with releasing storage energy generated from plastic deformation. The driving force for thermal recrystallization is determined from the difference in storage energy between recrystallized and deformed state. In 2005, P.R. Rios *et al.* concluded that driving force can be written as equation (6.1): [75]

$$F_N = G \cdot b^2 \cdot (\rho - \rho_0), \tag{6.1}$$

where F_N is driving force, G is shear modulus, b is the modulus of the Burgers vector to depict the magnitude and direction of the distortion of dislocation in crystal lattice, ρ is density of dislocation in deformed state and ρ_0 is density of dislocation in undeformed state.

The annealing temperature controls the nucleation and grain growth rate. Larger plastic deformation induces higher driving force and requires a lower recrystallization temperature. The resulting recrystallized grain size is highly sensitive to the applied strain

before thermal recrystallization. The machined surface has a severe plastic deformation on the top portion of subsurface damage layer that decreases to zero plastic deformation at the bottom portion of subsurface layer. Since the recrystallization process is a recovering process, crystal structures are reorganized and the defects are eliminated. According to equation(6.1), the density of dislocation in the recrystallized state is reduced, generating a driving force.

With the standard annealing process for nickel-based superalloy (standard temperature, heating and cooling time), the top deformed grains with relatively higher driving energies start to nucleate and grow. However, with decreasing $\Delta\rho$, the driving force decreases to the same level as retarding force and grain boundary growth is stopped. Thus, in this research, the depth of subsurface damage is defined as the depth of ultimate recrystallized grain boundary.

The machined samples are prepared for SEM and Optical microscope analysis. Figure 74(a) and (b) shows the schematic illustration of the orthogonal cutting process and where the sample is cut via wire EDM for microstructure analyses. Figure 74(c) shows the process to prepare the sample from orthogonal cutting for optical measurements. As mentioned in Chapter 1, thermal recrystallization process is conducted in order to obtain more objective measurements of the subsurface damage. The thermal recrystallization process is completed by GE Power and Water through a standard annealing process. This annealing process makes the original grain boundaries disappear during a certain temperature range within certain time. Meanwhile, the residual stress is relieved during this heat treatment process. Then, associated with the decreasing

temperature, nucleation starts and the grain rapidly grows through grain boundary migration, which leads to a visible boundary between the undeformed structure and the newly recrystallized grains. After the recrystallized samples are mounted in resin and polished, Kalling #2 (Ethyl Alcohol, Hydrochloric Acid and Cupric Chloride) is applied on the surface, the boundary between grains are etched and appeared. A prepared sample is shown in Figure 74(d). The subsurface damage beneath the machined face is investigated from the edge of the disc.

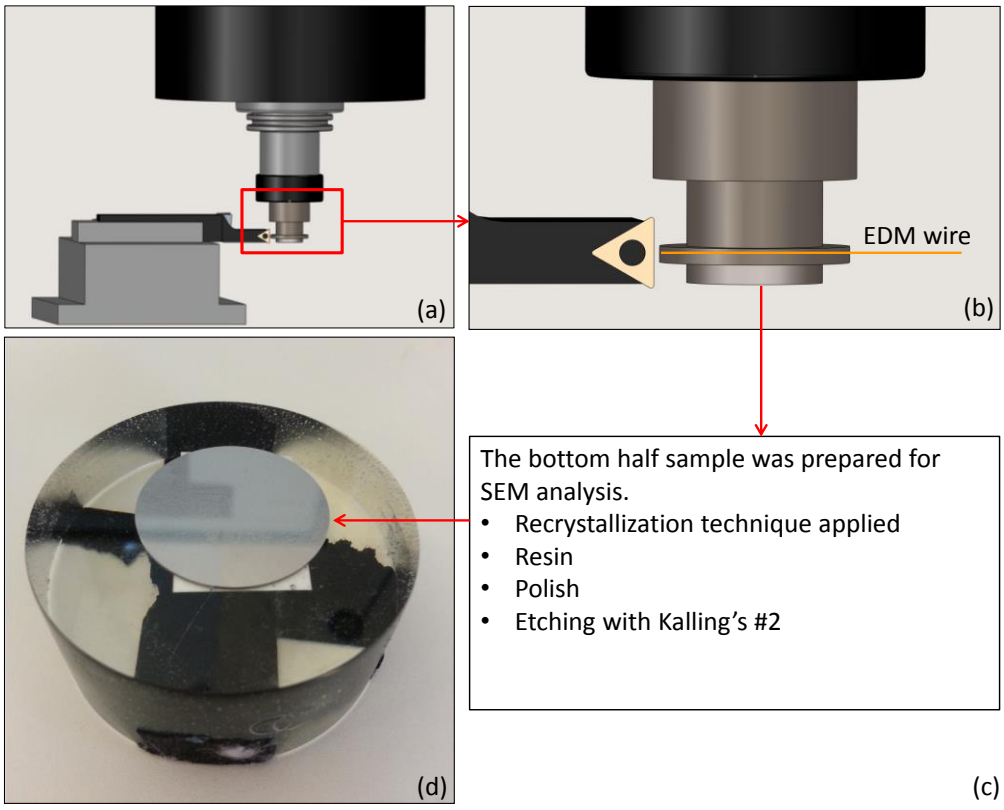

Figure 74: Schematic illustration of the orthogonal cutting process and recrystallized sample for optical analysis.

In Figure 75(a), the SEM image shows the machining induced subsurface damage before recrystallization. The dark particles are γ' phase and the matrix is γ phase; both of the two phases are dragged and elongated along the machining direction. As previously mentioned, from Figure 75(a), the measurement of subsurface damage is subjective. Figure 75(b) shows the optical image of a recrystallized sample where the new grain boundaries is easily observed. The depth of subsurface damage is defined as the maximum distance from the machined surface to the grain boundary.

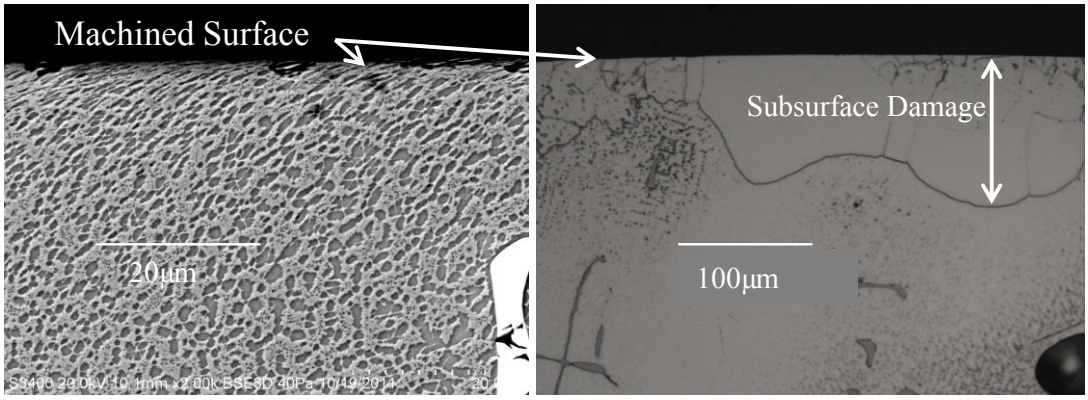

(a) (b)

Figure 75: Subsurface damage comparison between (a) sample before recrystallization and (b) recrystallized sample.

The depth of subsurface damage measurements for the recrystallized samples is summarized in Table 16. From each test, five optical measurements are taken from five different positions on the machined surface. The maximum depth of subsurface damage

is collected and the average of these five maximum depths is defined as the final depth of subsurface damage.

Table 16 Experimental Result on Recrystallized Samples.

Effect investigated	Cutting speed [m/min]	Depth of cut [mm]	Depth of subsurface damage [μm]
Surface Speed	10	0.05	62.0
	20		61.3
	30		44.3
Depth of Cut	20	0.025	38.0
		0.05	61.3
		0.1	107.0

Threshold stress to determine the depth of subsurface damage in FEA simulation

Von Mises yielding criteria is utilized as the indicator of when material yielding begins. With finite element method, in order to measure boundary of subsurface damage, a threshold stress value is determined. Von Mises stress of the nodes beneath the machined surface are measured and compared to the experimental results. From chapter 4, it is concluded that von Mises stress is written as:

$$\sigma_{VonMises} = \sqrt{\frac{3}{2}\left[\left(\sigma_{11}^{'}\right)^2 + \left(\sigma_{22}^{'}\right)^2 + \left(\sigma_{33}^{'}\right)^2 + 2\cdot\left(\sigma_{12}^{'}\right)^2 + 2\cdot\left(\sigma_{13}^{'}\right)^2 + 2\cdot\left(\sigma_{23}^{'}\right)^2\right]}, \qquad (6.2)$$

where $\boldsymbol{\sigma}_{ij}^{'} = \boldsymbol{\sigma}_{ij} - \bar{\sigma} \cdot \boldsymbol{I}$ named deviatoric stress.

Von Mises stress at $\Delta t + t$ is calculated and output for a series of nodes beneath the machined surface. To determine the threshold stress, the residual stresses are output along the depth of machined affected zone from FEA simulations, which is shown in Figure 76. The depth of subsurface measurement from experiments is utilized as the target, which is summarized in Table 16. Both data from experiment and FEA simulation are plotted as two 3D surfaces. The intersection line between these two surfaces is selected as the threshold value to determine the depth of subsurface damage. Then, according to the determined threshold stress value, the position of the node is obtained. The depth of subsurface damage is calculated by measuring the position of the node.

Figure 77 is an example shows the von Mises stress in subsurface damage layer. The von Mises stresses of the first six nodes from Figure 76, which is beneath the machined surface, are outputted and summarized in Figure 77. After the relax process, the von Mises stress stays in a constant level.

From the FEA simulation, the depth of subsurface damage is investigated. Figure 76 shows the material deformed in the direction of cutting, and it also presents the method of estimating the depth of subsurface damage. The von Mises stress and the equivalent plastic stain are extracted for the red nodes to determine the depth of subsurface.

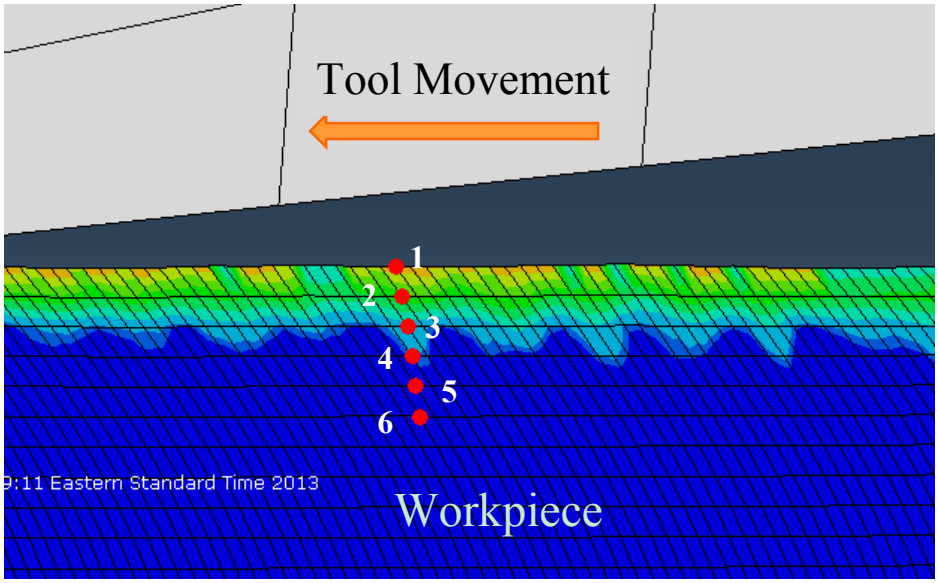

Figure 76: Subsurface measurement from node to node for v=20m/min, DoC=0.1mm.

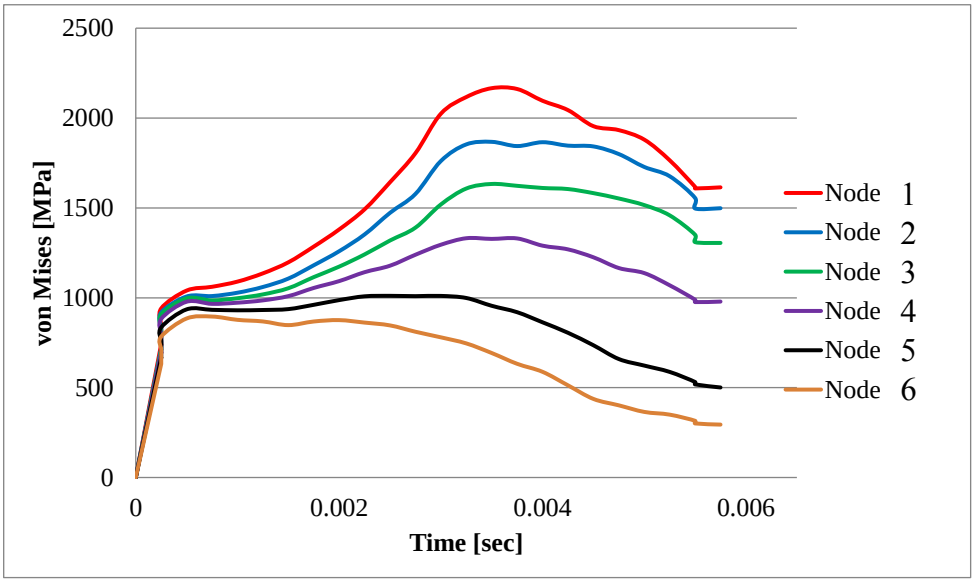

Figure 77: Residual Stress on each node along the Machined Subsurface for v=20m/min, DoC=0.1mm.

In order to determine this threshold stress value, a sweep stress comparison has been performed from 550MPa to 1555MPa, which is shown in Table 17. The position for each stress is calculated from with linear interpolation between two adjacent nodes with known positions. Then, the experimental results are applied as a target to compare with FEA results.

Table 17 Stress Sweep Measurements of Threshold Value to Determine Boundary on Susbsurface Damage.

Surface Speed [m/min]	**Threshold Stress [**MPa**]**	**Depth of Subsurface Damage [**μm**]**
10	550	71.2
	990	64.5
	1350	44.4
	1500	35.4
	1555	19.5
20	550	62.0
	990	56.8
	1350	40.1
	1500	31.1
	1555	16.9
30	550	53.1
	990	45.7
	1350	39.7

	1500	26.9
	1555	16.1

Figure 78 shows an objective method to determine the threshold stress value for the depth of subsurface damage for FEA simulation by comparing to the experimental results. By using the second order function $Depth = f\left(Threshold\ stress, Surface\ Speed\right)$, the scatter data point from experiments and FEA is fitted by regression analysis. As Figure 78 shown, the solid grid surface depicts the data from FEA simulation with the data in Table 17 and the hollow surface indicts the subsurface information from experiments. As this figure shown, the intersection between these two surfaces is between 1000MPa and 1100MPa. So, von Mises value of 1050MPa is determined as the threshold value to justify the depth of subsurface damage in FEA, which are optimized to the recrystallization sample from experiments. The right top image in Figure 78 is the top view of the 3D figures.

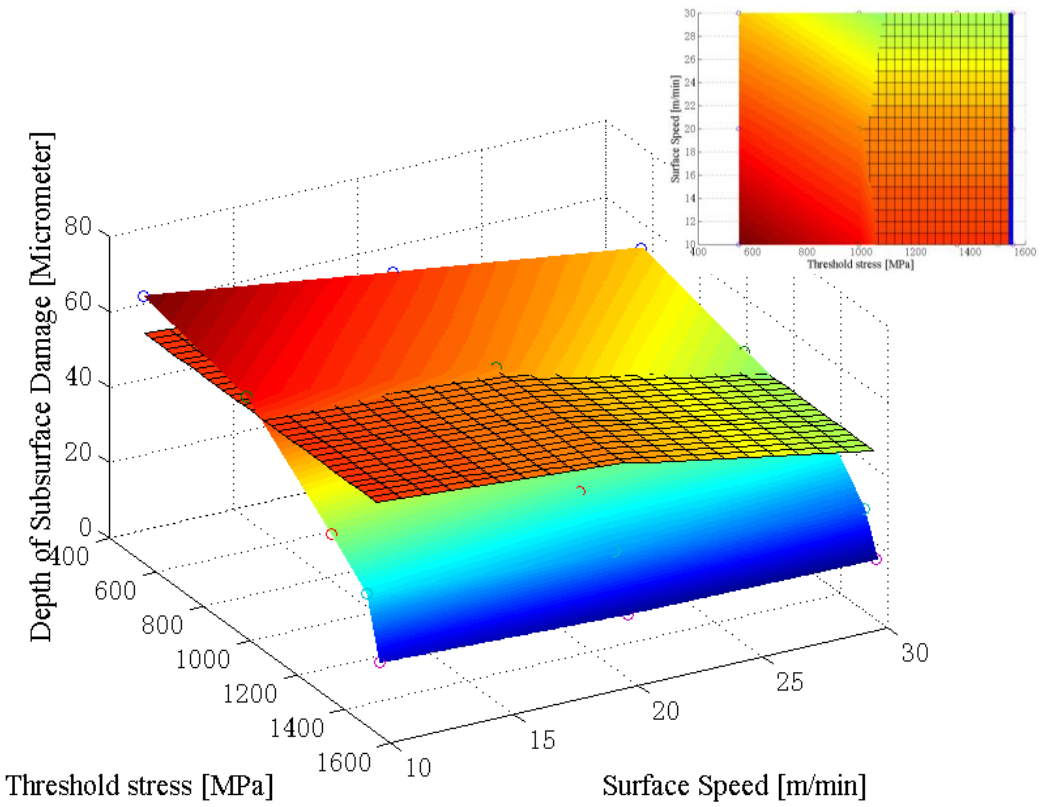

Figure 78: Comparison between Experimental and FEA results used to determine the Threshold stress.

Further observations can be drawn from Figure 78. At the 16 μm depth beneath the machined surface, the residual stresses for three surface speeds are all 1555MPa. In another word, the surface speed is not a significant factor to the depth of subsurface damage at this depth.

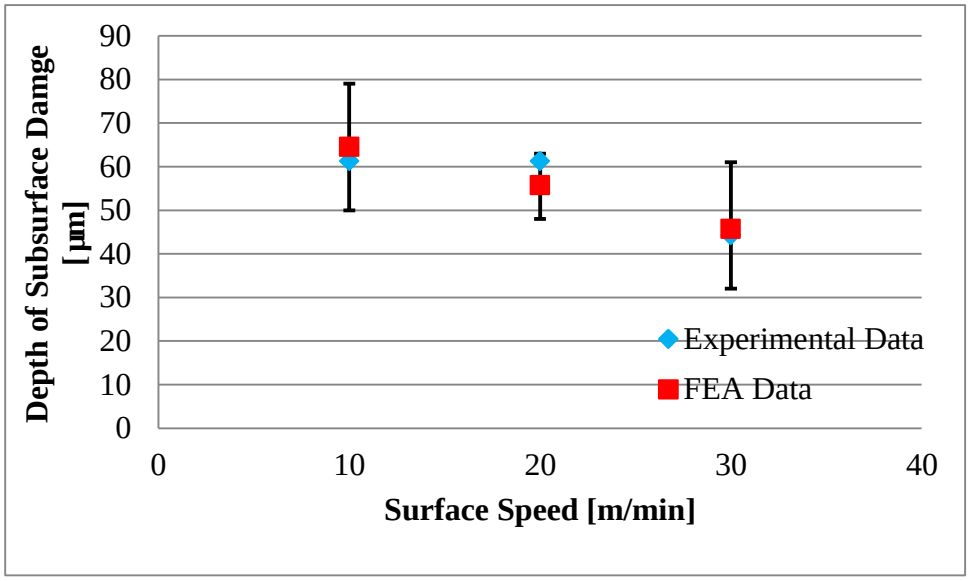

Figure 79: Residual Stress vs Recrystallized Sample with Various Speeds.

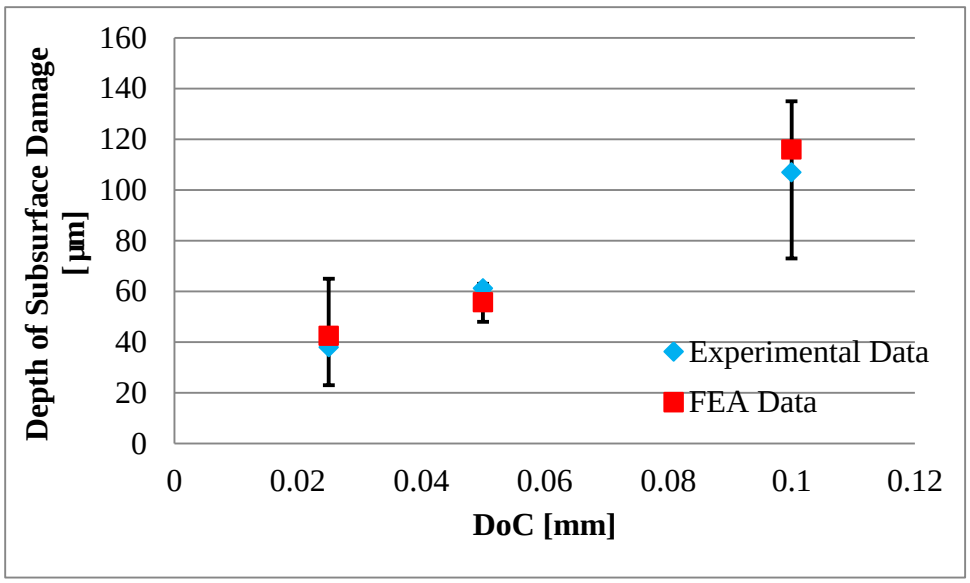

Figure 80: Residual Stress vs Recrystallized Sample with Various DoC.

Then recrystallized samples are measured and the depth of the subsurface damage is compared to the FEA results in Figure 79 and Figure 80. From the Figure 79 and Figure 80, it is concluded that with the experimental determined threshold stress, depth of subsurface damage from FEA simulation matches the recrystallized experimental sample. The agreement is more than 90%. It is also concluded that with same DoC, increasing surface speed induced lower depth of subsurface damage. Meanwhile, with the same surface speed, deeper DoC results in deeper subsurface damage with a linear relationship.

Threshold equivalent plastic strain to determine the depth of subsurface damage in FEA simulation

From FEA simulation, PEEQ (plastic equivalent strain) is generated. As it mentioned in chapter 4, PEEQ is a scalar used to measure the plastic deformation remaining in the workpiece. The value of PEEQ indicates the amount of plastic deformation remained in the workpiece.

Using the same method as determining threshold stress from the previous section, the same steps are applied to determine the PEEQ threshold value of subsurface damage. In order to determine the threshold PEEQ value, the sweep measurements of PEEQ are compared from 0.005 to 0.035, which are shown in Table 18.

Table 18 PEEQ Sweep Measurements of Threshold Value to Determine Boundary on Susbsurface Damage.

Surface Speed [m/min]	**Threshold PEEQ**	**Depth of Subsurface Damage [μm]**
10	0.035	42.3
	0.03	43.4
	0.025	45.6
	0.02	49.8
	0.015	52.1
	0.01	59.1
	0.007	66.2
	0.005	76.4
	0.003	82.1
	0.002	92.4
20	0.035	41.6
	0.03	42.7
	0.025	44.1
	0.02	46.5
	0.015	49.7
	0.01	52.6
	0.007	57.6
	0.005	64.2
	0.003	73.1
	0.002	78.1

30	0.035	27.1
	0.03	28.3
	0.025	31.1
	0.02	35.8
	0.015	41.4
	0.01	44.9
	0.007	49
	0.005	66.1
	0.003	72
	0.002	77.1

As shown in Figure 81, the scatter data point from experiments and FEA are fitted by regression analysis with second order functions. The solid surface shows the result from FEA simulation with the data Table 18 and the hollow surface shows the subsurface information from experiments. The intersection between these two surfaces is between 0.009 and 0.011. It is concluded that an equivalent plastic strain of 0.01 is appropriate determined as the threshold value for estimation of the depth of subsurface damage in FEA. The right top image in Figure 81 is the top view of the 3D figures. In 1991, T. Y. Kim also discovered that a minimum amount of plastic deformation, which is due to the specific annealing process, is the requirement to produce a nucleation of new grains followed by the grain growth during thermal recrystallization process.

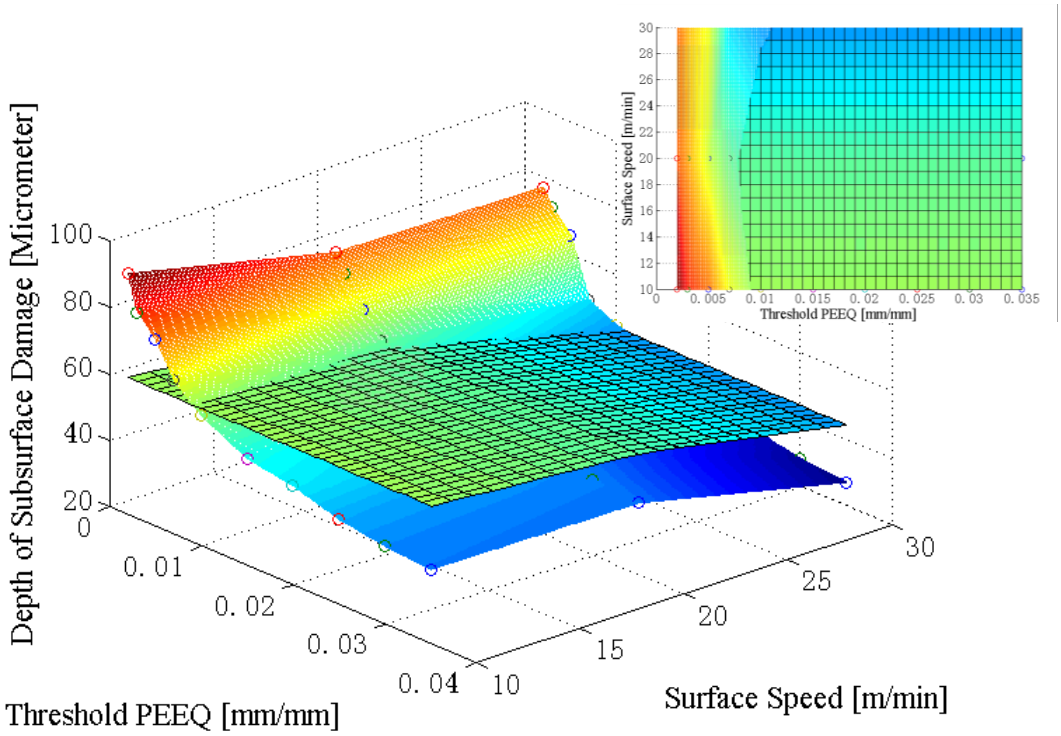

Figure 81: Comparison between Experimental and FEA results used to determine the Threshold PEEQ.

Then recrystallized samples are measured and the depth of the subsurface damage is compared to the FEA results in Figure 82 and Figure 83. From Figure 82 and Figure 83, it is concluded that with the experimental determined threshold PEEQ, depth of subsurface damage from FEA simulation matches the recrystallized experimental sample. However, compared to stress determination method, subsurface damage becomes shallower with PEEQ determination. The agreement is more than 85%. Also, it is concluded that with same DoC, increasing surface speed induced lower depth of subsurface damage. Meanwhile, with the same surface speed, deeper DoC results in deeper subsurface damage with linear relationship.

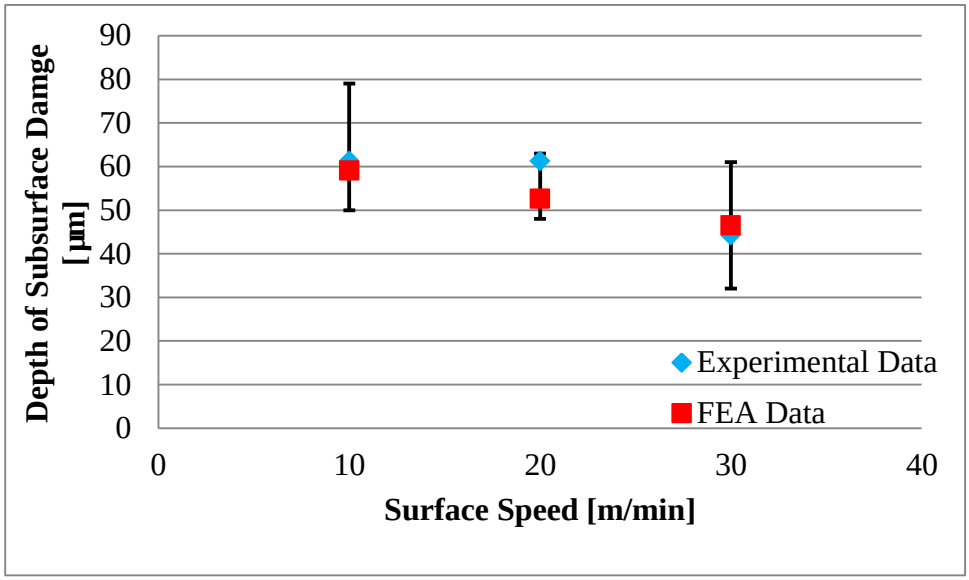

Figure 82: PEEQ vs Recrystallized Sample with Various Speeds.

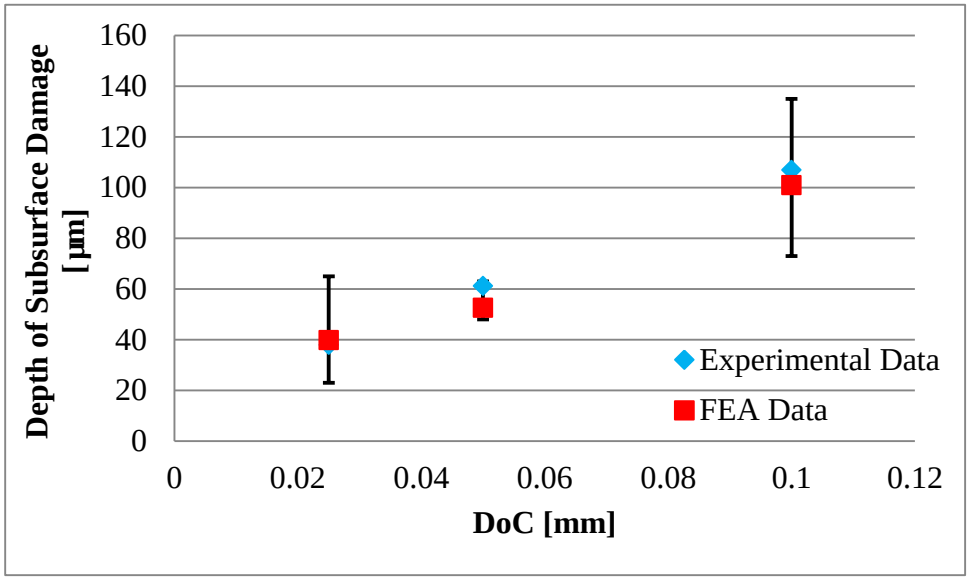

Figure 83: PEEQ vs Recrystallized Sample with Various DoC.

Temperature Contour in Cutting Zone

As mentioned in Chapter 3, the temperature generated in the cutting process is a critical factor influencing the material behavior during orthogonal cutting process, thus the temperature contour predictions from FEA simulation have also been investigated.

In Figure 84, the temperature contour of both cutting tool and workpiece are shown. It is observed that the highest temperature of 1228 °C appeared on the tip of tool near the flank wear zone, which is instantiated by the flank wear from experiments.

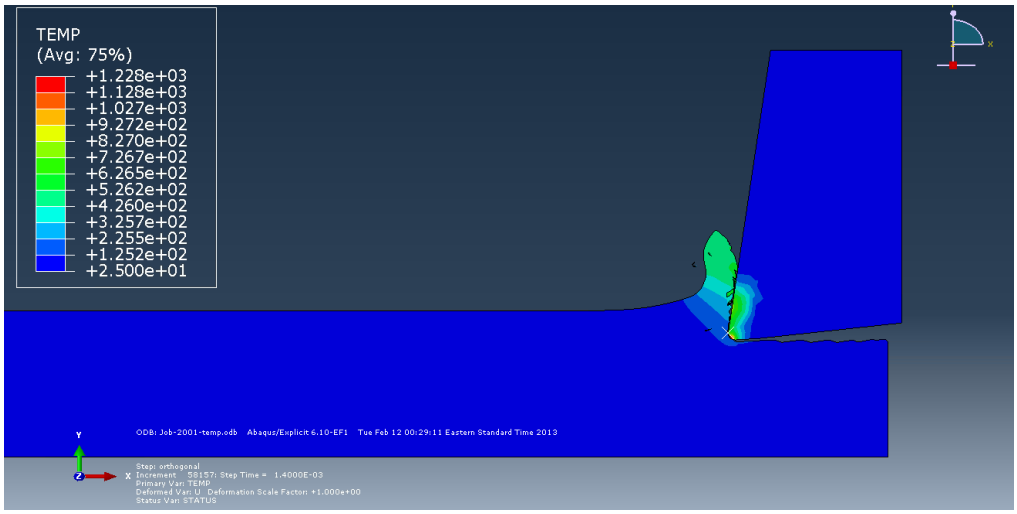

Figure 84: Overall temperature contour during orthogonal simulation for speed: 20 m/min, DoC: 0.1 mm; Temperature in °C.

When investigating the temperature distribution in the workpiece, shown in Figure 85 , the highest temperature point appears at area above the primary shear zone. Because in this area, the chip in this area just went through the plastic deformation and

generated heat, then the chip have friction with the rake face of tool, which generated another amount of energy and conducted into workpiece and tool.

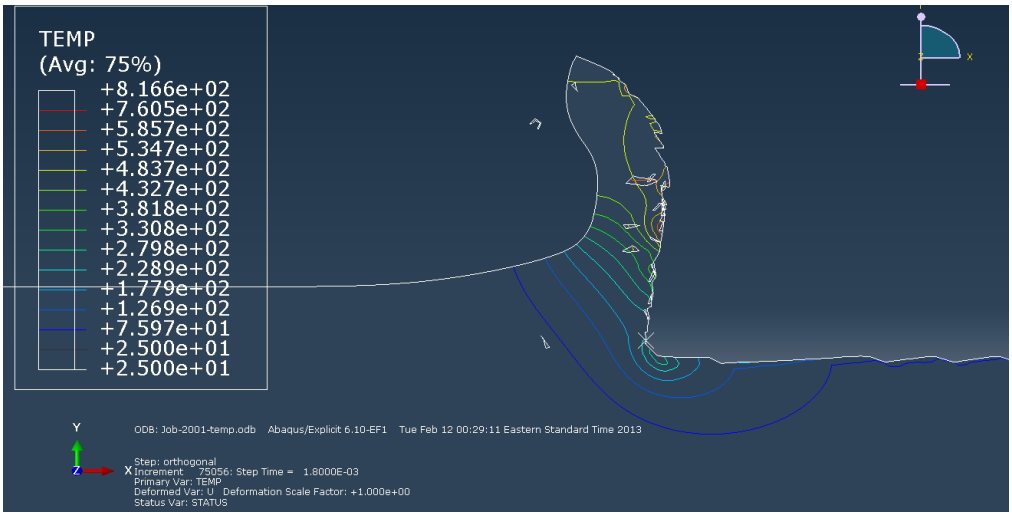

Figure 85: Chip-workpiece contour during orthogonal simulation for speed: 20 m/min, DoC: 0.1 mm; Temperature in °C.

Figure 86 shows temperature contour on the tool. The highest temperature is on the bottom part of the cutting radius, which has a larger friction area. The second highest temperature point is at the chip-tool contact position. Because the higher temperature chip form primary shear zone brought a lot of heat. Meanwhile, more heat is generated from the friction on the rake face. So friction heat conducts in to workpiece and tool at chip-tool contact position. Because the tool has higher thermal conductivity as compared to GTD111, more heat flows into the rake face of the tool in the contacting area. This may be an explanation of the rapid tool wear observed during the experiments, since more heat weaks the wear resistance of the cutting tool.

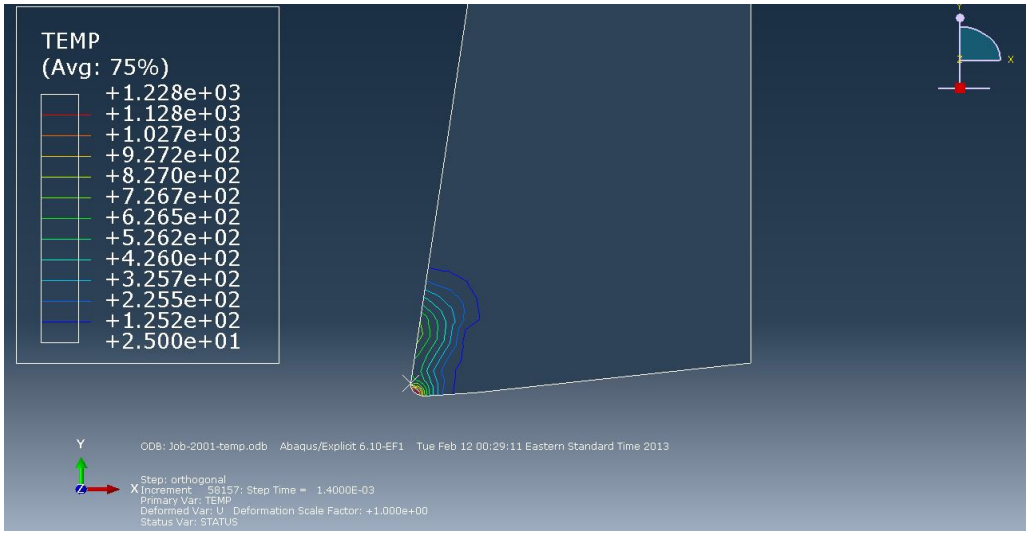

Figure 86: Cutting Tool contour during orthogonal simulation for speed: 20 m/min, DoC: 0.1 mm; Temperature in °C.

From the temperature contour, it is concluded that the anomalous strengthening temperature appear on a relatively small portion on the chips. Most area of the chip and machined surface is still dominated by thermal softening. Tool tip has a relatively higher temperature, which is the reason severe tool wear always appeared from experiments.

Statistical Analysis on Subsurface Damage

Orthogonal cutting includes two factors, such as: depth of cut and surface speed. With two factors and two levels, the full DOE are designed for FEA simulation. Two surface speeds are selected, one at the lower level of 10 m/min and one at the higher level of 20 m/min. Furthermore, two depth of cut are chosen at 0.025 mm and 0.05 mm. With these combination of cutting inputs, the FEA code is developed accordingly. Using the

threshold von Mises stress 1050 MPa to determine the boundary of subsurface damage, the results are summarized in Table 19.

Table 19 FEA Results.

Surface Speed [m/min]	Depth of Cut [mm]	Depth of Subsurface Damage [μm]
10	0.025	43.3
	0.05	62
20	0.025	38.0
	0.05	61.3

Using the results listed in Table 19, the statistic tool Minitab is applied to develop a statistic model for orthogonal cutting. By taking the two factors and the coupling effect into consideration, a second order orthogonal cutting model for the depth of subsurface damage as a function of cutting parameters is derived as:

$$Depth = 54.5 - 2.0 \cdot Speed + 164.0 \cdot DoC + 38.4 \cdot Speed \cdot DoC, \qquad (6.3)$$

With the statistic model, Figure 87 is obtained.

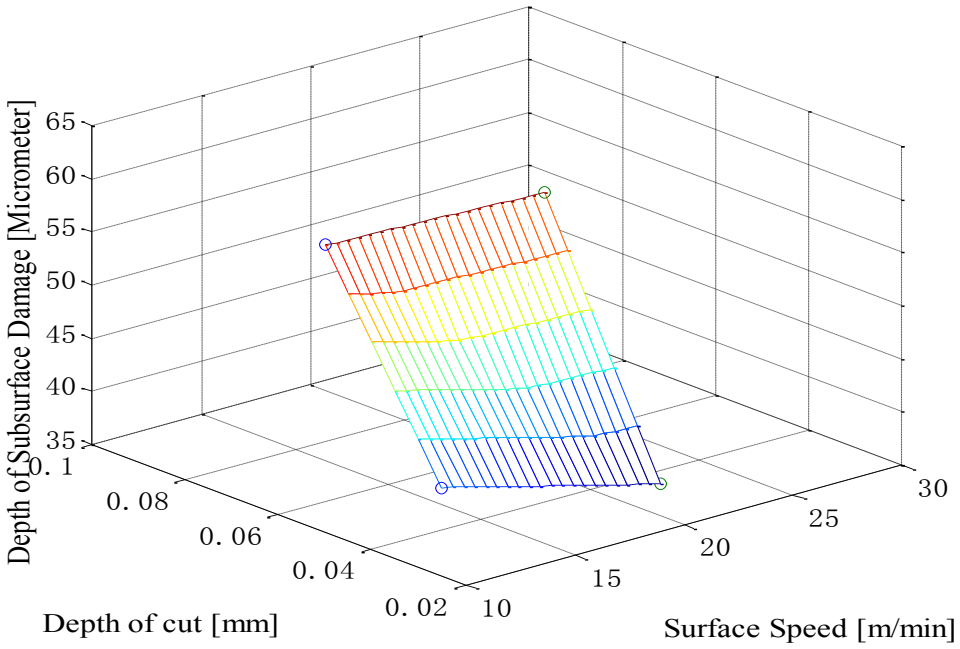

Figure 87: Depth of subsurface damage versus DoC and Surface Speed.

A main effect analysis is shown in Figure 88. The depth of cut is the main factor influencing the depth of subsurface damage. The higher depth of cut induces higher subsurface damage. Surface speed brings in negative affect to depth of subsurface damage. Figure 89 shows the contour between depth of subsurface damage versus depth of cut (DoC) and surface speed.

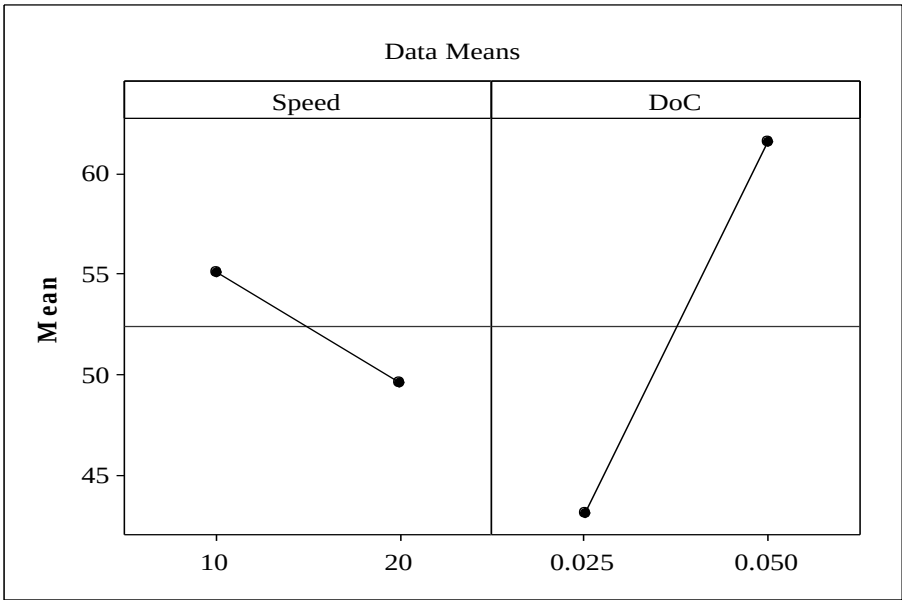

Figure 88: Main Effects Analysis for Depth of Subsurface Damage.

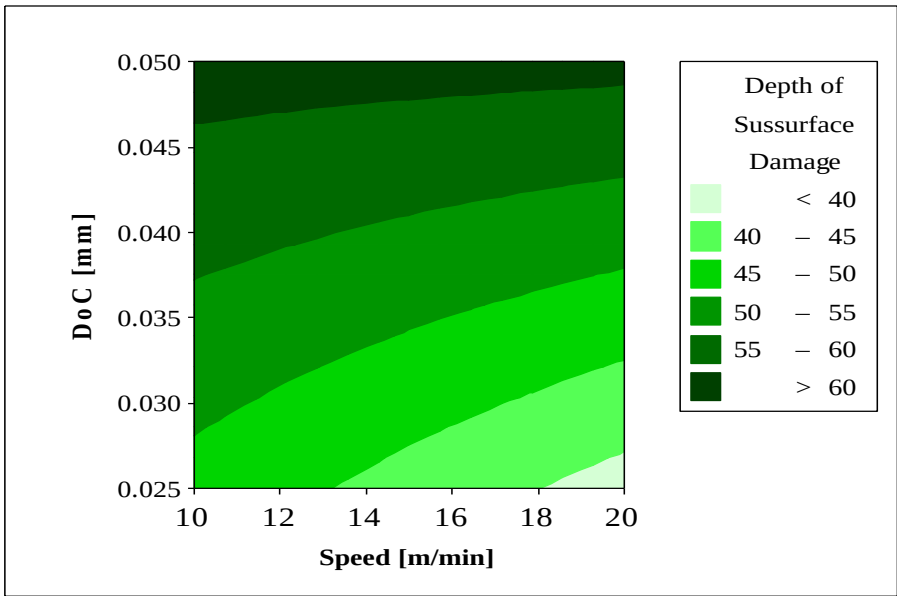

Figure 89: Contour between depth of subsurface damage vs. DoC and Speed.

In conclusion, in order to fulfill a higher material remove rate and keep lower subsurface damage, the higher speed with lower depth of cut is preferred.

CHAPTER SEVEN

SUMMARY AND CONCLUSIONS

In this research, material constitutive model and FEA orthogonal cutting simulation is investigated for γ'-strengthened nickel-based superalloys. The methodology for deriving the constitutive model is proposed by adding modifying terms to the Johnson-Cook model. The material testing data for GTD111 at various temperatures are studied in order to understand the anomalous behavior of the material when the temperature is varied, specifically the increase in strength at a high temperatures range. Another objective is to determine appropriate methods for modeling accurately that behavior. The modifiers in the novel constitutive model include strain hardening function, temperature sensitivity function, flow softening function and the piecewise method.

Based on the novel constitutive model of the γ'-strengthened nickel-based superalloy, explicit subroutine is developed and applied into the ABAQUS/Explicit solver to evaluate the cutting forces, cutting zone temperatures and a measure of the subsurface damage. Also, the orthogonal cutting experimental results are derived and compared with simulation results for validation purposes. The reaction forces agreement between FEA simulation and experiments is within 20%. Meanwhile, in order to obtain more objective results when estimating the subsurface damage, thermal recrystallization technique is utilized as the post-analysis of orthogonal cutting samples. A threshold value of 1050MPa is selected to determine the depth of subsurface damage for FEA simulations. With this threshold value, the agreement between the depth of subsurface damage

measured for the recrystallized samples and the values estimated in the FEA simulations is higher than 90%. A series of simulations under varying cutting conditions are executed, and a model of depth of subsurface damage as a function of cutting inputs is established. In order to make the material model and the subsurface damage model more robust, additional tensile tests at different strain rates must be conducted.

Contributions

During this research, a methodology of establishing the machining model for γ'-strengthened nickel-based superalloy is formulated. The contributions of this research are:

- The modified Johnson-Cook constitutive model is developed using elevated temperature uniaxial tensile tests data by introducing physics-based functions into the Johnson-Cook model.

- Explicit/implicit stress update theory is developed and coded with Intel FORTRAN to depict this modified constitutive model. This theory is applied in more commercial FEA code with various material models.

- Finite element analysis is accomplished based on ABAQUS/Explicit solver to simulate orthogonal cutting process.

- Orthogonal cutting model to predict subsurface damage is established to predict the depth of subsurface damage at various cutting inputs.

In a certain temperature range, anomalous strengthening phenomenon is observed for nickel-based superalloys. In order to depict this behavior, a piecewise method is

adapted for various temperature ranges. If increased accuracy is needed, some other functions can be brought into the constitutive model, depending on the material behavior during the elevated temperature tensile tests.

With the explicit/implicit stress update theory, the user defined material model can be depicted in commercial FEA code, which gives researcher more flexibility to use novel material models.

Impact of Research

The intellectual merit of this research consists in the formulation of an improved constitutive material model capable to accurately predict the anomalous strength behavior of γ'-strengthened nickel-based superalloys at various temperatures. The improved model is further applied in finite element analysis, leading to a better understanding of the cutting mechanism of these advanced materials. From the simulations, a correlation of the subsurface damage with the cutting parameters is developed for orthogonal cutting. Moreover, the methodology developed in this research is applicable any other advanced superalloys from the same category with GTD111. Also, the application in FEA can extend to other cutting process with more complex geometries, and a model for prediction of subsurface damage is established.

For industry, this research has immediate impact if the subsurface damage model is applied. By controlling the machining parameters, acceptable levels of subsurface

damage are obtained according to the requirements from the customers, and the number of defective parts is reduced, increasing productivity. Also, higher surface speed and lower depth of cut is recommended to obtain lower depth of subsurface damage and ensure a relatively high material remove rate.

Bounds of Applicability

From this research, the cutting force and depth of subsurface damage are in good agreement with the experimental results. However, there are some boundaries for this methodology:

- Strain rate sensitivity coefficient is obtained from Inconel 718 from literature. This must be verified or improved for each γ'-strengthened nickel-based superalloys.
- For machining FEA simulation, the accuracy of the material model and friction coefficient are two adjustable variables. The friction along the cutting edge must be more accurately determined.
- Since both FEA simulations and experiments are dry cutting (without coolant), the tool wear is severe even after short cutting distance. The cutting inputs are limited to a less aggressive level.

Recommendations

This research is the foundation for the development of a FEA model for machining process. There are several aspects that may be studied further:

- Strain rate sensitivity can be improved by performing the split Hopkinson bar tests at various temperatures.
- In this research, the constitutive model of GTD111 is treated as an accurate model and friction coefficient is adjusted accordingly. The friction coefficient in the cutting zone can be identified in greater detail.
- Material failure model can be developed in order to obtain the serrated chips from FEA simulation.

APPENDICES

Appendix A

FEA code for orthogonal cutting and user defined material subroutine are shown in this section.

Finite Element Analysis Code (input file)

```
*Heading
** Job name: Job-718 Model name: Model-1
** Generated by: Abaqus/CAE 6.10-EF1
*Preprint, echo=NO, model=NO, history=NO, contact=NO
**
** PARTS
**
*Part, name=tool
*Node
  [35751 Nodes Defination]
*Element, type=CPE4RT
  [35000 Elemnents Defination]
*Elset, elset=_PickedSet2, internal, generate
    1,  35000,      1
** Section: workpiece
*Solid Section, elset=_PickedSet2, controls=EC-2, material=workpiece
,
*End Part
**
**
** ASSEMBLY
**
*Assembly, name=Assembly
**
*Instance, name=tool-1, part=tool
0.00490899999999989,     4.893015,           0.
*End Instance
**
*Instance, name=workpiece-1, part=workpiece
        1.5,       -2.375,           0.
*End Instance
**
*Node
      1, 0.00858448632, -0.0775813162,           0.
*Nset, nset=_PickedSet64, internal
 1,
```

```
*Nset, nset=Set-2
 1,
*Nset, nset=_PickedSet87, internal
 1,
*Nset, nset=workpiecenode, instance=workpiece-1, generate
     1,  35751,      1
*Nset, nset=_PickedSet92, internal, instance=workpiece-1, generate
     1,  35751,      1
*Nset, nset=_PickedSet93, internal, instance=workpiece-1, generate
 35051,  35751,      1
*Elset, elset=_PickedSet95, internal, instance=workpiece-1, generate
     1,  35000,      1
*Elset, elset=_PickedSet97, internal, instance=tool-1, generate
   1,  117,    1
*Nset, nset=_PickedSet98, internal, instance=tool-1, generate
   1,  142,    1
*Nset, nset=_PickedSet98, internal, instance=workpiece-1, generate
     1,  35751,      1
*Elset, elset=__PickedSurf96_S1, internal, instance=tool-1
   4,  10,  11,  12,  13,  16,  31,  34,  43,  46,  47, 114
*Elset, elset=__PickedSurf96_S2, internal, instance=tool-1
   3,   5,  19,  20,  21,  34,  44,  48,  49,  50,  51,  54, 112, 115
*Elset, elset=__PickedSurf96_S3, internal, instance=tool-1
   8,  24,  26,  32,  35,  36,  57,  67,  69,  76,  78,  95,  96,  97,  99, 102
*Elset, elset=__PickedSurf96_S4, internal, instance=tool-1
 18, 23, 27, 28, 31, 43, 45, 70
*Surface, type=ELEMENT, name=_PickedSurf96, internal
__PickedSurf96_S1, S1
__PickedSurf96_S2, S2
__PickedSurf96_S4, S4
__PickedSurf96_S3, S3
*Surface, type=NODE, name=_PickedSet92_CNS_, internal
_PickedSet92, 1.
** Constraint: Constraint-1
*Rigid Body, ref node=_PickedSet87, elset=_PickedSet97
*End Assembly
**
** ELEMENT CONTROLS
**
*Section Controls, name=EC-1, hourglass=RELAX STIFFNESS
1., 1., 1.
*Section Controls, name=EC-2, DISTORTION CONTROL=NO, hourglass=RELAX
STIFFNESS, second order accuracy=YES
1., 1., 1.
```

```
**
** MATERIALS
**
*Material, name=tool
*Conductivity
46.,
*Density
1.4e-9,
*Elastic
 2.01e+5, 0.3
*Expansion
 4.7e-06,
*Inelastic Heat Fraction
        0.9,
*Specific Heat
40.,
*Material, name=workpiece
*Conductivity
18.,
*Density
8.2e-9,
*Depvar,delete=5
      7,
*User Material, constants=20
2.01e5, 0.3, 975., 1970., 0.79, 0.0134,1250., 25.,
1.5, 0.9, 435.,650., 1.1, 1033., -3.,-5.,10., -0.07, 0.71, 7.1e-6
*Specific Heat
435.,
** INTERACTION PROPERTIES
**
*Surface Interaction, name=IntProp-1
*Friction
 0.3,
*Surface Behavior, pressure-overclosure=HARD
** PREDEFINED FIELDS
**
** Name: Predefined Field-1   Type: Temperature
*Initial Conditions, type=TEMPERATURE
_PickedSet98, 25.
** ----------------------------------------------------------------
**
** STEP: orthogonal
**
*Step, name=orthogonal
```

```
*Dynamic Temperature-displacement, Explicit
, 0.01
*Bulk Viscosity
0.06, 1.2
**
** BOUNDARY CONDITIONS
**
** Name: BC-1 Type: Symmetry/Antisymmetry/Encastre
*Boundary
_PickedSet93, ENCASTRE
** Name: BC-2 Type: Velocity/Angular velocity
*Boundary, type=VELOCITY
_PickedSet64, 1, 1, -333.
_PickedSet64, 2, 2
_PickedSet64, 6, 6
*Adaptive Mesh Controls, name=Ada-1, curvature refinement=5.
1., 0., 0.
*Adaptive Mesh, elset=_PickedSet95, controls=Ada-1, op=NEW
**
** INTERACTIONS
**
** Interaction: Int-1
*Contact Pair, interaction=IntProp-1, mechanical constraint=PENALTY, cpset=Int-1
_PickedSurf96, _PickedSet92_CNS_
**
** OUTPUT REQUESTS
**
*Restart, write, number interval=1, time marks=NO
**
** FIELD OUTPUT: F-Output-1
**
*Output, field, number interval=200
*Node Output
A, NT, RF, RFL, U, V
*Element Output, directions=YES
PE, PEEQ, PEEQVAVG, PEVAVG, RHOE, RHOP, S
SDV, STATUS, SVAVG, TEMP, UVARM
*Contact Output
CSTRESS,
**
** FIELD OUTPUT: F-Output-2
**
*Node Output, nset=Set-2
RF, U
```

```
**
** HISTORY OUTPUT: H-Output-1
**
*Output, history, variable=PRESELECT, time interval=0.0001
*End Step
```

VUMAT (FORTRAN Code)

```
c   *Material, name=jc

      subroutine vumat(
c Read only -
     1  nblock, ndir, nshr, nstatev, nfieldv, nprops, lanneal,
     2  stepTime, totalTime, dt, cmname, coordMp, charLength,
     3  props, density, strainInc, relSpinInc,
     4  tempOld, stretchOld, defgradOld, fieldOld,
     3  stressOld, stateOld, enerInternOld, enerInelasOld,
     6  tempNew, stretchNew, defgradNew, fieldNew,
c Write only -
     5  stressNew, stateNew, enerInternNew, enerInelasNew )
c
      include 'vaba_param.inc'
c
c For 2D/3D cases using the Mises Plasticity with modified Johnson-Cook isotropic
hardening.
c
c
c
      dimension coordMp(nblock,*), charLength(nblock), props(nprops),
     1     density(nblock), strainInc(nblock,ndir+nshr),
     2     relSpinInc(nblock,nshr), tempOld(nblock),
     3     stretchOld(nblock,ndir+nshr),
     4     defgradOld(nblock,ndir+nshr+nshr),
     5     fieldOld(nblock,nfieldv), stressOld(nblock,ndir+nshr),
     6     stateOld(nblock,nstatev), enerInternOld(nblock),
     7     enerInelasOld(nblock), tempNew(nblock),
     8     stretchNew(nblock,ndir+nshr),
     9     defgradNew(nblock,ndir+nshr+nshr),
     1     fieldNew(nblock,nfieldv),
     2     stressNew(nblock,ndir+nshr), stateNew(nblock,nstatev),
     3     enerInternNew(nblock), enerInelasNew(nblock)
c
c
```

```
      parameter ( zero = 0.d0, vp5 = 1.5, half = 0.5d0,
     * vp8 = -1.8,five = -5.d0, one = 1.d0, two = 2.d0,
     * third = 1.d0 / 3.d0)
c
c
c
        e=props(1)
        xnu=props(2)
        Va=props(3)
        Vb=props(4)
        Vn=props(5)
        Vc=props(6)
        Tm=props(7)
        Tr=props(8)
        vm=props(9)
        Fracheat=props(10)
        Speheat=props(11)
        Temr1=props(12)
        oneone=props(13)
        Temr2=props(14)
        three=props(15)
        five=props(16)
        ten=props(17)
        ps=props(18)
        psv=props(19)
       Coe_exp=props(20)
c
c
      tmu = e / ( one + xnu )
      alamda = xnu * tmu / ( one - two * xnu )
      thremu = vp5 * tmu
      vk=e/(1-2*xnu)
c

      if ( stepTime .eq. zero ) then
        do k = 1, nblock
c     Trial stress
        trace = strainInc(k,1) + strainInc(k,2) + strainInc(k,3)

        stressNew(k,1) = stressOld(k,1)
     *       + tmu * strainInc(k,1) + alamda * trace
        stressNew(k,2) = stressOld(k,2)
     *       + tmu * strainInc(k,2) + alamda * trace
        stressNew(k,3) = stressOld(k,3)
```

```
     *       + tmu * strainInc(k,3) + alamda * trace
             stressNew(k,4)=stressOld(k,4) + tmu * strainInc(k,4)
             if (nshr.gt.1) then
             stressNew(k,5)= stressOld(k,5) + tmu * strainInc(k,5)
             stressNew(k,6) = stressOld(k,6) + tmu * strainInc(k,6)
             end if
             stateOld(k,1) = 1.0e-10
             stateOld(k,2) = 0.0
             stateOld(k,3) = 975.
             stateOld(k,4) = 25.
           end do
         else
c
           do k = 1, nblock
c           print*,nshr,'-------------------shear'

           trace = strainInc(k,1) + strainInc(k,2) + strainInc(k,3)

             s11 = stressOld(k,1)
     *       + tmu * strainInc(k,1) + alamda * trace
             s22 = stressOld(k,2)
     *       + tmu * strainInc(k,2) + alamda * trace
             s33 = stressOld(k,3)
     *       + tmu * strainInc(k,3) + alamda * trace
             s12=stressOld(k,4) + tmu * strainInc(k,4)
c
             if (nshr .gt. 1) then
             s23= stressOld(k,5) + tmu * strainInc(k,5)
             s13 = stressOld(k,6) + tmu * strainInc(k,6)
             end if
             sdvt=(s11+s22+s33)/3
             s11=s11-sdvt
             s22=s22-sdvt
             s33=s33-sdvt
c             print*,s11,s22,s33,'sssssssssssssssss'

           if (nshr .eq. 1) then
           vmises = sqrt( vp5 * ( s11 * s11 + s22 * s22 + s33 * s33 +
     * two * s12 * s12 ) )
           else
              vmises = sqrt( vp5 * ( s11 * s11 + s22 * s22 + s33 * s33 +
     * two * s12 * s12 + two * s13 * s13 + two * s23 * s23 ) )
           end if
c
```

```
      peeqOld=stateOld(k,1)     !strain at the beginning of time step
           peeq_rate=stateOld(k,2)   !strain rate at the beginning of time step
           yield= stateOld(k,3)
           temp=stateOld(k,4)
c         print*,stateOld(k,1),'----------stateOld(k,1)'
          if(peeqOld.eq.zero) then
           yield = Va
       end if
c      print*,vmises,'----------vmises'
c      print*,yield,'----------yield'
c
c the differnece between trial stress and yield stress
c
          sigdif = vmises - yield
c         print*,sigdif
c
     if(sigdif .GT. 0)then
c       print*,'----------------------flag'
     if(temp .lt. Tr)then
               temp = Tr
              end if

              if(temp .GT. Tm)then
                tt=0
              else
                t1=(temp-Tr)/(Tm-Tr)
                tt=1-(exp(-0.85))*t1**vm
              end if
c             write(200,*)t1,tt
c
           if(peeq_rate .lt. 1)then
                peeq_rate=1
            end if
c to calculate h, Vartial differential of PEEQ

ccccccccccccccccccccccccccccccccccccccccccccccccccccccccccccccccccccc

              if(peeqOld .eq.zero) then
             hard=thremu
          else
             hard=Vb*Vn*(peeqOld**(Vn-1))*(1+Vc*log(peeq_rate))*tt
          end if

ccccccccccccccccccccccccccccccccccccccccccccccccccccccccccccccccccccc
```

```
ccccccccccccccccccccccccccccccccccccccccccccccccccccccccccccccccccccccc
c
c Delta PEEQ
c
              deqps=sigdif/(thremu+hard)
c
              peeqOld=peeqOld+deqps
c
              peeq_rate=deqps/dt
c
              tvp=1+Vc*log(peeq_rate)

c
c calculate yield stress form updated PEEQ
c
              yield=(Va+Vb*(peeqOld**Vn))*tvp*tt
c
c calculate the inelastic heat
c
         deltemp=Fracheat*yield*deqps/( density(nblock)*Speheat)
         deftemp=deltemp*Coe_exp
c
c modification factor
c
              mfactor=yield/vmises
c
              stateOLd(k,1)=peeqOld
              stateOLd(k,2)=peeq_rate
              stateOLd(k,3)=yield
              stateOLd(k,4)=temp+deltemp
c
           else

              mfactor=1
              peeq_rate=0
              deqps=0
              deltemp=0

           end if
c
c Update the stress
c
      stressNew(k,1) = s11 * mfactor+ sdvt !+vk*(trace/3-deftemp)
      stressNew(k,2) = s22 * mfactor+ sdvt !+vk*(trace/3-deftemp)
```

```
      stressNew(k,3) = s33 * mfactor+ sdvt !+vk*(trace/3-deftemp)
      stressNew(k,4) = s12 * mfactor
      if (nshr .gt. 1) then
      stressNew(k,5) = s23 * mfactor
      stressNew(k,6) = s13 * mfactor
      end if
c
c Update the state variables
c
      stateNew(k,1)=stateOLd(k,1)
      stateNew(k,2)=stateOLd(k,2)
           stateNew(k,3)=stateOld(k,3)
           stateNew(k,4)=stateOld(k,4)
           stateNew(k,6)=stressNew(k,1)
           stateNew(k,7)=stressNew(k,3)
             if ( stateNEW(k,1).LT.1.3)then
        statenew(k,5)=1
             else
        statenew(k,5)=0
        endif
c
c Update the specific internal energy -
c
      if (nshr .eq.. 1) then
      stressPower = half * (
     * ( stressOld(k,1) + stressNew(k,1) ) * strainInc(k,1) +
     * ( stressOld(k,2) + stressNew(k,2) ) * strainInc(k,2) +
     * ( stressOld(k,3) + stressNew(k,3) ) * strainInc(k,3) ) +
     * ( stressOld(k,4) + stressNew(k,4) ) * strainInc(k,4)
       else
       stressPower = half * (
     * ( stressOld(k,1) + stressNew(k,1) ) * strainInc(k,1) +
     * ( stressOld(k,2) + stressNew(k,2) ) * strainInc(k,2) +
     * ( stressOld(k,3) + stressNew(k,3) ) * strainInc(k,3) ) +
     * ( stressOld(k,4) + stressNew(k,4) ) * strainInc(k,4) +
     * ( stressOld(k,5) + stressNew(k,5) ) * strainInc(k,5) +
     * ( stressOld(k,6) + stressNew(k,6) ) * strainInc(k,6)
       end if
c
      enerInternNew(k) = enerInternOld(k) + stressPower / density(k)
c
c Update the dissipated inelastic specific energy -
c
      plasticWorkInc = yield * deqps
```

```
      enerInelasNew(k) = enerInelasOld(k)
     * + plasticWorkInc / density(k)

        end do

      end if
c
      return
      end
```

Appendix B

With different convergence criterion, implicit method is compared on one element, as shown in Figure 90 Figure 91 . Also, explicit method and CAE are investigated as well, as shown in Figure 92 and Figure 93.

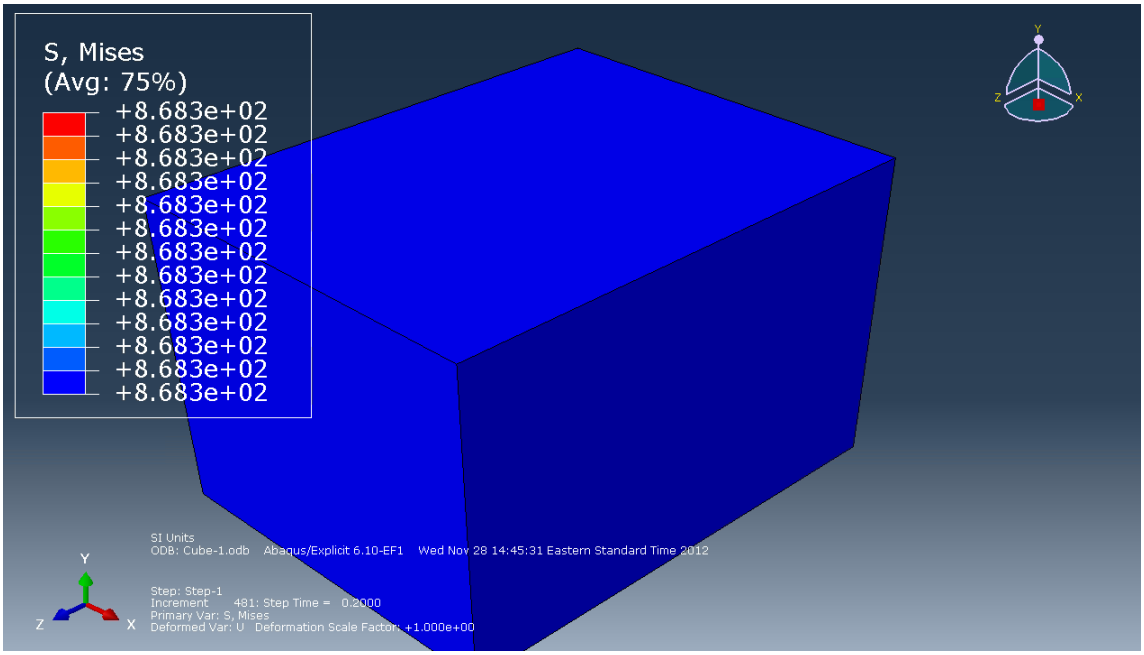

Figure 90: Implicit - One Element with convergence 10^{-5}.

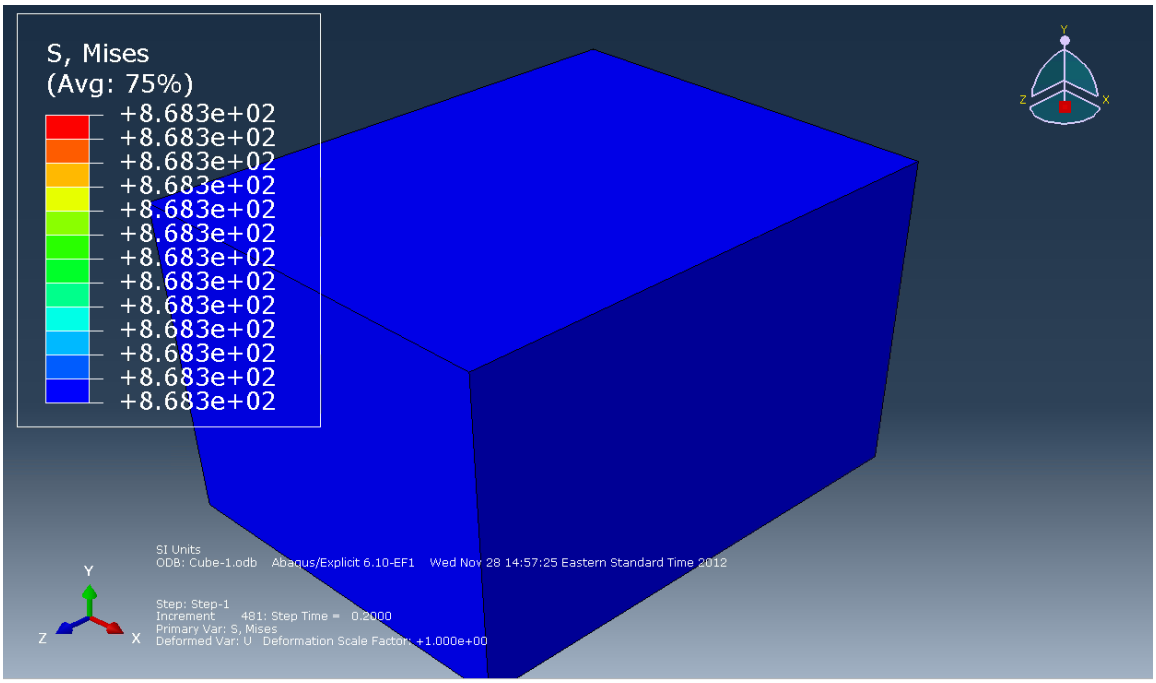

Figure 91: Implicit - One Element with convergence 10^{-10}.

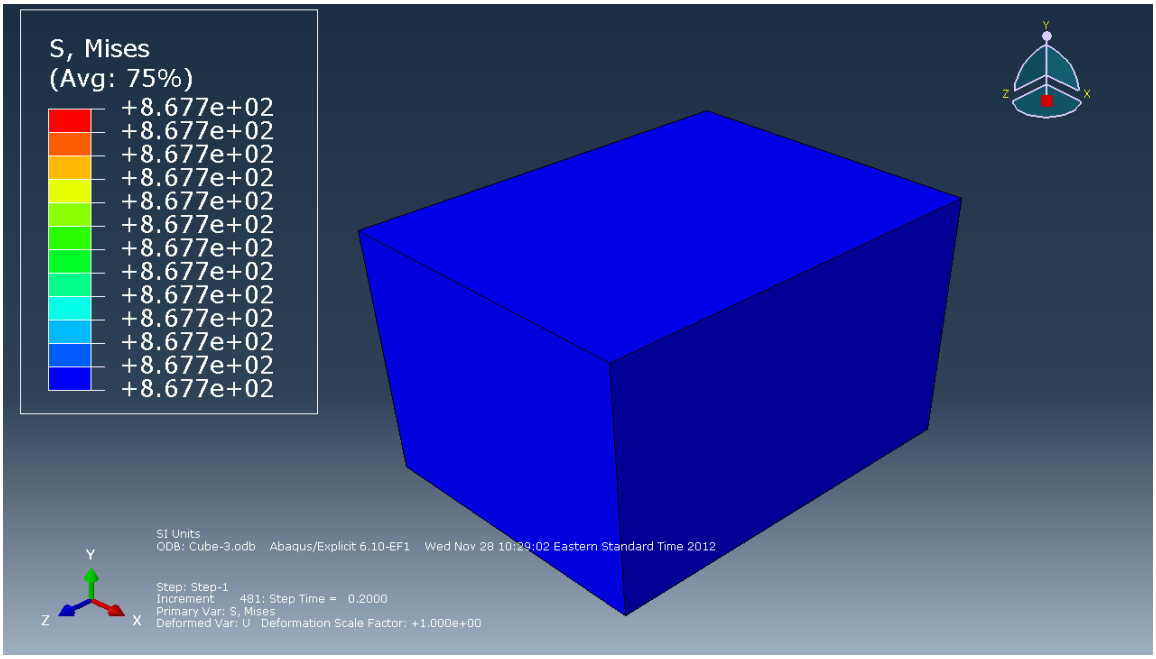

Figure 92: Explicit - One Element.

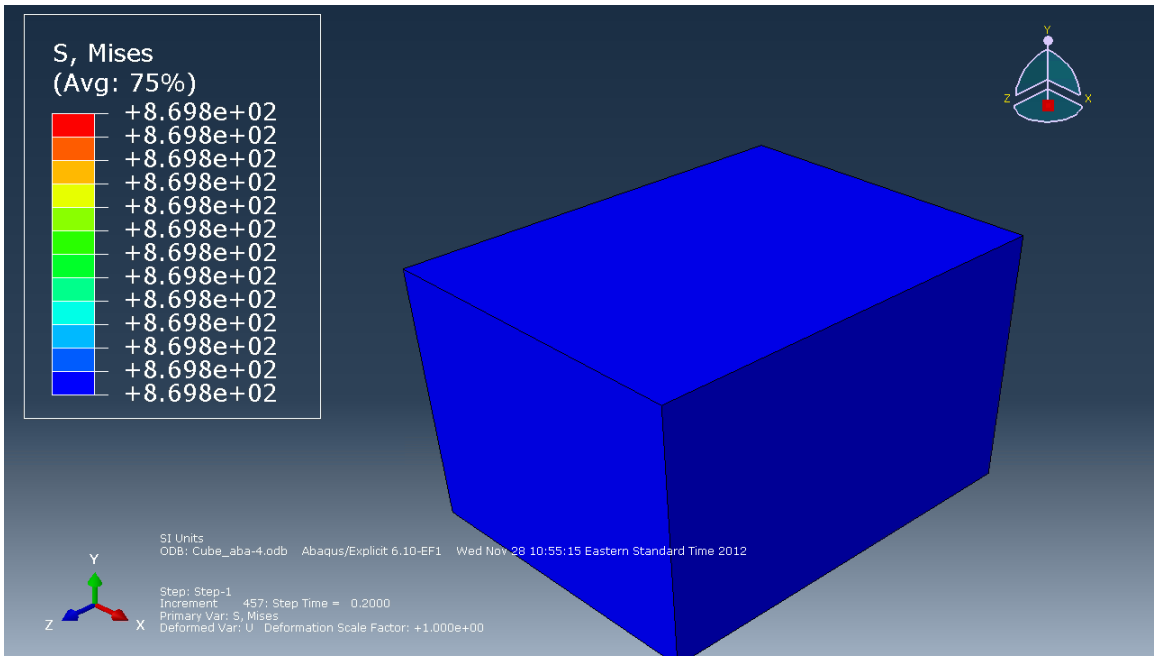

Figure 93: CAE – One Element.

Appendix C

With FEA simulation, temperature contour is obtained from Figure 94 to Figure 99.

Temperature contours of chip

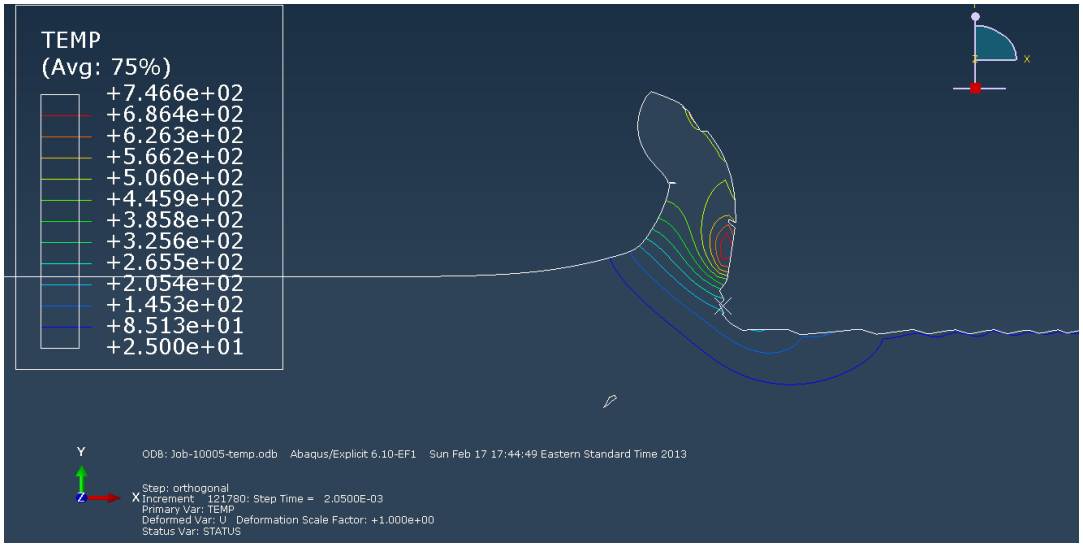

Figure 94: Temperature contour for speed: 10 m/min, DoC: 0.05 mm; Temperature in °C.

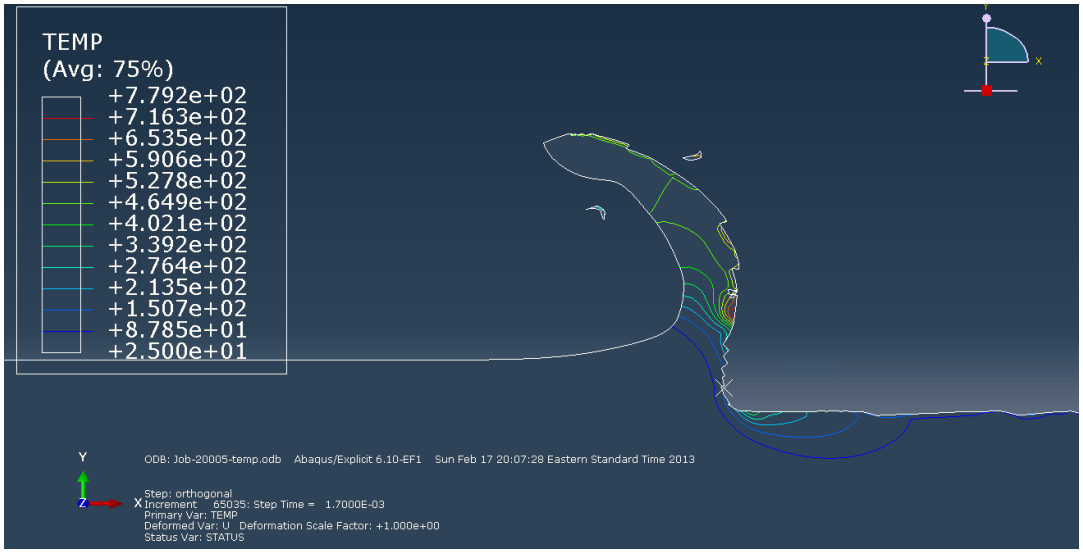

Figure 95: Temperature contour for speed: 20 m/min, DoC: 0.05 mm; Temperature in °C.

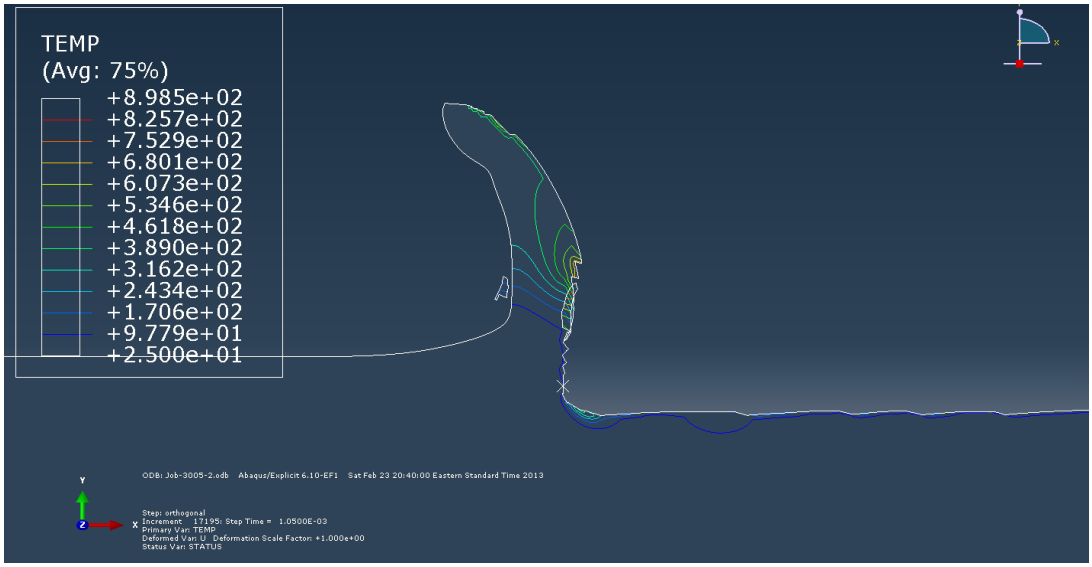

Figure 96: Temperature contour for speed: 30 m/min, DoC: 0.05 mm; Temperature in °C.

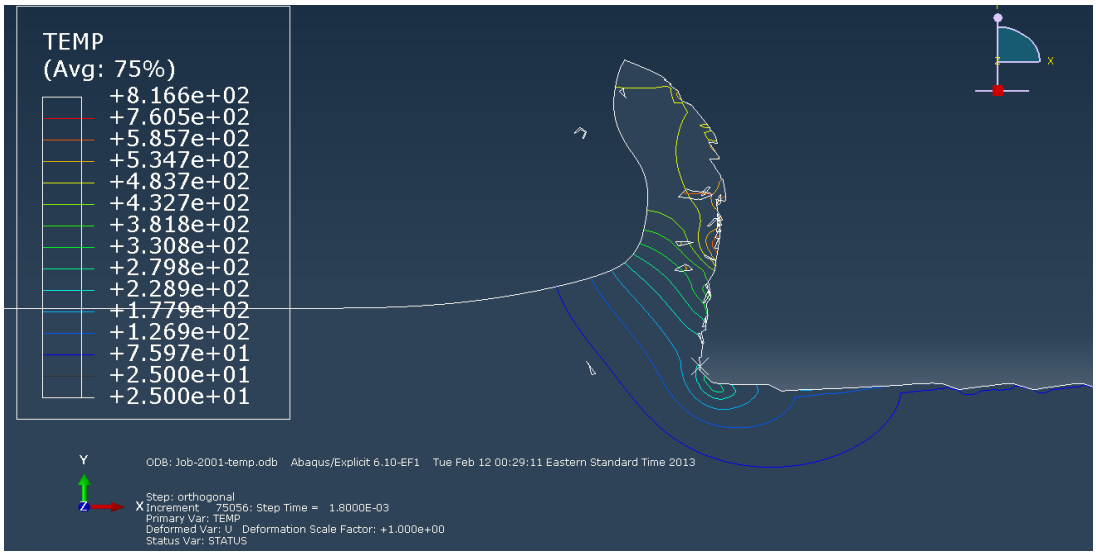

Figure 97: Temperature contour for speed: 20 m/min, DoC: 0.1 mm; Temperature in °C.

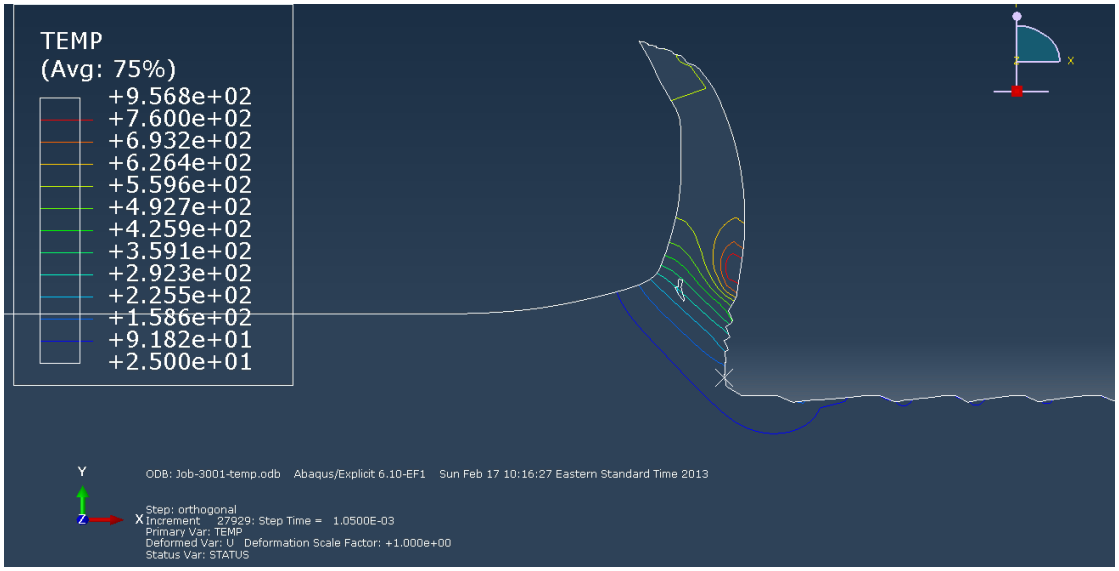

Figure 98: Temperature contour for speed: 30 m/min, DoC: 0.1 mm; Temperature in °C.

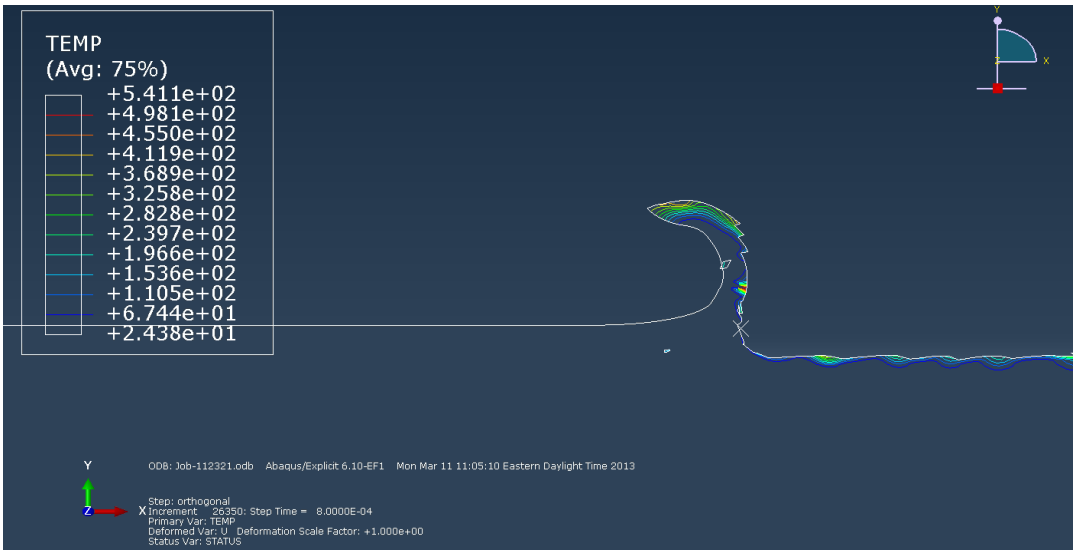

Figure 99: Temperature contour for speed: 20 m/min, DoC: 0.025 mm; Temperature in °C.

Equivalent plastic strain contour

With FEA simulation, the PEEQ contour is obtained from Figure 100 to Figure 105.

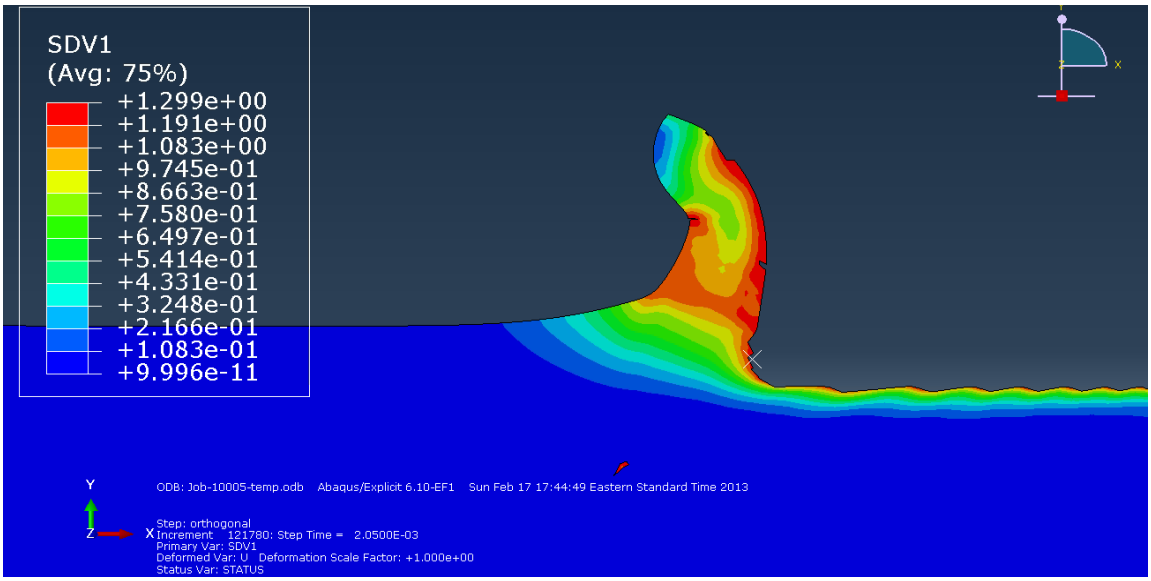

Figure 100: Equivalent plastic strain contour for speed: 10 m/min, DoC: 0.05 mm.

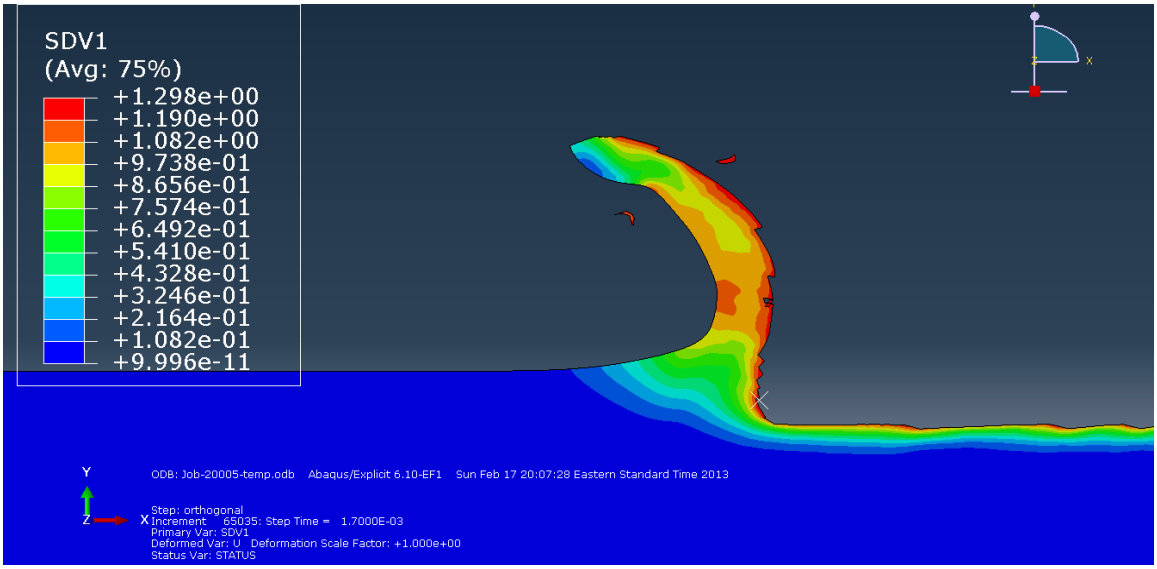

Figure 101: Equivalent plastic strain contour for speed: 20 m/min, DoC: 0.05 mm.

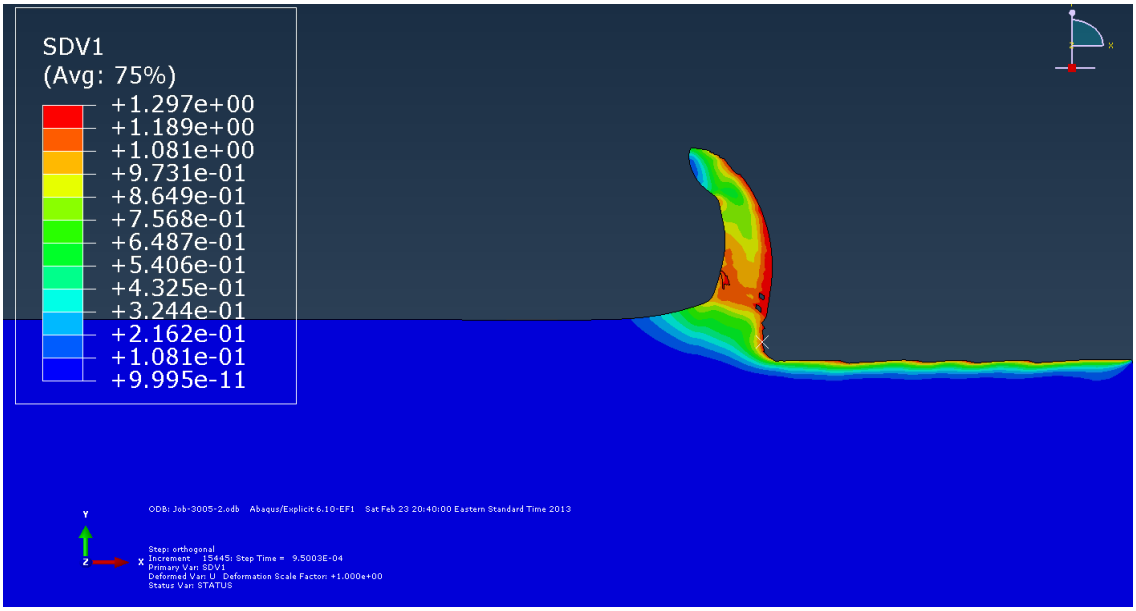

Figure 102: Equivalent plastic strain contour for speed: 30 m/min, DoC: 0.05 mm.

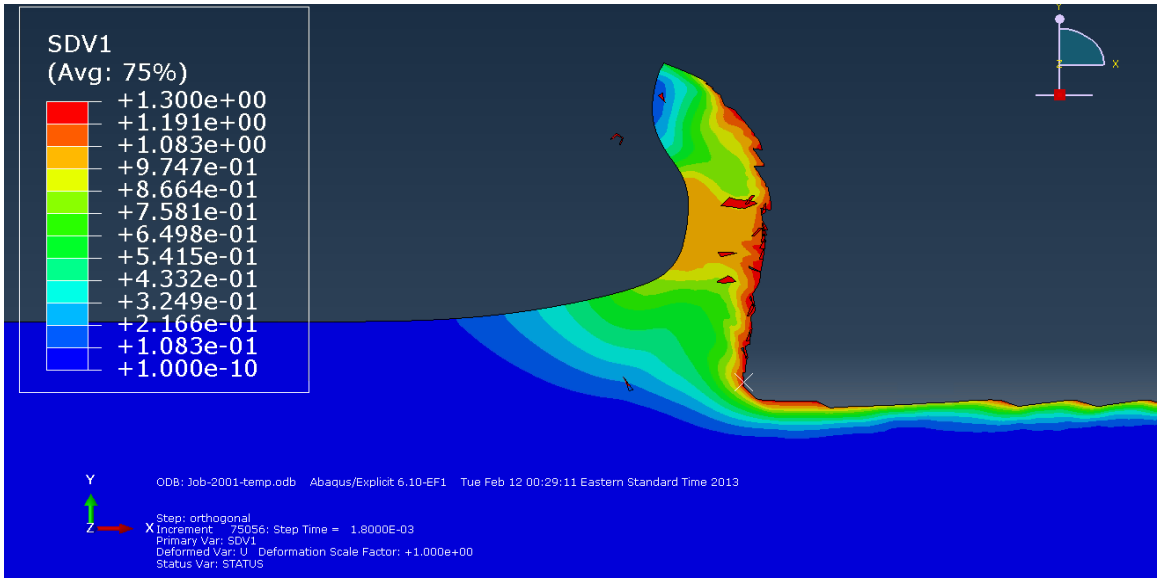

Figure 103: Equivalent plastic strain contour for speed: 20 m/min, DoC: 0.1 mm.

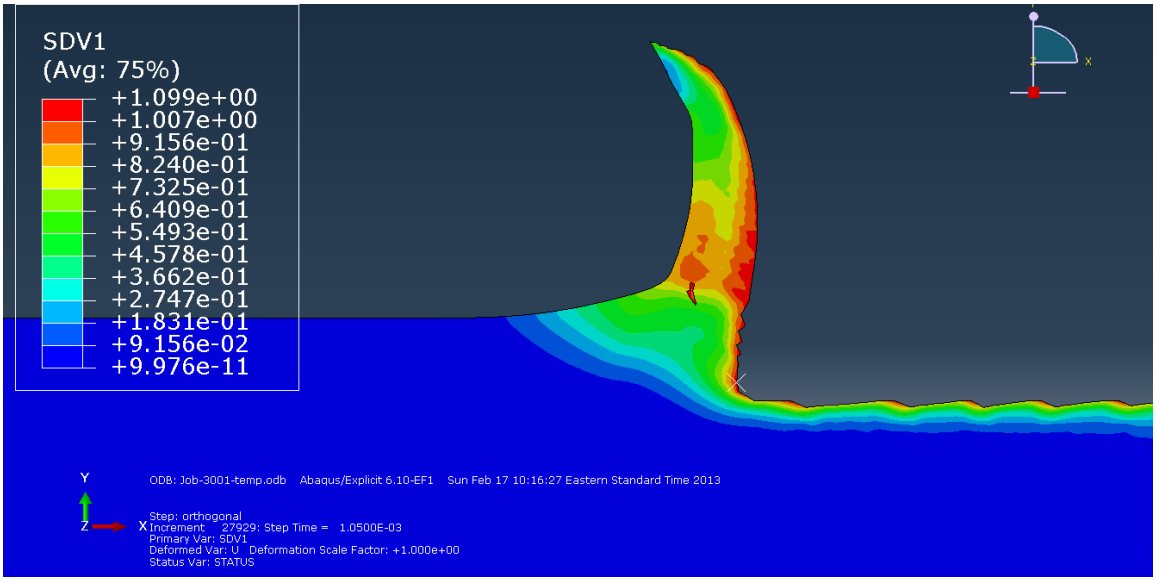

Figure 104: Equivalent plastic strain contour for speed: 30 m/min, DoC: 0.1 mm.

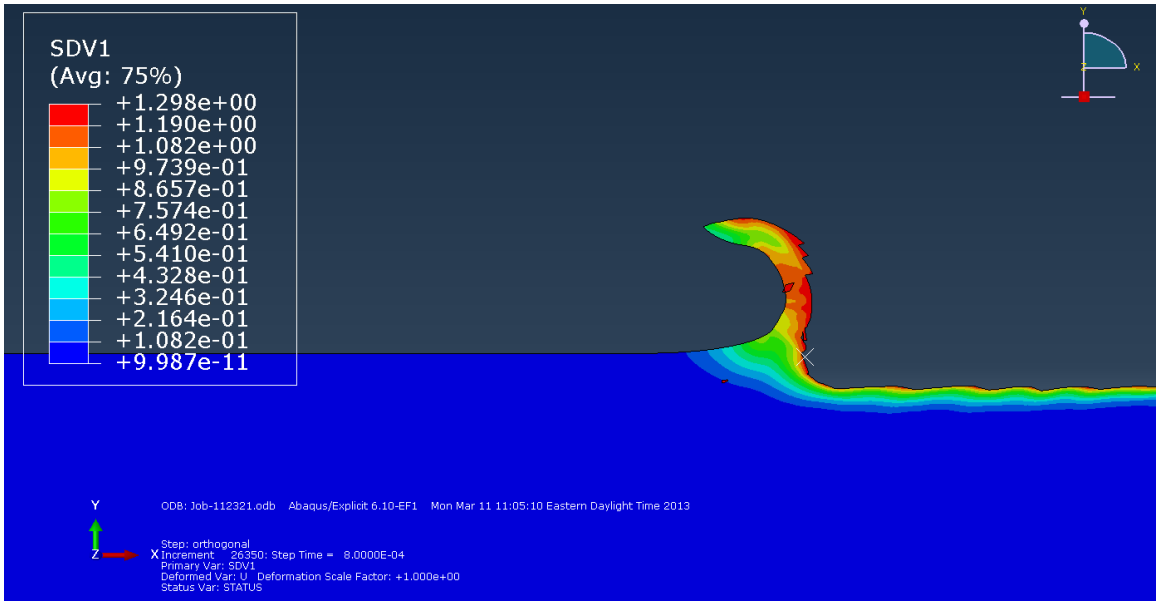

Figure 105: Equivalent plastic strain contour for speed: 20 m/min, DoC: 0.025 mm.

REFERENCES

1. G. Sorell, Corrosion- and heat-resistant nickel alloys guideline for selection and application. Nickel Development Institute, (1998)

2. A. J. Henderson, C. Bunget, T.R. Kurfess, Integration of On- Machine Measurements on the Force Modeling for Machining of Advanced Nickel-Based Superalloys, Proc. Int. Symp. Flex. Autom. (2012)

3. E.O. Ezugwu, Z.M. Wang, A.R. Machado, The machinability of nickel-based alloys: a review, J. Mater. Process. Technol. 86 (1999) 1-16.

4. E.O. Ezugwu, J. Bonney, Y. Yamane, An overview of the machinability of aeroengine alloys, J. Mater. Process. Technol. 134 (2003) 233-253.

5. Ezugwu, E.O. and S.H. Tang, Surface abuse when machining cast iron (G-17) and nickel-base superalloy (Inconel 718) with ceramic tools. Journal of Material Processing Technology, 1995. 55: p. 63-69.

6. A. Ramesh, S.N. Melkote, Modeling of white layer formation under thermally dominant conditions in orthogonal machining of hardened AISI 52100 steel. International Journal of Machine Tools and Manufacture, 48 (2008), pp. 402–414

7. Richardson, B.J., C. Bunget, and T.R. Kurfess, A statistical based determination of the depth of the machining affected zone in nickel-based superalloys using MATLAB. Proceedings of Manufacturing Science and Engineering Conference, Erie, Pennsylvania, 2010. MSEC2010-34327: p. 4.

8. Gas turbine bucket, online source: http://www.powertechnology.com/contractors/operations/wood_group/.

9. Ranganath, S., C. Guo, and P. Hegde, A finite element modeling approach to predict white layer formation in nickel superalloys. CIRP Annals - Manufacturing Technology, 2009. 58: p. 77-80.

10. Mohammed Sima, Tugrul Ozel, Modified materials constitutive models for serrated chip formation simulations and experimental validation in machining of titanium alloy Ti-6Al-4V. International Journal of Machine Tools and Manufacture 50 (2001): 943-960

11. Y. Kevin Chou, Hui Song, Thermal modeling for white layer predictions I finish hard turning. International Journal of Machine Tools and Manufacture, Volune 45, Issue4-5 (2005): pp. 481-495

12. Y. Chen, C. Bunget, L. Mears and T. Kurfess, An Improved Empirical Constitutive Model for Gamma Prime – Strengthened Nickel-Based Superalloys. NAMRC/SME Vol. 41, 2013

13. X. Yang, C.R. Liu, Machining titanium and its alloys. Machining Science and Technology 3.1 (1999): pp. 107–139

14. Mohammed Sima, Tugrul Ozel, Modified materials constitutive models for serrated chip formation simulations and experimental validation in machining of titanium alloy Ti-6Al-4V. International Journal of Machine Tools and Manufacture 50 (2001): 943-960

15. Ezugwu, E.O. and S.H. Tang, Surface abuse when machining cast iron (G-17) and nickel-base superalloy (Inconel 718) with ceramic tools. Journal of Material Processing Technology, 1995. 55: p. 63-69.

16. A. Ginting, M. Nouari. Surface integrity of dry machined titanium alloys. International Journal of Machine Tools and Manufacture, 49 (2009): pp. 325–332

17. Axinte, D.A., et al., Turning of advanced Ni based alloys obtained via powder metallurgy route. Annals of the CIRP, 2006. 55(1): p. 117-120.

18. Muhanmmad Imran, Paul T. Mativenga, Ali Gholinia, Philip J. Withers Evaluation of surface integrity in micro drilling process for nickel-based superalloy.

19. R.S. Pawade, Suhas S. Joshi, P.K. Brahmankar. Effect of machining parameters and cutting edge geometry on surface integrity of high-speed turned Inconel 718. Machine tools and manufacture 48 (2008) 15-28

20. Pawade, R.S., S.S. Joshi, and P.K. Brahmankar, Effect of machining parameters and cutting edge geometry on surface integrity of high-speed turned Inconel 718. International Journal of Machine Tools & Manufacture, 2008. 48: p. 15-28.

21. R. M'Saoubi, J.C. Outeiro, H. Chandrasekaran, O.W. Dillon Jr. and I.S. Jawahir, A review of surface integrity in machining and its impact on functional performance and life of machined products. International Journal Sustainable Manufacturing, volume1 Nos. ½, 2008.

22. D.K. Aspinwall, R.C. Dewes, E.-G. Ng, C. Sage, S.L. Soo, The influence of cutter orientation and workpiece angle on machinability when high-speed milling Inconel 718 under finishing conditions. International Journal of Machine Tools and Manufacture, 47 (2007): pp. 1839–1846

23. A.R.C. Sharman, J.I. Hughes, K. Ridgway, An analysis of the residual stresses generated in Inconel 718 when turning. Journal of Materials Processing Technology, 173 (2006): pp. 359–367

24. Roy, A.K., Marthandam, V., 2009. Mechanism of yield strength anomaly of Alloy 617. Material Science and Engineering A, 517: 276-280.

25. M. Shenoy, Y. Tjiptowidjojo, D. McDowell, Microstructure-sensitive modeling of polycrystalline IN 100, International Journal of Plasticity, Vol. 24, Issue 10, pp 1694-1730, 2008.

26. Beardmore, P Davies, R G | Johnston, T L On the temperature dependence of the flow stress of nickel-base alloys (Flow stress temperature dependence of Ni-Cr-Al alloys consisting of gamma prime dispersion in Ni base solid solution) METALLURGICAL SOCIETY OF AIME, TRANSACTIONS. Vol. 245, pp. 1537-1545. 1969

27. Seyed Sajjadi et al. 2004, Tensile Deformation Mechanisms at Different Temperatures in the Ni-base superalloy GTD-111.

28. M.V. Nathal et al. 1985, Temperature Dependence of γ and γ' Lattice Mismatch in Nickel-base Superalloys.

29. K.J. Ducki 2007, Structure and precipitation strengthening in a high temperature Fe-Ni alloy

30. D.A. Grose 1981, The influence of coherency strain on the elevated temperature tensile behavior of Ni-15Cr-Al-Ti-Mo Alloys

31. Nickel-Based Superalloys: Part One

32. RF Decker, JR Mihalisin, Coherency strains in gamma prime hardened nickel alloys. ASM TRANS QUART, 1969.

33. D. Ulutan, M. Sima, T. Ozel, Prediction of machining induced surface integrity using elastic-viscoelastic simulation and temperature-dependent flow softening material models in Titanium and nickel-based alloys. Advanced Materials Research Vol. 223(2011) pp 401-410.

34. Gordon R. Johnson, William H. Cook. A constitutive model and data for metals subjected to large strain, high strain rates and high temperature. Proceedings of Seventh International Symposium on Ballistics, The Hague (1983)

35. Zerilli, F.J., Armstrong, R.W., 1987. Dislocation Mechanics based Constitutive Relations for Material Dynamic Calculation. Applied Physics, 61/5.

36. Lin, Y.C., Chen, X.M, 2010. A Combined Johson-Cook and Zerilli-Armstong model for hot compressed typical high strength alloy steel. Computational Materials Science, 49: 628-633.

37. Nemat, N.S., Ni, L., Okinaka, T., 1998. A constitutive model for fcc crystals with application to polycrystalline OFHC copper. Mechanics of Materials, 30/4: 325-341.

38. Bammann ,D.J, Chiesa, M.L., Johnson, G.C., 1996. Modeling large deformation and failure in manufacturing processes. Theoretical and Applied Mechanics: 357-376.

39. Cuo, Y.B., Anurag, S., 2007. A modified micromechanical approach to determine flow stress of work materials experiencing complex deformation histories in manufacturing process. International Jounal of Mechanical Science, 49: 909-918

40. L. Chen, T.I. El-Wardany, W.C. Harris, Modeling the effects of flank wear land and chip formation on residual stresses. CIRP Annals—Manufacturing Technology, 53 (1) (2004), pp. 95–98

41. T. Özel, E. Zeren, Finite element modeling the influence of edge roundness on the stress and temperature fields induced by high-speed machining. International Journal of Advanced Manufacturing Technology, 35 (2007), pp. 255–267

42. J.C. Outeiro, D. Umbrello, R. M'Saoubi, Experimental and numerical modeling of residual stresses induced in orthogonal cutting of AISI 316L steel. International Journal of Machine Tools and Manufacture, 46 (2006), pp. 1786–1794

43. M. Nasr, E.G. Ng, M. Elbestawi, Effects of workpiece thermal properties on machining-induced residual stresses—thermal softening and conductivity. Journal of Engineering Manufacture, 221 (2007), pp. 1387–1400

44. K.C. Ee, O.W. Dillon Jr., I.S. Jawahir, Finite element modeling of residual stresses in machining induced by cutting using a tool with finite edge radius. International Journal of Mechanical Sciences, 47 (2005), pp. 1611–1628

45. A. Ramesh, S.N. Melkote, Modeling of white layer formation under thermally dominant conditions in orthogonal machining of hardened AISI 52100 steel. International Journal of Machine Tools and Manufacture, 48 (2008), pp. 402–414

46. P.J. Arrazola, T. Özel, Numerical modelling of 3-D hard turning using Arbitrary Eulerian Lagrangian finite element method. International Journal of Machining and Machinability of Materials, 3 (3) (2008), pp. 238–249

47. Y.B. Guo, S. Anurag, I.S. Jawahir, A novel hybrid predictive model and validation of unique hook-shaped residual stress profiles in hard turning. CIRP Annals—Manufacturing Technology, 58 (1) (2009), pp. 81–84

48. D. Umbrello, L. Filice, Improving surface integrity in orthogonal machining of hardened AISI 52100 steel by modeling white and dark layers formation. CIRP Annals—Manufacturing Technology, 58 (2009), pp. 73–76

49. Y.B. Guo, C.R. Liu, 3D FEA modeling of hard turning. ASME Journal of Manufacturing Science and Engineering, 124 (2002), pp. 189–199

50. S.L. Soo, D.K. Aspinwall, R.C. Dewes, 3D FE modeling of the cutting of Inconel 718. Journal of Materials Processing Technology, 150 (2004), pp. 116–123

51. S.L. Soo, D.K. Aspinwall, R.C. Dewes Three-Dimensional, Finite element modelling of high-speed milling of Inconel 718. Proceedings of the Institution of Mechanical Engineers, Part B: Journal of Engineering Manufacture, 218 (2004), pp. 1555–1561

52. T.D. Marusich, M. Ortiz, Modeling and simulation of high-speed machining. International Journal for Numerical Methods in Engineering, 38 (1995), pp. 3675–3694

53. T. Özel, Computational modelling of 3-D turning with variable edge design tooling: influence of micro-geometry on forces, stresses, friction and tool wear. Journal of Materials Processing Technology, 209 (11) (2009), pp. 5167–5177

54. T. Özel, E. Zeren, Finite element modeling the influence of edge roundness on the stress and temperature fields induced by high-speed machining. International Journal of Advanced Manufacturing Technology, 35 (2007), pp. 255–267

55. T. Özel, Computational modelling of 3-D turning with variable edge design tooling: influence of micro-geometry on forces, stresses, friction and tool wear. Journal of Materials Processing Technology, 209 (11) (2009), pp. 5167–5177

56. A. Haglund, H.A. Kishawy, R.J. Rogers, An exploration of friction models for the chip tool interface using an Arbitrary Lagrangian–Eulerian finite element model. Wear, 265 (3–4) (2008), pp. 452–460

57. R. Sievert, H.D. Noack, A. Hamann, P. Loewe, K.N. Singh, G. Kuenecke, R. Clos, U. Schreppel, P. Veit, E. Uhlmann, R. Zettier, Simulation der Spansegmentierung beim Hochgeschwindigkeits-Zerspanned unter Berücksichtigung duktiler Schädigung. Techniche Mechanik, 23 (2–4) (2003), pp. 216–233

58. G.R. Johnson, W.H. Cook, A constitutive model and data for metals subjected to large strains, high strain rates and high temperatures. Proceedings of the Seventh International Symposium on Ball (1983), pp. 541–547

59. A.V. Mitrofanov, V.I. Babitsky, V.V. Silberschmidt, Finite element analysis of ultrasonically assisted turning of Inconel 718. Journal of Materials Processing Technology, 153–154 (2004), pp. 233–239

60. E. Uhlmann, M. Graf von der Schulenburg, R. Zettier, Finite element modeling and cutting simulation of Inconel 718. Annals of the CIRP, 56 (1) (2007), pp. 61–64

61. M. Field, J. F. Kahles and J. J. Cammett, Review of measuring methods for subsurface integrity, Ann.CIRP, 21 (2) (1972), pp. 219-237

62. Tae-Young Kim, Y. Matsumoto, H.G. Shin and D. William Wu, A new technique to measure plastic strain in the machined surface, Wear 147 (1991), pp. 311-322

63. Tetsufumi Shoji, Crack-tip blunting and crack-opening displacement under large-scale yielding. Material Science, 10(5) (1976), pp. 165-169

64. T. Kitagawa, A. Kubo, K. Maekawa, Temperature and wear of cutting tools in high-speed machining of Inconel 718 and Ti-6Al-6V-2Sn. Wear 1997 Volum 202 Issue2 pp 142-148

65. ABAQUS version 6.8 Documentation.

66. A.K. Balaji, G. Sreeram, I.S. Jawahir, E. Lenz, The effects of cutting tool thermal conductivity on tool-chip contact length and cyclic chip formation in machining with grooved tools. Annals of the CIRP Vol. 48/1/1999

67. A. Jawaid, S. Sharif, S. Koksal. Evaluation of wear mechanisms of coated carbide tool when face milling titanium alloy. Journal of Material Processing Technology 99 (2000) pp 266-274

68. D. Ulutan, M. Sima and T. Ozel, 2011, Prediction of Machining Induced Surface Integrity using Elastic-Viscoelastic Simulations and Temperature-Dependent Flow Softening Material Models in Titanium and Nickel-based alloys. Advanced Material Research Vol. 233 (2011) pp 401-410.

69. Ibanez, A.R., 2003, Dissertation: Modeling Creep Behavior in a Directionally Solidified Nickel Based Superalloys, Dissertation in Georgia Institute of Technology.

70. ASTM Standard E8-98, 1998. Annual Book of ASTM Standards, 03.01:.57-77.

71. Daleo, J. and Wilson, J. (1998), "GTD111 Alloy Material Study", Journal of Engineering for Gas Turbines and Power, Vol. 120, pp 375-382.

72. M. Calamaz, D. Coupard and F. Girot, 2008, A new material model for 2D numerical simulation of serrated chip formation when machining titanium alloy Ti-6Al-4V. International Journal of Machine Tools and Manufacture, Volume 48, Issue3-4, pp: 275-288

73. Fionn Dunne, Nik Petrinc, Introduction to Computational Plasticity, Oxford University Press.

74. Boyce J. Richardson, Jr. Identification of and effects on the depth of the machining affected zone in Nickel-Based Superalloys. Dec. 2010

75. P. R. Rios, F. S. Jr, H. R. Z. Sandim, R. L. Plaut, A. F. Padilha, Nucleation and growth during Recrystallization. Material Research, (2005) Vol.8, No.3, pp: 225-238.